Università degli Studi di Padova

Dipartimento di Fisica e Astronomia "Galileo Galilei"
Corso di Laurea Magistrale in Fisica

A QUADRATIC ESTIMATOR FOR THE MATTER POWER SPECTRUM FROM WEAK GRAVITATIONAL LENSING

Relatore:
Ch.mo Prof. Sabino
Matarrese
Università degli Studi di Padova

Correlatore:
Ch.mo Prof. Alan Francis
Heavens
Imperial College London

Laureando:
Alessio Spurio Mancini
Matricola 1079663

Anno Accademico 2014/2015

Abstract

A quadratic estimator for the matter power spectrum from weak gravitational lensing

Weak gravitational lensing is one of the most powerful tools available to cosmologists to gain an insight into our Universe. In particular, measurements of this relativistic effect can provide information about the matter power spectrum. This describes the amplitude of density fluctuations on different scales and plays a key role in the theories that describe the formation of large-scale structures. However, since the matter overdensity is connected to the weak lensing convergence through a line-of-sight integral, this effect mixes the different physical scales and makes it difficult to isolate the power spectrum at a certain scale.

In this thesis a new quadratic estimator for the power spectrum, based on weak lensing measurements, is developed. According to the Cramér-Rao inequality, the estimator is guaranteed to have the minimum variance and is therefore the best unbiased estimator of the power spectrum. The properties of this estimator are explored, in particular its window functions which are optimised to be as narrow as possible in k-space. This would permit to isolate the effects of physical processes that act on different scales. A major goal here is to detect features at $k \sim 1\,h\,\mathrm{Mpc}^{-1}$ arising from non-zero neutrino masses. A second is to develop statistics that are insensitive to the high-k regime ($k > 1\,h\,\mathrm{Mpc}^{-1}$) that may be affected by uncertain baryon feedback processes.

Contents

Introduction

The term *gravitational lensing* refers to the deflection of light rays from distant sources by means of the intervening matter distribution along the line of sight towards the observer. This effect, whose existence was speculated long before the advent of General Relativity (see Schneider (1992) for a historical review), was put on solid theoretical grounds by Einstein's theory of gravity. A famous general relativistic result [Einstein (1911)] is the prediction of the deflection angle for a light ray approaching the surface of the Sun, which yields a value twice as big as the one calculated within Newtonian gravitation. Indeed, the confirmation of the larger value, thanks to the observations performed in May 1919 by Arthur Eddington and his collaborators during a total solar eclipse [Eddington et al. (1920)], still represents one of the best tests of General Relativity as the correct theory of gravity.

The deflection of light rays emitted from a background galaxy produces a distortion of the image of the source, which is both sheared and (de)magnified. It is customary to distinguish two fields of study of gravitational lensing, according to the intensity of these effects. First, we can identify the so called *strong lensing* regime (see Treu (2010) for a review), corresponding to big effects, potentially leading to multiple images of distant objects. These perturbations are usually produced by very massive and well-identified foreground lenses, such as clusters of galaxies, whose properties (e.g. the mass) can be investigated analysing the distortions induced on the images.

We refer instead to *weak gravitational lensing* (see Bartelmann and Schneider (2001) or Schneider (2006) for comprehensive reviews) when the changes in the observed images are small. We will be mainly interested in weak gravitational lensing on a large scale, or *cosmic shear*. This field of study, despite being technically challenging, has recently seen rapid advances from the first detections published only in the year 2000 [Bacon et al. (2000); Kaiser et al. (2000); Van Waerbeke et al. (2000); Wittman et al. (2000)]. Cosmic shear is based on the fact that the effects of gravitational lensing are not limited to small scales or to high density regions. At large radii the tidal field causes a subtle change in the shapes of galaxies, resulting in a coherent alignment of the sources that can be measured statistically.

Indeed, cosmic shear measurements are intrinsically statistical, because in this case the lensing effect is not associated with a particular intervening lens, but rather corresponds to small distortions (of the order of 1%) of the images of distant galaxies by all density fluctuations along the line of sight. In this context, one does not use gravitational lensing to obtain the characteristics of a single massive object, but tries to derive the statistical properties of the density field, which in turn can be used to constrain cosmological parameters (see Munshi et al. (2008) for a review on cosmological applications of weak lensing).

The key observable in this context is the matter power spectrum (see Peacock (1999) for a definition), which describes the amplitudes of the density fluctuations on different scales. The ability of weak lensing to constrain the matter power spectrum makes it an invaluable tool to analyse the large scale structures of our Universe. The advantage of weak lensing is its ability to probe the matter distribution more directly than traditional methods such as the galaxy catalogue, fundamentally limited by our poor knowledge of galaxy formation and evolution.

This thesis addresses the question of the extraction of information about the matter power spectrum $P(k)$ from weak lensing measurements. We develop a new quadratic estimator for $P(k)$ from the convergence κ, one of the parameters that describe the lensing effect on background sources.

Generally speaking, the estimation of power spectra from various types of data is becoming increasingly important in cosmology (see Efstathiou (2004) for a critical discussion). There are three main reasons for this. Firstly, there has been an explosion in the size and quality of cosmological data sets. With such large data sets it is now possible to measure power spectra accurately over a wide range of angular and spatial scales. Secondly, the power spectrum is a simple two-point statistic and so it is natural that more effort has been devoted to optimal methods for the power spectrum estimation rather than to optimal estimators for higher order statistics. Thirdly, in most realisations of the inflationary scenario, the fluctuations generated during the inflationary phase are predicted to be Gaussian (see e.g. Liddle and Lyth (2000), for a review). If the fluctuations are Gaussian, and as long as they remain linear, all of the information pertaining to the fluctuations is contained in the power spectrum.

Quadratic estimators have been largely employed in the statistical challenge of recovering as much information as possible about the power spectra. Most importantly for our purposes, Tegmark et al. have proposed quadratic estimators for the CMB angular power spectrum [Tegmark (1997)] and the three-dimensional power spectrum of galaxies [Tegmark et al. (2004)]. The interest for a quadratic combination of data comes from the fact that these methods have proved to be unbeatable, in the sense that their information

content is maximised. In this case, estimation of the power spectrum can be viewed as a form of lossless data compression. This approach is invaluable, since physical parameters of interest can be estimated from the power spectrum and its covariance matrix, rather than from the pixel values themselves.

Motivated by the appealing features of these techniques, in this thesis we devise and implement a quadratic estimator for the matter power spectrum based on weak lensing estimates. Here the situation appears to be more complicated than in Tegmark's papers, because lensing is an integrated effect along the line of sight and this implies mixing of different scales, which makes it not clear *a priori* that the technique will succeed.

We first derive the mathematics of the estimator, essentially extending the same basics of Tegmark (1997) and Tegmark et al. (2004) to the weak lensing case, and subsequently we carry out a series of tests on our estimator. Given the complexity of the problem, we decide to set out on the study of the estimator following an increasing level of sophistication. In particular, this implies moving from a unidimensional case to a 2D and 3D approach, while passing from an idealised treatment in absence of noise to a more realistic approach with a finite signal-to-noise ratio. The analysis is performed using the convergence κ, since it is a scalar parameter and therefore easier to treat in an initial approach, but the calculations for the shear γ are also presented in the concluding section of the thesis.

The physical interest for this estimator resides in its ability to isolate the effects of physical processes that act on different scales. We are particularly interested in developing statistics that could detect features at $k \sim 1\,h\,\mathrm{Mpc}^{-1}$ arising from non-zero neutrino mass, as well as developing statistics that are sensitive or insensitive to the high-k regime ($k > 1\,h\,\mathrm{Mpc}^{-1}$), where uncertain baryon feedback processes become important.

This thesis is structured as follows:

1. In Chapter 1 we review the main results of the gravitational lensing theory, starting from the case of a single lens and a set of lenses at a fixed redshift. We then move to the case of lensing by the large-scale structure in the Universe.

2. In Chapter 2 we introduce the matter power spectrum and we analyse the effect of massive neutrinos on it.

3. In Chapter 3 we describe the basis of the quadratic methods in the estimation of power spectra, analysing the algorithms and the results of Tegmark (1997) and Tegmark et al. (2004), as our new method represents an extension of these models to the more complicated case of weak lensing.

4. In Chapter 4 we describe the mathematical foundations of our new method, developing the optimised weights for the estimation of $P(k)$ from the convergence κ in different signal-to-noise regimes.

5. In Chapter 5 we apply the new method to a unidimensional model that we use to test the estimator. In this model we choose an input power spectrum and we check how well the estimator recovers it from the simulated convergence field. We describe in detail the algorithm followed to test the estimator and we present the results obtained.

6. In Chapter 6 we apply the same procedure to a two-dimensional and three-dimensional grid. We report the main differences with the unidimensional model and the results obtained in these new cases.

7. In Chapter 7 we conclude by reviewing the results obtained, commenting the approximations made and suggesting some possible future developments of the estimator. We also present the calculations for the shear γ.

Chapter 1

Lensing formalism

1.1 Light deflection

We start by considering the gravitational lensing effect by a single intervening mass distribution (Sect. 1.1.1) and a set of lenses at a fixed redshift (Sect. 1.1.2). This will introduce some of the ideas that we will then use in Sect. 1.2, when we will analyse the gravitational lensing effect by the large-scale structure in the Universe, the case of major interest for our purposes.

1.1.1 Deflection angle from Fermat's principle

Following the approach of Meneghetti (2012), in this first subsection we describe light deflection using Fermat's principle. This turns out to be equivalent to the study of geodesic curves. In its simplest form, Fermat's principle states that the path followed by light waves of a given frequency is the one that minimises the travel time,

$$\int \frac{n}{c} dl \tag{1.1}$$

where n is the index of refraction of the medium. We thus search for a path, $\vec{x}(l)$, for which the variation

$$\delta \int_A^B n\left(\vec{x}\left(l\right)\right) dl = 0 \tag{1.2}$$

where the extreme points A and B are fixed.
In order to find the index of refraction we make a first approximation: we assume the lens to be small, such that its dimension is negligible compared to the overall system (source, lens and observer) and "weak". By this we mean a lens whose Newtonian gravitational potential Φ is much smaller than c^2, $\Phi/c^2 \ll 1$. The unperturbed space-time, described by the Minkowski metric $\eta_{\mu\nu} = diag(1, -1, -1, -1)$, is perturbed by a weak lens such that

$\eta_{\mu\nu} \rightarrow g_{\mu\nu} = diag(1 + \frac{2\Phi}{c^2}, 1 - \frac{2\Phi}{c^2}, 1 - \frac{2\Phi}{c^2}, 1 - \frac{2\Phi}{c^2})$ and the line element becomes

$$ds^2 = \left(dx^0\right)^2 - \left(dx^1\right)^2 - \left(dx^2\right)^2 - \left(dx^3\right)^2 \rightarrow ds^2 = \left(1 + \frac{2\Phi}{c^2}\right) c^2 dt^2 - \left(1 - \frac{2\Phi}{c^2}\right) \left(d\vec{x}^2\right) \tag{1.3}$$

Since for light we have $ds = 0$, it follows that

$$\left(1 + \frac{2\Phi}{c^2}\right) c^2 dt^2 = \left(1 - \frac{2\Phi}{c^2}\right) \left(d\vec{x}^2\right) \tag{1.4}$$

The light speed in the gravitational field is thus

$$c' = \frac{|d\vec{x}|}{dt} = c\sqrt{\frac{1 + \frac{2\Phi}{c^2}}{1 - \frac{2\Phi}{c^2}}} \approx c\left(1 + \frac{2\Phi}{c^2}\right) \tag{1.5}$$

where $\Phi/c^2 \ll 1$ by assumption. The index of refraction is thus

$$n = c/c' = \frac{1}{1 + \frac{2\Phi}{c^2}} \approx 1 - \frac{2\Phi}{c^2}. \tag{1.6}$$

With $\Phi \leq 0,\ n \geq 1$, and the light speed c is lower than in vacuum. n will depend on the spatial coordinate $\vec{x}$ and on time t. Let $\vec{x}(l)$ be a light path. Then the light travel time is proportional to

$$\int_A^B n\left[\vec{x}(l)\right] \, \mathrm{d}l, \tag{1.7}$$

and the light path follows from

$$\delta \int_A^B n\left[\vec{x}(l)\right] \, \mathrm{d}l = 0. \tag{1.8}$$

Let us write

$$dl = \left|\frac{d\vec{x}}{d\lambda}\right| d\lambda \tag{1.9}$$

with a curve parameter λ which is yet arbitrary, and find

$$\delta \int_{\lambda_A}^{\lambda_B} d\lambda \, n\left[\vec{x}(\lambda)\right] \left|\frac{d\vec{x}}{d\lambda}\right| = 0. \tag{1.10}$$

Defining

$$\dot{\vec{x}} = \frac{d\vec{x}}{d\lambda}, \tag{1.11}$$

we have

$$\left|\frac{d\vec{x}}{d\lambda}\right| = \left|\dot{\vec{x}}\right| = (\dot{\vec{x}}^2)^{1/2} \tag{1.12}$$

and, considering our Lagrangian

$$n\left[\vec{x}(\lambda)\right]\left|\frac{d\vec{x}}{d\lambda}\right| \equiv L(\dot{\vec{x}}, \vec{x}, \lambda) \tag{1.13}$$

we find the Euler equations

$$\frac{d}{d\lambda}\frac{\partial L}{\partial \dot{\vec{x}}} - \frac{\partial L}{\partial \vec{x}} = 0 \tag{1.14}$$

where

$$\frac{\partial L}{\partial \vec{x}} = \left|\dot{\vec{x}}\right| \frac{\partial n}{\partial \vec{x}} = (\vec{\nabla} n)\left|\dot{\vec{x}}\right|, \quad \frac{\partial L}{\partial \dot{\vec{x}}} = n\frac{\dot{\vec{x}}}{\left|\dot{\vec{x}}\right|}. \tag{1.15}$$

By a suitable choice of the curve parameter λ we can assume $\dot{\vec{x}} = 1$ and write $\vec{e} \equiv \dot{\vec{x}}$ for the unit tangent vector to the light path. Then, we have

$$\frac{d}{d\lambda}(n\vec{e}) - \vec{\nabla} n = 0 \tag{1.16}$$

or

$$n\dot{\vec{e}} + \vec{e}\cdot[(\vec{\nabla} n)\vec{\nabla}] = \vec{\nabla} n \implies n\dot{\vec{e}} = \vec{\nabla} n - \vec{e}(\vec{\nabla}\cdot\vec{e}). \tag{1.17}$$

The right hand side is the gradient of n perpendicular to the light path. Thus

$$\dot{\vec{e}} = \frac{1}{n}\vec{\nabla}_\perp n = \vec{\nabla}_\perp \ln n \tag{1.18}$$

As $n = 1 - 2\Phi/c^2$ and $\Phi/c^2 \ll 1$, $\ln n \approx -2\Phi/c^2$, and

$$\dot{\vec{e}} = -\frac{2}{c^2}\vec{\nabla}_\perp \Phi \tag{1.19}$$

The total deflection angle of the light path is now the integral over $-\dot{\vec{e}}$ along the light path,

$$\hat{\vec{\alpha}} = \frac{2}{c^2}\int_{\lambda_A}^{\lambda_B} \vec{\nabla}_\perp \Phi d\lambda \tag{1.20}$$

As it stands, the equation for α is not useful, as one would have to integrate over the actual light path. However, since $\Phi/c^2 \ll 1$, we expect the deflection angle to be small. Then, we can adopt the Born approximation and integrate over the unperturbed light path. We suppose, therefore, that

a light ray starts out into $+\vec{e}_z$-direction and passes a lens at $z = 0$, with impact parameter b. The deflection angle is then given by

$$\hat{\vec{\alpha}} = \frac{2}{c^2} \int_{-\infty}^{+\infty} \vec{\nabla}_\perp \phi \, \mathrm{d}z \tag{1.21}$$

In particular if the lens is a point mass, then

$$\Phi = -\frac{GM}{r} \tag{1.22}$$

and the deflection angle is therefore:

$$|\hat{\vec{\alpha}}| = \frac{4GM}{bc^2} = 2\frac{R_S}{b}. \tag{1.23}$$

This famous result, first obtained by Einstein himself [Einstein (1911)], is twice as big as the one that we would obtain by treating the photons as corpuscles in standard Newtonian Gravity.

1.1.2 Lens equation from a geometric approach

The deflection angle in Eq. 1.23 depends linearly on the mass M. This ensures that the deflection angles of a set of lenses can be linearly superposed. Then let us suppose to have a sparse distribution of N point masses on a plane, whose positions and masses are ξ_i and M_i, $1 \leq i \leq N$. The deflection angle of a light ray crossing the plane at ξ will be:

$$\hat{\vec{\alpha}}(\vec{\xi}) = \sum_i \hat{\vec{\alpha}}_i(\vec{\xi} - \vec{\xi}_i) = \frac{4G}{c^2} \sum_i M_i \frac{\vec{\xi} - \vec{\xi}_i}{|\vec{\xi} - \vec{\xi}_i|^2} \tag{1.24}$$

In order to consider three dimensional distributions of matter we adopt a simplifying approximation, called the *thin screen approximation*.
This consists of approximating the lens by a planar distribution of matter, the lens plane. Even the sources are assumed to lie on a plane, called the source plane. The physical motivation behind this approximation is the fact that even in the case of lensing by galaxy clusters, the physical size of the lens is generally much smaller than the distances between observer, lens and source [Wambsganss (1998)]. The deflection therefore arises along a very short section of the light path. Within this approximation, the lensing matter distribution is fully described by its surface density,

$$\Sigma(\vec{\xi}) = \int \rho(\vec{\xi}, z) dz, \tag{1.25}$$

where $\vec{\xi}$ is a two-dimensional vector on the lens plane and ρ is the three-dimensional density. As long as the thin screen approximation holds, the total deflection angle is obtained by summing the contribution of all the mass elements $\Sigma(\xi) d^2\xi$:

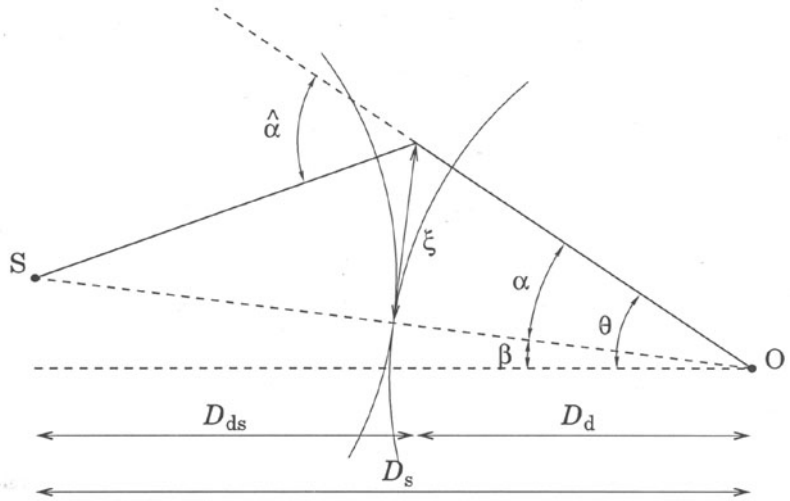

Figure 1.1: Model of a typical gravitational lens

$$\hat{\vec{\alpha}}(\vec{\xi}) = \frac{4G}{c^2} \int \frac{(\vec{\xi} - \vec{\xi}_i)\Sigma(\vec{\xi}')}{|\vec{\xi} - \vec{\xi}_i|^2} d^2\vec{\xi}'. \tag{1.26}$$

In Fig. 1.1 a typical gravitational lens system is shown, consisting of a mass concentration placed at redshift z_L, corresponding to an angular diameter distance D_L. The lens deflects the light rays coming from a source at redshift z_S (or angular distance D_S).
We first define an optical axis, indicated by the dashed line, perpendicular to the lens and source planes and passing through the observer. Then we measure the angular positions on the lens and on the source planes with respect to this reference direction. Let us consider a source at the angular position β, which lies on the source plane at a distance $\eta = \beta D_S$ from the optical axis. The deflection angle $\hat{\alpha}$ of the light ray coming from that source and having an impact parameter $\xi = \theta D_L$ on the lens plane is given by Eq. 1.21. Due to the deflection, the observer receives the light coming from the source as if it was emitted at the angular position θ. If $\vec{\theta}$, $\vec{\beta}$ and $\hat{\alpha}$ are small, the true position of the source and its observed position on the sky are related by a very simple relation, called the *lens equation*:

$$\vec{\theta} D_S = \vec{\beta} D_S + \hat{\vec{\alpha}} D_{LS} \tag{1.27}$$

where D_{LS} is the angular diameter distance between lens and source. Defining the reduced deflection angle

$$\vec{\alpha}(\vec{\theta}) \equiv \frac{D_{LS}}{D_S} \hat{\vec{\alpha}}(\vec{\theta}), \tag{1.28}$$

Eq. 1.27 becomes

$$\vec{\beta} = \vec{\theta} - \vec{\alpha}(\vec{\theta}). \tag{1.29}$$

It is very useful to write the lens equation in a dimensionless form. We then define a length scale ξ_0 on the lens plane and a corresponding length scale $\eta_0 = \xi_0 D_S/D_L$ on the source plane. Furthermore, if we define the dimensionless vectors

$$\vec{x} \equiv \frac{\vec{\xi}}{\xi_0}; \quad \vec{y} \equiv \frac{\vec{\eta}}{\eta_0} \tag{1.30}$$

as well as the scaled deflection angle

$$\vec{\alpha}(\vec{x}) = \frac{D_L D_S}{\xi_0 D_S} \hat{\vec{\alpha}}\left(\xi_0 \vec{x}\right), \tag{1.31}$$

we can rewrite the lens equation as

$$\vec{y} = \vec{x} - \vec{\alpha}(\vec{x}). \tag{1.32}$$

1.1.3 Lensing potential

An extended distribution of matter is characterized by its effective lensing potential, obtained by projecting the three-dimensional Newtonian potential on the lens plane and by properly rescaling it:

$$\hat{\Psi}(\vec{\theta}) = \frac{D_{LS}}{D_L D_S} \frac{2}{c^2} \int \Psi(D_L \vec{\theta}, z) dz \tag{1.33}$$

and its dimensionless version

$$\Psi = \frac{D_L^2}{\xi_0^2} \hat{\Psi}. \tag{1.34}$$

This lensing potential satisfies two important properties:
(1) the gradient of Ψ gives the scaled deflection angle:

$$\vec{\nabla}_x \Psi(\vec{x}) = \vec{\alpha}(\vec{x}) \tag{1.35}$$

This can be shown to be true by direct calculation:

$$\begin{aligned} \vec{\nabla}_x \Psi(\vec{x}) &= \xi_0 \vec{\nabla}_\perp \left(\frac{D_{LS} D_L}{\xi_0^2 D_S} \frac{2}{c^2} \int \Phi(\vec{x}, z) dz \right) \\ &= \frac{D_{LS} D_L}{\xi_0^2 D_S} \frac{2}{c^2} \int \vec{\nabla}_\perp \Phi(\vec{x}, z) dz \\ &= \vec{\alpha}(\vec{x}) \end{aligned} \tag{1.36}$$

(2) the Laplacian of Ψ gives twice the *convergence*:

$$\nabla_x^2 \Psi(\vec{x}) = 2\kappa(\vec{x}) \tag{1.37}$$

This is defined as a dimensionless surface density

$$\kappa(\vec{x}) \equiv \frac{\Sigma(\vec{x})}{\Sigma_{cr}} \quad \text{with} \quad \Sigma_{cr} = \frac{c^2}{4\pi G} \frac{D_S}{D_L D_{LS}} \tag{1.38}$$

where Σ_{cr} is called the critical surface density: this is a function of the angular diameter distances of lens and source that characterizes the lens system.
To show that Eq. 1.37 holds, we first remember the Poisson equation,

$$\nabla^2 \Phi = 4\pi G \rho. \tag{1.39}$$

The surface mass density is

$$\Sigma(\vec{\theta}) = \frac{1}{4\pi G} \int_{-\infty}^{+\infty} \nabla^2 \Phi \, \mathrm{d}z \tag{1.40}$$

and

$$\kappa(\vec{\theta}) = \frac{1}{c^2} \frac{D_L D_{LS}}{D_S} \int_{-\infty}^{+\infty} \nabla^2 \Phi \, \mathrm{d}z. \tag{1.41}$$

Let us now introduce a two-dimensional Laplacian

$$\nabla_\theta^2 = \frac{\partial^2}{\partial \theta_1^2} + \frac{\partial^2}{\partial \theta_2^2} = D_L^2 \left(\frac{\partial^2}{\partial \xi_1^2} + \frac{\partial^2}{\partial \xi_2^2} \right) = D_L^2 \left(\nabla^2 - \frac{\partial^2}{\partial z^2} \right) \tag{1.42}$$

which gives

$$\nabla^2 \Phi = \frac{1}{D_L^2} \nabla_\theta^2 \Phi + \frac{\partial^2 \Phi}{\partial z^2} \tag{1.43}$$

Inserting Eq. 1.43 into Eq. 1.41, we obtain

$$\kappa(\vec{\theta}) = \frac{1}{c^2} \frac{D_{LS}}{D_S D_L} \left[\nabla_\theta^2 \int_{-\infty}^{+\infty} \Phi dz + D_L^2 \int_{-\infty}^{+\infty} \frac{\partial^2 \Phi}{\partial z^2} dz \right] \tag{1.44}$$

If the lens is gravitationally bound, $\partial \Phi / \partial z = 0$ at its boundaries and the second term on the right hand side vanishes. From Eqs. 1.33 and 1.34, we find

$$\kappa(\theta) = \frac{1}{2} \nabla_\theta^2 \hat{\Psi} = \frac{1}{2} \frac{\xi_0^2}{D_L^2} \nabla_\theta^2 \Psi. \tag{1.45}$$

Since

$$\nabla_\theta^2 = D_L^2 \nabla_\xi^2 = \frac{D_L^2}{\xi_0^2} \nabla_x^2 \tag{1.46}$$

using adimensional quantities Eq. 1.45 reads

$$\kappa(\vec{x}) = \frac{1}{2}\nabla_x^2 \Psi(\vec{x}). \tag{1.47}$$

Integrating Eq. 1.37, the effective lensing potential can be written in terms of the convergence as

$$\Psi(\vec{x}) = \frac{1}{\pi}\int_{\mathbf{R}^2} \kappa(\vec{x}') \ln|\vec{x} - \vec{x}'| d^2x', \tag{1.48}$$

from which we obtain that the scaled deflection angle is

$$\vec{\alpha}(\vec{x}) = \frac{1}{\pi}\int_{\mathbf{R}^2} d^2x' \kappa(\vec{x}') \frac{\vec{x} - \vec{x}'}{|\vec{x} - \vec{x}'|}. \tag{1.49}$$

1.1.4 Shear

One of the main features of gravitational lensing is the distortion which it introduces into the shape of the sources. This is particularly evident when the source has no negligible apparent size. For example, background galaxies can appear as very long arcs in galaxy clusters. The distortion arises because light bundles are deflected differentially. Ideally the shape of the images can be determined by solving the lens equation for all the points within the extended source. In particular, if the source is much smaller than the angular size on which the physical properties of the lens change, the relation between source and image positions can locally be linearized. In other words, the distortion of images can be described by the Jacobian matrix

$$A \equiv \frac{\partial y}{\partial x} = \left(\delta_{ij} - \frac{\partial \alpha_i(x)}{\partial x_j}\right) = \left(\delta_{ij} - \frac{\partial^2 \Psi(x)}{\partial x_i \partial x_j}\right) \tag{1.50}$$

where x_i indicates the $i-$component of x on the lens plane. Eq. 1.50 shows that the elements of the Jacobian matrix can be written as combinations of the second derivatives of the lensing potential. We will use the shorthand notation

$$\frac{\partial^2 \Psi(x)}{\partial x_i \partial x_j} \equiv \Psi_{ij}. \tag{1.51}$$

We can now split off an isotropic part from the Jacobian:

$$A - \frac{1}{2} trA \cdot I = \delta_{ij} - \Psi_{ij} - \frac{1}{2}\left(1 - \Psi_{11} + 1 - \Psi_{22}\right)\delta_{ij} \tag{1.52}$$

$$= -\Psi_{ij} + \frac{1}{2}\left(\Psi_{11} + \Psi_{22}\right)\delta_{ij} \tag{1.53}$$

$$= \begin{pmatrix} -\frac{1}{2}(\Psi_{11} - \Psi_{22}) & -\Psi_{12} \\ -\Psi_{12} & \frac{1}{2}(\Psi_{11} - \Psi_{22}) \end{pmatrix} \tag{1.54}$$

This antisymmetric, trace-free matrix is called the shear matrix. It quantifies the projection of the gravitational tidal field (the gradient of the gravitational force), which describes distortions of background sources.
This allows us to define the pseudo-vector $\vec{\gamma} = (\gamma_1, \gamma_2)$ on the lens plane, whose components are

$$\gamma_1(\vec{x}) = \frac{1}{2}(\Psi_{11} - \Psi_{22})\gamma_2(\vec{x}) = \Psi_{12} = \Psi_{21} \tag{1.55}$$

This is called the *shear*. The eigenvalues of the shear matrix are

$$\pm\sqrt{\gamma_1^2 + \gamma_2^2} = \pm\gamma \tag{1.56}$$

Thus, there exists a coordinate rotation by an angle ϕ such that

$$\begin{pmatrix} \gamma_1 & \gamma_2 \\ \gamma_2 & -\gamma_1 \end{pmatrix} = \gamma \begin{pmatrix} \cos 2\phi & \sin 2\phi \\ \sin 2\phi & \cos 2\phi \end{pmatrix} \tag{1.57}$$

The factor 2 on the angle Φ indicates that the shear component are elements of a 2×2 tensor and not a vector.
The remainder of the Jacobian is

$$\frac{1}{2}\mathrm{Tr}A = \left[1 - \frac{1}{2}(\psi_{11} + \psi_{22})\right]\delta_{ij} \tag{1.58}$$

$$= \left(1 - \frac{1}{2}\nabla^2\Psi\right)\delta_{ij} = (1 - \kappa)\delta_{ij} \tag{1.59}$$

Thus, the Jacobian matrix becomes

$$A = \begin{pmatrix} 1 - \kappa - \gamma_1 & -\gamma_2 \\ -\gamma_2 & 1 - \kappa + \gamma_1 \end{pmatrix} = (1 - \kappa)\begin{pmatrix} 1 & 0 \\ 0 & 1 \end{pmatrix} - \gamma \begin{pmatrix} \cos 2\phi & \sin 2\phi \\ \sin 2\phi & -\cos 2\phi \end{pmatrix} \tag{1.60}$$

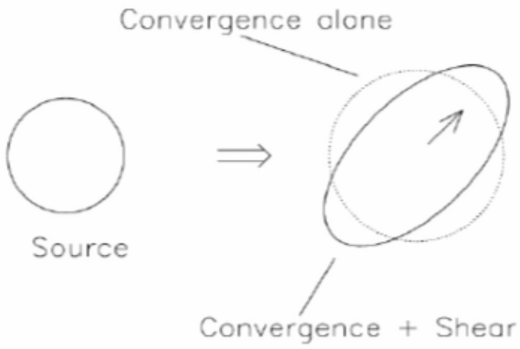

Figure 1.2: Distortion effects due to convergence and shear on a circular source

The last equation explains the meaning of both convergence and shear. The distortion induced by the convergence is isotropic, i.e. the images are only rescaled by a constant factor in all directions. On the other hand, the shear stretches the intrinsic shape of the source along one privileged direction. For this reason, a circular source, which is small enough compared to the scale of the lens, like that shown in Fig. 1.2, is mapped into an ellipse when κ and γ are both non-zero. The semi-major and -minor axes are

$$a = \frac{r}{1-\kappa-\gamma}, \quad b = \frac{1}{1-\kappa+\gamma} \tag{1.61}$$

where r is the radius of the circular source.
An important consequence of the lensing distortion is the magnification. Through the lens equation, the solid angle element $\delta\beta^2$ (or equivalently the surface element δy^2) is mapped into the solid angle $\delta\theta^2$ (or into the surface element δx^2). Since the Liouville theorem and the absence of emission and absorption of photons in gravitational light deflection ensure the conservation of the source surface brightness, the change of the solid angle under which the source is seen implies that the flux received from a source is magnified (or demagnified).
Given Eq. 1.50, the magnification is quantified by the inverse of the determinant of the Jacobian matrix. For this reason, the matrix $M = A^{-1}$ is called the *magnification* tensor. We therefore define

$$\mu \equiv \det M = \frac{1}{\det A} = \frac{1}{(1-\kappa)^2 - \gamma^2} \tag{1.62}$$

The eigenvalues of the magnification tensor (or the inverse of the eigenvalues of the Jacobian matrix) measure the amplification in the tangential and in the radial direction and are given by

$$\mu_t = \frac{1}{\lambda_t} = \frac{1}{1-\kappa-\gamma} \tag{1.63}$$

$$\mu_r = \frac{1}{\lambda_r} = \frac{1}{1-\kappa+\gamma} \tag{1.64}$$

The magnification is ideally infinite where $\lambda_t = 0$ and where $\lambda_r = 0$. These two conditions define two curves in the lens plane, called the tangential and the radial critical line, respectively. An image forming along the tangential critical line is strongly distorted tangentially to this line. On the other hand, an image forming close to the radial critical line is stretched in the direction perpendicular to the line itself.

1.2 Lensing by large-scale structures

1.2.1 Light propagation through an inhomogeneous universe

In contrast to the earlier treatment, we have to take into account that lenses can now be of comparable size to the curvature scale of the universe, thus we need to refine the picture of straight light paths which are instantly deflected by sheet-like, thin lenses. Starting from null geodesic in space-time, it can be shown [Seitz et al. (1994)] that light rays propagate through the unperturbed Friedmann-Lemaitre spacetime such that the comoving separation vector $\vec{x}$ between them changes with the radial coordinate w as

$$\frac{d^2\vec{x}}{dw^2} + K\vec{x} = 0 \tag{1.65}$$

where $K = (H_0/c)^2(\Omega_0 + \Omega_\Lambda - 1)$ is the curvature parameter of the universe. Ω_0 is the density parameter of the universe today,

$$\Omega_0 = \left(\frac{3H_0^2}{8\pi G}\right)^{-1} \rho_0 \tag{1.66}$$

while Ω_Λ is the density parameter corresponding to the cosmological constant,

$$\Omega_\Lambda = \frac{\Lambda}{3H_0^2}. \tag{1.67}$$

H_0 is the Hubble constant. Comoving means that the physical separation r between the rays is divided by the scale factor of the universe,

$$\vec{x} = \frac{\vec{r}}{a} \tag{1.68}$$

in order to get rid of the expansion of space-time. The metric is written as

$$ds^2 = c^2dt^2 - a^2[dw^2 + f_K^2(w)d^2\Omega] \tag{1.69}$$

such that dw is the radial, comoving distance element, and $f_K(w)$ is given by

$$f_K(w) = \begin{cases} \frac{1}{\sqrt{K}} \sin \sqrt{K}w & (K > 0) \\ w & (K = 0) \\ \frac{1}{\sqrt{-K}} \sinh \sqrt{-K}w & (K < 0). \end{cases} \tag{1.70}$$

The propagation equation is easily solved. It is an oscillator equation, so that its general solution is

$$\vec{x} = \vec{A} \cos \sqrt{K}w + \vec{B} \sin \sqrt{K} \quad (K > 0). \tag{1.71}$$

With the boundary conditions $\vec{x}(w = 0) = 0$ and $d\vec{x}/dw|_{w=0} = \vec{\theta}$, we find

$$\vec{x}(w) = \vec{\theta} \sin \sqrt{K}w. \tag{1.72}$$

Generally, for negative and vanishing K, we find

$$\vec{x}(w) = \vec{\theta} f_K(w) \tag{1.73}$$

Since lensing masses are typically much smaller than the Hubble radius, in order to add perturbations space-time can be considered flat in their surroundings, and we can use our earlier result on the deflection angle in the form

$$\frac{d^2\vec{x}}{dw^2} = -\frac{2}{c^2}\vec{\nabla}_\perp \phi \tag{1.74}$$

where it must now be noted that the perpendicular gradient of ϕ must be taken with respect to the comoving coordinates as well. This means

$$\frac{2}{c^2}\vec{\nabla}_\perp \phi = \frac{1}{f_K(w)}\vec{\nabla}_\theta \phi \tag{1.75}$$

The propagation equation changes to

$$\frac{d^2\vec{x}}{dw^2} + K\vec{x} = -\frac{2}{c^2}\vec{\nabla}_\perp \phi \tag{1.76}$$

which now incorporates overall space-time curvature and local perturbations caused by a potential ϕ.

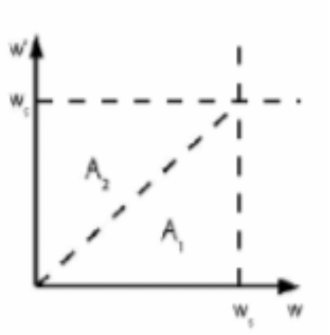

Figure 1.3: Range of validity of the Green function $G(w, w')$

The inhomogeneus oscillator equation can be solved by constructing a Green function $G(w, w')$, which is defined on the square $0 \leq w \leq w_s$, $0 \leq w' \leq w_s$, where w_s is the coordinate distance to the source (see Fig. 1.3). According to the definition of a Green function, $G(w, w')$ must satisfy the following conditions

- $G(w, w')$ is continuously differentiable in both triangles $A_{1,2}$ and satisfies the homogeneous differential equation
- $G(w, w')$ is continuous on the entire square;
- the derivative of $G(w, w')$ with respect to w jumps by 1 on the boundary between A_1 and A_2 ;
- as a function of w, $G(w, w')$ satisfies the homogeneous boundary conditions on the solution.

Accordingly, we set up

$$G(w,w') = \begin{cases} A(w')\cos\sqrt{K}w + B(w')\cos\sqrt{K}w & \text{on} \quad A_1 \\ C(w')\cos\sqrt{K}w + D(w')\cos\sqrt{K}w & \text{on} \quad A_2 \end{cases} \tag{1.77}$$

The homogeneous boundary conditions demand $A = B = 0$. Continuity requires

$$C\cos\sqrt{K}w' + D\sin\sqrt{K}w' = 0 \tag{1.78}$$

and the jump in the derivative implies

$$-C\sin\sqrt{K}w' + D\cos\sqrt{K}w' = \frac{1}{\sqrt{K}}. \tag{1.79}$$

Thus,

$$\begin{aligned} C &= -\frac{1}{\sqrt{K}w'}\sin\sqrt{K}w' \\ D &= \frac{1}{\sqrt{K}w'}\cos\sqrt{K}w'. \end{aligned} \tag{1.80}$$

This implies

$$G(w,w') = \begin{cases} 0 & (w < w') \\ \frac{1}{\sqrt{K}}\sin\sqrt{K}(w-w') & (w > w') \end{cases} \tag{1.81}$$

More generally, i.e. for arbitrary sign of K, we find instead

$$G(w,w') = \begin{cases} 0 & (w < w') \\ f_K(w-w') & (w > w') \end{cases} \tag{1.82}$$

Therefore the general solution of the propagation equation reads

$$\vec{x} = f_K(w)\vec{\theta} - \frac{2}{c^2}\int_0^w dw' f_K(w-w')\vec{\nabla}_\perp\phi. \tag{1.83}$$

As in the single-lens plane approach, we evaluate this integral along the unperturbed path $f_K(w)\vec{\theta}$. The deflection angle is defined as the deviation between the perturbed and the unperturbed path,

$$\vec{\alpha} = \frac{f_K(w)\vec{\theta} - \vec{x}}{f_K(w)} = \frac{2}{c^2}\int_0^w dw' \frac{f_K(w-w')}{f_K(w)}\vec{\nabla}_\perp\phi[f_K(w')\vec{\theta}, w']. \tag{1.84}$$

This is now the deflection angle accumulated along a light path propagating into direction θ out to the coordinate distance w. Hence, we denote it as $\alpha(\theta, w)$. For a spatially flat universe, $K = 0$ and $f_K(w) = w$. Then,

$$\vec{\alpha}(\vec{\theta}, w) = \frac{2}{c^2}\int_0^w dw'(1 - \frac{w'}{w})\vec{\nabla}_\perp\phi(w'\vec{\theta}, w') = \frac{2w}{c^2}\int_0^1 dy(1-y)\vec{\nabla}_\perp\phi(wy\vec{\theta}, wy). \tag{1.85}$$

1.2.2 Effective convergence

In the single lens-plane case, the convergence is one half the divergence of α. Analogously, we define here an effective convergence for large-scale structure lenses,

$$\kappa_{eff}(\vec{\theta}, w) = \frac{1}{2}\vec{\nabla}_{\vec{\theta}}\vec{\alpha}(\vec{\theta}, w) = \frac{1}{c^2}\int dw' \frac{f_K(w')f_K(w-w')}{f_K(w)}\nabla^{2(2)}\phi[f_K(w')\vec{\theta}', w'], \tag{1.86}$$

where $\nabla^{2(2)}$ is the two-dimensional Laplacian with respect to comoving coordinates,

$$\nabla^{2(2)} = \vec{\nabla}_\perp^2 = \frac{\partial^2}{\partial x^2} + \frac{\partial^2}{\partial y^2} \tag{1.87}$$

We now do the same as we did when we introduced the lensing potential: we replace

$$\nabla^{2(2)} \to \nabla^2 = \frac{\partial^2}{\partial x^2} + \frac{\partial^2}{\partial y^2} + \frac{\partial^2}{\partial z^2}, \tag{1.88}$$

and assume that $\partial\phi/\partial z = 0$ at the boundaries of the perturbations. Then, we can write

$$\kappa_{eff} = \frac{1}{c^2}\int_0^w dw' \frac{f_K(w')f_K(w-w')}{f_K(w)}\nabla^2\phi[f_K(w')\vec{\theta}', w'] \tag{1.89}$$

and substitute for $\nabla^2\phi$ using Poisson's equation. In its original form, Poisson's equation reads

$$\nabla_r^2\phi = 4\pi G\rho \tag{1.90}$$

where the Laplacian is now taken with respect to physical coordinates. Introducing the density contrast

$$\delta \equiv \frac{\rho - \bar{\rho}}{\bar{\rho}}, \tag{1.91}$$

we can write

$$\nabla^2\phi = 4\pi G\bar{\rho}(1+\delta)a^2 = 4\pi G\bar{\rho}_0 a^{-1}(1+\delta) \tag{1.92}$$

where we have inserted ρa^{-3} as for ordinary (non-relativistic) matter. Decoupling the potential into a background potential

$$\nabla^2\bar{\phi} = 4\pi G\bar{\rho}_0 a^{-1}, \tag{1.93}$$

and a peculiar (perturbing) potential ϕ, we have

$$\nabla^2\phi = 4\pi G\bar{\rho}_0 a^{-1}\delta, \tag{1.94}$$

Using further

$$\bar{\rho}_0 = \Omega_m \frac{3H_0^2}{8\pi G} \tag{1.95}$$

yields the Poisson equation that we need,

$$\nabla^2\phi = \frac{3}{2}H_0^2\Omega_m\frac{\delta}{a} \tag{1.96}$$

The effective convergence can then be written as

$$\kappa_{eff} = \frac{3\Omega_m}{2}\left(\frac{H_0}{c}\right)^2 \int_0^w dw' \, \frac{f_K(w')f_K(w-w')}{f_K(w)} \frac{\delta[f_K(w')\vec{\theta}', w']}{a(w')} \tag{1.97}$$

where we can appreciate the similarity of the distance factor with the factor $D_L D_{LS}/D_S$ that we had in the single-lens case. If the sources are distributed in redshift or, equivalently, in coordinate distance w, the mean effective convergence is

$$\langle\kappa_{eff}\rangle(\vec{\theta}) = w\int_0^{w_H} dw\, G(w)\kappa_{eff}(\vec{\theta}, w), \tag{1.98}$$

where $G(w)dw$ is the probability to find a source within dw of w. Then we can write

$$\langle\kappa_{eff}\rangle(\vec{\theta}) = \frac{3H_0^2\Omega_m}{2c^2}\int_0^{w_H} dw\, W(w) f_K(w)\frac{\delta[f_K(w)\vec{\theta}, w]}{a(w)}, \tag{1.99}$$

with the effective weight function

$$W(w) = \int_w^{w_H} dw' G(w')\frac{f_K(w'-w)}{f_K(w')}. \tag{1.100}$$

Chapter 2

Neutrino cosmology and matter power spectrum

2.1 Two-point correlation function and power spectrum

2.1.1 Definitions for a generic random field

In this subsection, we define the correlation function and the power spectrum of a generic random field and then we apply these mathematical concepts to the density perturbation field in the following subsection. Without loss of generality, consider a random field $g(\vec{x})$ whose expectation value is zero everywhere (if that was not the case, we could consider the field $g(\vec{x}) - \langle g(\vec{x}) \rangle$ instead, which would have the desired property). Spatial positions $\vec{x}$ have n dimensions, and the field can be either real or complex. A random field $g(\vec{x})$ is called *statistically homogeneous* if it cannot statistically be distinguished from the field $g(\vec{x} + \vec{y})$, where $\vec{y}$ is an arbitrary translation vector. Formally, this means that all the joint multipoint *probability distribution functions* $p(g(\vec{x}_1), g(\vec{x}_2), ...)$ or its *moments*, ensemble averages of products of elements of the field, remain the same under translation of the coordinates $\vec{x}_i$ in space. Similarly, a random field $g(\vec{x})$ is called statistically isotropic if it has the same statistical properties as the random field $g(\mathcal{R}\vec{x})$, where $\mathcal{R}$ is an arbitrary rotation matrix in n dimensions. Namely, this means that $p(g(\vec{x}_1), g(\vec{x}_2), ...)$ is invariant under spatial rotations. Restricting our attention to homogeneous and isotropic random fields, we note that the two-point correlation function

$$\langle g(\vec{x}) g^*(\vec{y}) \rangle = \xi_{gg}(|\vec{x} - \vec{y}|) \tag{2.1}$$

can only depend on the absolute value of the difference vector between the two points $\vec{x}$ and $\vec{y}$. Note that ξ_{gg} is real, even if g is complex. This can

be seen by taking the complex conjugate of Eq. 2.1, which is equivalent to interchanging $\vec{x}$ and $\vec{y}$, leaving the right-hand-side unaffected.
We define the Fourier-transform pair of g as

$$\hat{g}(\vec{k}) = \int_{\mathbb{R}^n} \mathrm{d}^n x \, g(\vec{x}) e^{\mathrm{i}\vec{x}\cdot\vec{k}}; \quad g(\vec{x}) = \int_{\mathbb{R}^n} \frac{\mathrm{d}^n k}{(2\pi)^n} \, \hat{g}(\vec{k}) e^{-\mathrm{i}\vec{x}\cdot\vec{k}}. \tag{2.2}$$

We now calculate the correlation function in Fourier space,

$$\left\langle \hat{g}(\vec{k})\hat{g}^*(\vec{k'}) \right\rangle = \int_{\mathbb{R}^n} \mathrm{d}^n x \, e^{\mathrm{i}\vec{x}\cdot\vec{k}} \int_{\mathbb{R}^n} \mathrm{d}^n x' \, e^{-\mathrm{i}\vec{x}'\cdot\vec{k}'} \left\langle g(\vec{x}) g^*(\vec{x}') \right\rangle. \tag{2.3}$$

Using Eq. 2.1 and substituting $\vec{x}' = \vec{x} + \vec{y}$, this becomes

$$\begin{aligned} \left\langle g(\vec{x}) g^*(\vec{x}') \right\rangle &= \int_{\mathbb{R}^n} \mathrm{d}^n x \, e^{\mathrm{i}\vec{x}\cdot\vec{k}} \int_{\mathbb{R}^n} \mathrm{d}^n y e^{-\mathrm{i}(\vec{x}+\vec{y})\cdot\vec{k}'} \xi_{gg}(|\vec{y}|) \\ &= (2\pi)^n \delta_D(\vec{k} - \vec{k}') \int_{\mathbb{R}^n} \mathrm{d}^n y \, e^{-\mathrm{i}\vec{y}\cdot\vec{k}} \xi_{gg}(|\vec{y}|) \\ &= (2\pi)^n \delta_D(\vec{k} - \vec{k}') P_g(|\vec{k}|). \end{aligned} \tag{2.4}$$

In the final step, we defined the power spectrum of the statistically homogeneous and isotropic random field g,

$$P_g(|\vec{k}|) = \int_{\mathbb{R}^n} \mathrm{d}^n y \, e^{-\mathrm{i}\vec{y}\cdot\vec{k}} \xi_{gg}(|\vec{y}|) \tag{2.5}$$

which is the Fourier transform of the two-point correlation function. Isotropy of the random field implies that P_g can only depend on the modulus of k.
Gaussian random fields are characterised by the property that the probability distribution of any linear combination of the random field $g(\vec{x})$ is Gaussian. More generally, the joint probability distribution of a number M of linear combinations of the random variable $g(\vec{x}_i)$ is a multivariate Gaussian. This is equivalent to requiring that the Fourier components $\hat{g}(\vec{k})$ are mutually statistically independent, and that the probability densities for the $\hat{g}(\vec{k})$ are Gaussian with dispersion $P_g(|\vec{k}|)$. Thus, a Gaussian random field is fully characterised by its power spectrum.

2.1.2 Specialisation to the cosmological density field

Now we will apply the mathematical notions of the last subsection to the following problem: how do we describe the fluctuations of density in the Universe that caused the matter inhomogeneities we can observe around us? It turns out that these fluctuations can be described by a statistically homogeneous random field. First of all let us define the cosmological density perturbation field as:

$$\delta(\vec{x}) \equiv \frac{\rho(\vec{x}) - \bar{\rho}}{\bar{\rho}} \tag{2.6}$$

This formula just states that $\delta(\vec{x})$ is the fractional deviation of the cosmological density field $\rho(x)$ above a certain average $\bar{\rho}$ at position $\vec{x}$. Since we assume our Universe to be homogeneous and isotropic, the average of a cosmological quantity cannot depend on position or direction, as this would indicate a preferred point or axis in space. Formally speaking, we have to perform this average over an ensemble of different realizations of the Universe, with the same conditions, if we want to talk about statistical processes. Since this is not possible and we can only observe a single realization of our Universe, the best we can do is to average over largely separated regions of space which, according to our theories, should be completely causally disconnected, so that the bigger the volume we average over, the best we approximate a true ensemble average. Fields which satisfy the property that the ensemble average equals the volume average are called *ergodic* and the validity of this hypothesis is taken as an axiom for cosmology (see Peacock (1999)). The density contrast field $\delta(\vec{x})$ changes sign and magnitude depending on its position, but in order to be statistically homogeneous and isotropic, its ensemble averages of local density products p, for example for $p = 3$, $\langle\delta(\vec{x}_1)\delta(\vec{x}_2)\delta(\vec{x}_3)\rangle$, have to be independent under translations and rotations of the coordinates $\vec{x}_1, \vec{x}_2, \vec{x}_3$ (see Bernardeau et al. (2002)). For example the variance $\left\langle\delta^2\right\rangle$, which is just the second moment of δ at the same value of $\vec{x}$, should only depend on the norm of this vector.

2.1.3 N-point correlations and Gaussian random fields

Correlation functions are directly related to the multipoint probability function, in fact they can be defined from it, as we show here for the density field. The physical interpretation of the two-point correlation function is a measure of the excess over random probability of finding a neighbouring element in a volume $\mathrm{d}V_1$ at a distance r from another given element in a volume $\mathrm{d}V_2$:

$$\mathrm{d}P = \rho_0^2[1 + \xi(r)]\mathrm{d}V_1\mathrm{d}V_2 \tag{2.7}$$

so that if clustering ($\xi \neq 0$) is present, the probability will be above the usual Poisson value, which is just proportional to the density squared. The n-point correlation functions are then interpreted as the excess probability of finding an n-tuplet of objects in n specified volumes and they can be written as:

$$\mathrm{d}P = \rho_0^n[1 + \xi^{(n)}]\mathrm{d}V_1...\mathrm{d}V_n \tag{2.8}$$

Since the two-point function is proportional to the product of the density field at the n-points, then the n-point correlation function is just:

$$1 + \xi^{(n)} = \left\langle \prod_i^n (1 + \delta_i) \right\rangle \tag{2.9}$$

Expanding the product for $n = 3$, we get:

$$\xi^{(3)} = \xi(r_{12}) + \xi(r_{13}) + \xi(r_{32}) + \zeta(r_1, r_2, r_3) \tag{2.10}$$

The term $\zeta = \langle \delta_1 \delta_2 \delta_3 \rangle$ expresses just the excess correlation between three objects that is not taken into account by the two-point correlations. This is called the reduced or *connected* three-point correlation functions, because of the analogy to the Green functions of quantum field theory.
For a Gaussian random field, the Wick theorem implies that the only non vanishing p-moments δ^p are the even ones, while the odd-valued products vanish. We have then:

$$\left\langle \delta(\vec{k}_1, ..., \delta(\vec{k}_{2p+1}) \right\rangle = 0 \tag{2.11}$$

$$\left\langle \delta(\vec{k}_1, ..., \delta(\vec{k}_{2p}) \right\rangle = \sum_{\text{associations}} \prod_{\text{p pairs(i,j)}} \left\langle \delta(\vec{k_i}) \delta(\vec{k_j}) \right\rangle \tag{2.12}$$

This just states that all possible statistical properties of the random variables $\delta(\vec{k})$ are completely determined by the form of the power spectrum $P(k)$. This implies that at least in the linear regime, a given cosmological model will be entirely determined by the power spectrum, if one is interested only in the behaviour of dark matter under gravitational evolution.
However, the dynamics of gravitational instability is a highly nonlinear process and therefore nonlinear evolution leads inevitably to the development of non-Gaussian features in the density field, specially at very small scales and late times. This leads to a subtle problem, since for weakly non-Gaussian fields the whole hierarchy of n-point correlation functions is needed to describe the statistical properties in a complete way. The general n-point correlation function can be written as:

$$\xi_n(\vec{x}_1, ..., \vec{x}_n) = \langle \delta(\vec{x}_1), ..., \delta(\vec{x}_n) \rangle_c \tag{2.13}$$

The connected ensemble average of products, also called the cumulants (if they are located at the same point), are defined as the difference between the n-th moment and all possible different combinations of connected ensemble product averages of order less than n, between the n points. As an example we write here the first four terms:

$$\langle\delta\rangle_c = \langle\delta\rangle \tag{2.14}$$

$$\left\langle\delta^2\right\rangle_c = \left\langle\delta^2\right\rangle - \langle\delta\rangle_c^2 \equiv \sigma^2 \tag{2.15}$$

$$\left\langle\delta^3\right\rangle_c = \left\langle\delta^3\right\rangle - 3\left\langle\delta^2\right\rangle_c \langle\delta\rangle_c - \langle\delta\rangle_c^3 \tag{2.16}$$

$$\left\langle\delta^4\right\rangle_c = \left\langle\delta^4\right\rangle - 4\left\langle\delta^3\right\rangle_c \langle\delta\rangle - 3\left\langle\delta^2\right\rangle_c^2 - 6\left\langle\delta^2\right\rangle_c \langle\delta\rangle_c^2 - \langle\delta\rangle_c^4 \tag{2.17}$$

This can also be visualized for clearer understanding, as in Fig. 2.1, where the connected components are represented by single points in the case of $\langle\delta\rangle_c$, or points joined by lines for higher order cumulants. If the average of the density fluctuation is regarded as zero, as in cosmology, then the single points do not contribute. To understand Eq. 2.16, compare it with Fig. 2.2. The moment of order 3 is just the sum of a triangle $\left\langle\delta^3\right\rangle_c$, plus three times a line $\left\langle\delta^2\right\rangle_c$ with a single point $\langle\delta\rangle_c$ plus 3 individual points $\langle\delta\rangle_c^3$.
When nonlinearities in gravitational interactions start inducing mode couplings between different scales, the Gaussianity is broken and we need an infinite hierarchy of correlation functions, therefore the power spectrum is not the only quantity encoding cosmological information. The next order statistical quantity at $n = 3$ is the bispectrum and is usually denoted $B(\vec{k}_1, \vec{k}_2, \vec{k}_3)$ and measures correlations between three different points. In the halo model of structure formation, this yields interesting insights into the bias parameters [see Cooray and Sheth (2002)].

2.2 Matter power spectrum

The current large scale structure of the Universe is probed by the matter power spectrum, introduced in the last section. Defined as the Fourier transform of the matter correlation function, it describes the density contrast of the universe as a function of scale. On large scales, gravity competes with cosmic expansion, and structures grow according to linear theory. In this regime, the density contrast field is Gaussian, Fourier modes evolve independently, and the power spectrum is sufficient to completely describe the density field. On small scales, gravitational collapse is non-linear: higher-order statistics are necessary to describe the full field at small scales. The shape of the matter power spectrum is affected in a scale-dependent way by the free-streaming caused by small neutrino masses of $O(\mathrm{eV})$ and thus it is the key observable to constrain m_ν with cosmological methods.

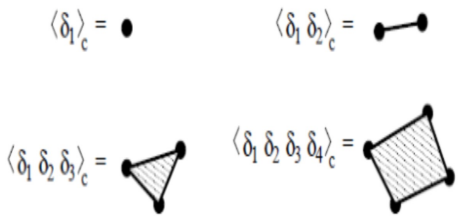

Figure 2.1: Representation of the connected part of the moments

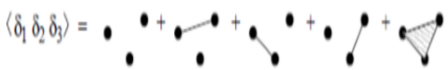

Figure 2.2: Three-point moment in terms of connected parts

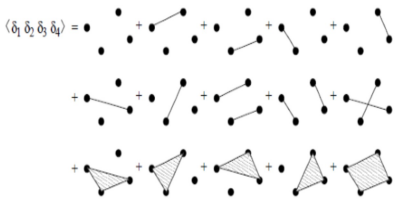

Figure 2.3: Four-point moment in terms of connected parts

2.2.1 Neutrino free-streaming

After thermal decoupling, relic neutrinos constitute a collisionless fluid, where the individual particles free-stream with a characteristic velocity that, in average, is the thermal velocity v_{th}. It is possible to define a horizon as the typical distance on which particles travel between time t_i and t. When the Universe was dominated by radiation or matter $t \gg t_i$, this horizon is, as usual, asymptotically equal to v_{th}/H, up to a numerical factor of order one. Similarly to the definition of the Jeans wavelength, we can define the neutrino free-streaming wavenumber and wavelength as

$$\begin{aligned} k_{FS}(t) &= \left(\frac{4\pi G\bar{\rho}(t)a^2(t)}{v_{th}^2}\right)^{1/2}, \\ \lambda_{FS}(t) &= 2\pi\frac{a(t)}{k_{FS}(t)} = 2\pi\sqrt{\frac{2}{3}}\frac{v_{th}(t)}{H(t)}. \end{aligned} \tag{2.18}$$

As long as neutrinos are relativistic, they travel at the speed of light and their free-streaming length is simply equal to the Hubble radius. When they become non-relativistic, their thermal velocity decays like

$$v_{th} \equiv \frac{\langle p\rangle}{m} \sim \frac{3.15T_\nu}{m} = \frac{3.15T_\nu^0}{m}\left(\frac{a_0}{a}\right) \simeq 158(1+z)\left(\frac{1eV}{m}\right)\mathrm{km\,s^{-1}}, \tag{2.19}$$

where we used for the present neutrino temperature $T_\nu^0 \simeq (4/11)^{1/3}\,T_\gamma^0$ and $T_\gamma^0 \simeq 2.726K$. This gives for the free-streaming wavelength and wavenumber during matter or Λ domination

$$\begin{aligned} k_{FS}(t) &= 0.8\frac{\sqrt{\Omega_\Lambda + \Omega_m(1+z)^3}}{(1+z)^2}(\frac{m}{1eV})\,h\,\mathrm{Mpc}^{-1}, \\ \lambda_{FS}(t) &= 8\frac{1+z}{\sqrt{\Omega_\Lambda + \Omega_m(1+z)^3}}(\frac{1eV}{m})\,h^{-1}\,\mathrm{Mpc}, \end{aligned} \tag{2.20}$$

where Ω_Λ and Ω_m are the cosmological constant and matter density fractions, respectively, evaluated today. After the non-relativistic transition and during matter domination, the free-streaming length continues to increase, but only like $(aH)^{-1} \propto t^{-1/3}$, i.e. more slowly than the scale factor $a \propto t^{2/3}$. Therefore, the comoving free-streaming length λ_{FS}/a actually decreases like $(a^2H)^{-1} \propto t^{-1/3}$. As a consequence, for neutrinos becoming non-relativistic during matter domination, the comoving free-streaming wavenumber passes through a minimum k_{nr} at the time of the transition, i.e. when $m = \langle p\rangle = 3.15\,T_\nu$ and $a_0/a = (1+z) = 2.0\cdot 10^3(m/1eV)$. This minimum value is found to be

$$k_{nr} \simeq 0.018\,\Omega_m^{1/2}\left(\frac{m}{1eV}\right)^{1/2}\,h\,\mathrm{Mpc}^{-1}. \tag{2.21}$$

As we will see in more detail in the following subsection, the physical effect of free-streaming is to damp small-scale neutrino density fluctuations: neutrinos cannot be confined into (or kept outside of) regions smaller than the free-streaming length, because their velocity is greater than the escape velocity from gravitational potential wells on those scales. Instead, on scales much larger than the free-streaming scale, the neutrino velocity can be effectively considered as vanishing, and after the non-relativistic transition the neutrino perturbations behave like CDM perturbations. In particular, modes with $k < k_{nr}$ are never affected by free-streaming and evolve like being in a pure ΛCDM model.

2.2.2 Impact of massive neutrinos on the matter power spectrum

The small initial cosmological perturbations evolve within the linear regime at early times. During matter domination, the smallest cosmological scales start evolving non-linearly, leading to the formation of the structures we see today. We will emphasize the main effects caused by massive neutrinos on linear scales in the framework of the standard cosmological scenario: a Λ Mixed Dark Matter (ΛMDM) model, where Mixed refers to the inclusion of some HDM component. On large scales (i.e. on wavenumbers smaller than the value k_{nr} defined in the previous subsection), neutrino free-streaming can be ignored, and neutrino perturbations are indistinguishable from CDM perturbations. On those scales, the matter power spectrum $P(k, z)$ can be shown to depend only on the matter density fraction today (including neutrinos), Ω_m, and on the primordial perturbation spectrum. If the neutrino mass is varied with Ω_m fixed, the large-scale power spectrum remains invariant.

On small scales such that $k > k_{nr}$, the matter power spectrum is affected by neutrino masses for essentially three reasons:

1. massive neutrinos do not cluster on those scales. The matter power spectrum can be expanded as a function of the three non-relativistic species,

$$P(k,z) = \left\langle \left| \frac{\delta\rho_{\rm cdm} + \delta\rho_b + \delta\rho_\nu}{\rho_{\rm cdm} + \rho_b + \rho_\nu} \right|^2 \right\rangle = \Omega_m^{-2} \left\langle \left| \Omega_{\rm cdm}\delta_{\rm cdm} + \Omega_b\delta_b + \Omega_\nu\delta_\nu \right|^2 \right\rangle \tag{2.22}$$

   On scales of interest and in the recent universe, baryon and CDM fluctuations are equal to each other, while $\delta_\nu \ll \delta_{\rm cdm}$. Hence, even if the evolution of $\delta_{\rm cdm}$ was not affected by neutrino masses (which is not the case, see the remaining two points below), the power spectrum would be reduced by a factor $(1 - f_\nu)^2$, with

$$f_\nu \equiv \frac{\Omega_\nu}{\Omega_m}; \tag{2.23}$$

2. the redshift of radiation-to-matter equality z_{eq} or the baryon-to-CDM ratio $\omega_b/\omega_{\rm cdm}$ might be slightly affected by neutrino masses, with a potential impact on the small-scale matter power spectrum. This depends very much on which other parameters are kept fixed when the neutrino mass varies. If neutrino masses are smaller than roughly 0.5 eV, they are still relativistic at the time of radiation-to-matter equality, and the redshift of equality depends on $\omega_b + \omega_{\rm cdm}$, not on ω_m. It is possible to increase the total mass $M_\nu = \sum_i m_{\nu_i}$ and ω_m with fixed parameters $\Omega_m, \omega_b, \omega_{\rm cdm}$ (provided that the Hubble parameter also increases like the square root of ω_m). In that case, there is no significant impact of massive neutrinos on the matter power spectrum through background effects, i.e. through a change in the homogeneous cosmological evolution. However, there are some important perturbation effects that we will summarize in the following point;

3. the growth rate of cold dark matter perturbations is reduced through an absence of gravitational back-reaction effects from free-streaming neutrinos. This growth rate is set by an equation of the type

$$\delta''_{\rm cdm} + \frac{a'}{a}\delta_{\rm cdm} = -k^2\psi \tag{2.24}$$

where $\delta_{\rm cdm}$ stands for the CDM relative density perturbation in Fourier space, and ψ for the metric perturbation playing the role of the Newtonian potential inside the Hubble radius. There is a similar equation for decoupled baryons, and very soon after baryon decoupling we can identify $\delta_b = \delta_{\rm cdm}$ on scales of interest. The right-hand side represents gravitational clustering, and is given by the Poisson equation as a function of the total density fluctuation. The second term on the left-hand side represents Hubble friction, i.e. the fact that the cosmological expansion enhances distances, reduces gravitational forces and slows down gravitational clustering. The coefficient a'/a is given by the Friedmann equation as a function of the total background density. In a universe such that all species present in the Friedmann equation cluster, as it is the case in a matter-dominated universe with $\delta\rho_{total} \simeq \delta\rho_{\rm cdm} + \delta\rho_b$ and $\bar\rho_{total} = \bar\rho_{\rm cdm} + \bar\rho_b$, the solution is simply given by $\delta_{\rm cdm} \propto a$: the so-called linear growth factor is proportional to the scale factor. But whenever one of the species contributing to the background expansion does not cluster efficiently, it can be neglected in the Poisson equation. In that case, the term on the right-hand side becomes smaller with respect to the Hubble friction term, and CDM (as well as baryons) clusters at a slower rate.

This is the case in presence of massive neutrinos and for $k \gg k_{nr}$: the linear growth rate during matter domination is then equal to $a^{1-3/5f_\nu}$. During Λ domination, this effect sums up with that of the cosmological constant (or of any non-clustering dark energy), which also tends to reduce the growth rate for the very same reason.

In summary, the small-scale matter power spectrum $P(k \geq k_{nr})$ is reduced in presence of massive neutrinos for at least two reason: by the absence of neutrino perturbations in the total matter power spectrum, and by a slower growth rate of CDM/baryon perturbations at late times. The third effect has the largest amplitude. At low redshift $z \simeq 0$, the step-like suppression of $P(k)$ starts at $k \geq k_{nr}$ and saturates at $k \sim 1\,h\,\mathrm{Mpc}^{-1}$ with a constant amplitude $\Delta P(k)/P(k) \simeq -8f_\nu$. This result was obtained by fitting numerical simulations [Hu et al. (1997)], but a more accurate approximation can be derived analytically [Lesgourgues et al. (2013)]. As mentioned in the second point above, neutrino masses can have additional indirect effects through a change in the background evolution, depending on which cosmological parameters are kept fixed when M_ν varies. When fitting data, one can use analytical approximations to the full MDM or ΛMDM matter power spectrum, valid for arbitrary scales and redshifts, as listed in Lesgourgues and Pastor (2006). However, nowadays the analyses are performed using the matter power spectra calculated by Boltzmann codes such as CAMB [Lewis et al. (2000)] or CLASS [Lesgourgues and Tram (2011)], that solve numerically the evolution of the cosmological perturbations. The step-like suppression of the matter power spectrum induced by various values of f_ν is shown in Fig. 2.4.

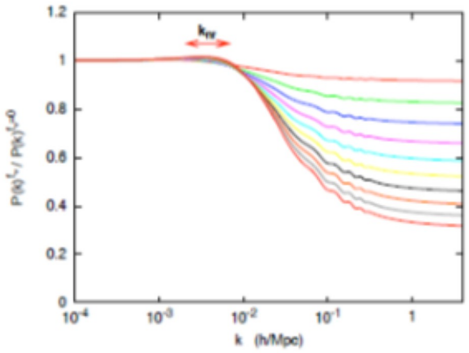

Figure 2.4: Ratio of the matter power spectrum including three degenerate massive neutrinos with density fraction f_ν to that with three massless neutrinos. The parameters ω_m, Ω_Λ are kept fixed, and from top to bottom the curves correspond to $f_\nu = 0.01.0.02, 0.03, ...0.10$. The individual masses m_ν range from 0.046 to 0.46 eV, and the scale k_{nr} from $2.1 \times 10^{-3} h$ Mpc^{-1} to $6.7 \times 10^{-3} h$ Mpc^{-1}.

Chapter 3

Quadratic estimator basics

We now come to the description of the quadratic estimator developed in this thesis work. The estimator acts on weak lensing data sets and produces estimates of the matter power spectrum $P(k)$. It is the first quadratic estimator derived for weak lensing measurements: nevertheless, there already exist in literature examples of similar estimators for power spectra, acting on different data sets. We present two cases of particular interest, Tegmark (1997) and Tegmark et al. (2004), where the same quadratic estimator is applied to the CMB and galaxies case, respectively. This thesis work is an extension of this method to the weak lensing case, where the situation is in principle more complicated, due to the fact that weak lensing constitutes an integrated effect along the line of sight. This makes it not at all clear that the technique will succeed. In this chapter we introduce the method followed in the above cited papers, while in the next chapter we specialise the discussion to the weak lensing case, introducing the mathematical details of our estimator.

3.1 The CMB case

3.1.1 Preliminaries

In Tegmark (1997) a quadratic estimator for the CMB angular power spectrum C_l is presented. The estimation of C_l is crucial in cosmology as it allows measurements of the cosmological parameters, from which the power spectrum depends, with great accuracy. As we will see in detail later on, the quadratic estimator presented in the paper has the alluring property of producing the smallest error bars on the estimated C_l. It also turns out to be computationally faster than other methods, such as the nonlinear maximum-likelihood method or the Karhunen-Loève data compression method [Bond (1995), Tegmark et al. (1997)], both requiring computations scaling with n^3, where n is the number of map pixels. In fact, the CPU time needed for applying the maximum-likelihood method directly to a map scales as n^3, since

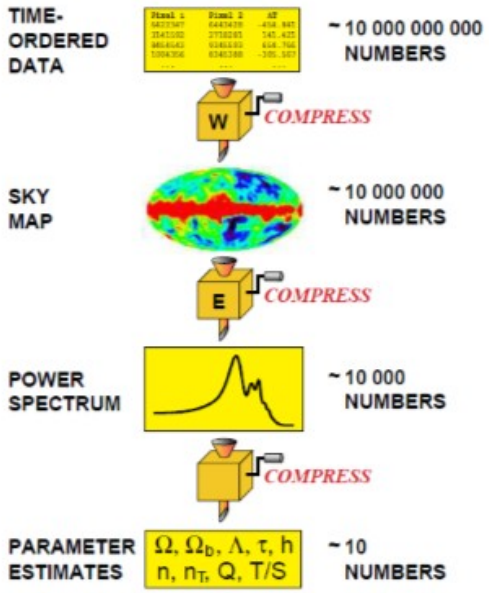

Figure 3.1: Pipeline in the estimation of cosmological parameters from CMB data. Figure from Tegmark (1997).

it involves computing determinants of $n \times n$ non-sparse covariance matrices. The Karhunen-Loève method also scales as n^3, requiring the diagonalization of an $n \times n$ matrix. Therefore, both these methods show problems in terms of computational feasibility as n becomes large. The quadratic estimator, instead, scales as n^2 in its crucial steps rather than n^3.

Since a likelihood analysis, measuring the cosmological parameters from time-ordered data, is computationally unfeasible, the power spectrum estimation plays a key role in splitting the extraction of the cosmological parameters into feasible steps. Under the inflationary paradigm (see Liddle and Lyth (2000) for a review), the temperature fluctuations are Gaussian, which means that the harmonic coefficients have Gaussian distributions with mean zero and variance given by C_l. In this case, all we need to characterise the statistics of our temperature fluctuations field is the power-spectrum

- all higher-point statistics will be zero and contain no extra information. Therefore, provided that all the cosmological information that was present in the map is still retained in the estimated power spectrum, the method provides a measurement of the parameters with the same smallest error bars of the likelihood technique. Thus, the power spectrum estimator becomes only one of the steps characterising the pipeline described in Fig. 3.1, where the data-compression performed at every step ultimately leads to a more feasible, yet highly accurate, estimate of the cosmological parameters.
It is clear then that the quality of retaining as much information as possible is vital for the validity of the estimator and the whole pipeline. In this regard the Fisher information matrix formalism [Tegmark et al. (1997)] offers a simple and useful way to measure how much information the methods in the pipeline destroy. Given any set of cosmological parameters of interest, their Fisher matrix $\mathbf{F}$ gives the smallest error bars with which the parameters can be measured from a given data set, as $\mathbf{F}^{-1}$ can be thought of as the best possible covariance matrix for the measurement errors on the parameters. The Cramér-Rao inequality shows that no unbiased method can measure the i-th parameter with error bars smaller than $1/\sqrt{\mathbf{F}_{ii}}$.
If the probability distribution f for the data set $\vec{x}$ (the pixels temperatures in a sky map, in the CMB case) depends on some parameters $\lambda_1, \lambda_2, ...$, then the Fisher information matrix for these parameters is defined as [Tegmark et al. (1997)]

$$\mathbf{F}_{ij}^{\lambda} \equiv -\left\langle \frac{\partial^2}{\partial\alpha_i \partial\alpha_j} \ln f \right\rangle \tag{3.1}$$

Since f is a probability distribution over $\vec{x}$, $\int f(\vec{x}; \lambda_1, \lambda_2, ...)\mathrm{d}^n x = 1$ for any choice of the parameter vector λ_i. Differentiating this identity, we obtain

$$\left\langle \frac{\partial}{\partial\lambda_i} ln f \right\rangle = \int \frac{\partial ln f}{\partial\lambda_i} f \mathrm{d}^n x = \frac{\partial}{\partial\lambda_i} \int f \mathrm{d}^n x = 0 \tag{3.2}$$

Using this result and the chain rule, we find that if the parameter set λ_i depends on some other parameter set θ_j, then the Fisher matrix for these new parameters is given by

$$\mathbf{F}^{\theta} = \mathbf{J}^t \mathbf{F}^{\lambda} \mathbf{J} \tag{3.3}$$

where the Jacobian matrix (not necessarily square) is

$$\mathbf{J}_{ij} \equiv \frac{\partial\lambda_i}{\partial\theta_j} \tag{3.4}$$

The transformation rule 3.3 holds regardless of whether the probability distribution is Gaussian or not. However, if the CMB fluctuations $\vec{x}$ are Gaussian and isotropic, then we know that their probability distribution is entirely determined by the power spectrum. This means that if we choose the parameters λ_i to be the power spectrum coefficients C_l, the Fisher matrix for any set of cosmological parameters can be computed directly from $\mathbf{F}^C$, the Fisher matrix for the power spectrum itself:

$$\mathbf{F}^\theta = \mathbf{J}^t \mathbf{F}^C \mathbf{J} \tag{3.5}$$

So one does not need to compute and compare large numbers of Fisher matrices for various parameter combinations, since they can all be computed directly from $\mathbf{F}^C$. We will let $\hat{C}_l$ denote estimates of the true angular power spectrum C_l. The estimates are unbiased if they satisfy

$$\left\langle \hat{C}_l \right\rangle = C_l \tag{3.6}$$

According to the Cramér-Rao inequality, to test if a power spectrum estimation method is lossless, we compute the covariance matrix

$$\mathbf{V}_{ll'} \equiv \left\langle \hat{C}_l \hat{C}_{l'} \right\rangle - \left\langle \hat{C}_l \right\rangle \left\langle \hat{C}_{l'} \right\rangle \tag{3.7}$$

and check if it equals the inverse of the Fisher matrix $\mathbf{F}^C$, for which we now derive an explicit expression in the Gaussian case. We will follow closely the approach of Tegmark et al. (1997). Let us consider a Gaussian probability distribution, i.e., indicating with $\mathcal{L}$ the negative of the natural logarithm of the likelihood function, a distribution for which

$$2\mathcal{L} = \ln\det\mathbf{C} + (\mathbf{x} - \mu)\mathbf{C}^{-1}(\mathbf{x} - \mu)^t, \tag{3.8}$$

where in general both the mean vector μ and the covariance matrix

$$\mathbf{C} = \left\langle (\mathbf{x} - \mu)(\mathbf{x} - \mu)^t \right\rangle \tag{3.9}$$

depend on the model parameters $\mathbf{\Theta}$. Defining the data matrix

$$\mathbf{D} \equiv (\mathbf{x} - \mu)(\mathbf{x} - \mu)^t \tag{3.10}$$

and using the matrix identity $\ln\det\mathbf{C} = \mathrm{Tr}\ln\mathbf{C}$, we can rewrite equation 3.8 as

$$2\mathcal{L} = Tr[\ln\mathbf{C} + \mathbf{C}^{-1}\mathbf{D}]. \tag{3.11}$$

Since $\mathbf{C}$ is a symmetric matrix for all values of the parameters, all the derivatives $\frac{\partial\mathbf{C}}{\partial\theta_i}$, $\frac{\partial\mathbf{C}}{\partial\theta_i\partial\theta_j}$... will also be symmetric matrices. Using the matrix identities $\frac{\partial\mathbf{C}^{-1}}{\partial\theta_i} = -\mathbf{C}^{-1}\frac{\partial\mathbf{C}}{\partial\theta_i}\mathbf{C}^{-1}$ and $\frac{\partial ln\mathbf{C}}{\partial\theta_i} = \mathbf{C}^{-1}\frac{\partial\mathbf{C}}{\partial\theta_i}$, we thus obtain

$$2\frac{\partial\mathcal{L}}{\partial\theta_i} = Tr\left[\mathbf{C}^{-1}\frac{\partial\mathbf{C}}{\partial\theta_i} - \mathbf{C}^{-1}\frac{\partial\mathbf{C}}{\partial\theta_i}\mathbf{C}^{-1}\mathbf{D} + \mathbf{C}^{-1}\frac{\partial\mathbf{D}}{\partial\theta_i}\right]. \tag{3.12}$$

When evaluating $\mathbf{C}$ and μ at the true parameter values, we have $\langle\mathbf{x}\rangle = \mu$ and $\langle\mathbf{x}\mathbf{x}^t\rangle = \mathbf{C} + \mu\mu^t$, which gives

$$\begin{cases} \langle\mathbf{D}\rangle & = \mathbf{C} \\ \left\langle\frac{\partial\mathbf{D}}{\partial\theta_i}\right\rangle & = 0 \\ \left\langle\frac{\partial\mathbf{D}}{\partial\theta_i\partial\theta_j}\right\rangle & = \frac{\partial\mu}{\partial\theta_i}\frac{\partial\mu}{\partial\theta_j}^t + \frac{\partial\mu}{\partial\theta_j}\frac{\partial\mu}{\partial\theta_i}^t. \end{cases} \tag{3.13}$$

Applying the chain rule to equation 3.12, we find

$$\begin{aligned} 2\frac{\partial^2\mathcal{L}}{\partial\theta_i\partial\theta_j} = \mathrm{Tr}[& -\mathbf{C}^{-1}\frac{\partial\mathbf{C}}{\partial\theta_i}\mathbf{C}^{-1}\frac{\partial\mathbf{C}}{\partial\theta_j} + \mathbf{C}^{-1}\frac{\partial^2\mathbf{C}}{\partial\theta_i\partial\theta_j} \\ & + \mathbf{C}^{-1}\left(\frac{\partial\mathbf{C}}{\partial\theta_i}\mathbf{C}^{-1}\frac{\partial\mathbf{C}}{\partial\theta_j} + \frac{\partial\mathbf{C}}{\partial\theta_j}\mathbf{C}^{-1}\frac{\partial\mathbf{C}}{\partial\theta_i}\right)\mathbf{C}^{-1}\mathbf{D} \\ & - \mathbf{C}^{-1}\left(\frac{\partial\mathbf{C}}{\partial\theta_i}\mathbf{C}^{-1}\frac{\partial\mathbf{D}}{\partial\theta_j} + \frac{\partial\mathbf{C}}{\partial\theta_j}\mathbf{C}^{-1}\frac{\partial\mathbf{D}}{\partial\theta_i}\right)\mathbf{C}^{-1}\mathbf{D} \\ & - \mathbf{C}^{-1}\frac{\partial^2\mathbf{C}}{\partial\theta_i\partial\theta_j}\mathbf{C}^{-1}\mathbf{D} + \mathbf{C}^{-1}\frac{\partial^2\mathbf{D}}{\partial\theta_i\partial\theta_j}] \end{aligned}$$

Substituting this and equation 3.13 into equation 3.1 and using the trace identity $\mathrm{Tr}[\mathbf{AB}] = \mathrm{Tr}[\mathbf{BA}]$, the Fisher information matrix reduces to

$$\mathbf{F}_{ij} = \frac{1}{2}\mathrm{Tr}[\mathbf{C}^{-1}\frac{\partial\mathbf{C}}{\partial\theta_i}\mathbf{C}^{-1}\frac{\partial\mathbf{C}}{\partial\theta_i}] + \mathbf{C}^{-1}\mathbf{M}_{ij} \tag{3.14}$$

where $\mathbf{M}_{ij} = \left\langle\frac{\partial\mathbf{D}}{\partial\theta_i\partial\theta_j}\right\rangle = \frac{\partial\mu}{\partial\theta_i}\frac{\partial\mu}{\partial\theta_j}^t + \frac{\partial\mu}{\partial\theta_j}\frac{\partial\mu}{\partial\theta_i}^t$.
Let us now give an explicit expression for the CMB case, considering our data to be the temperature fluctuations $\frac{\Delta T}{T}$. With the standard assumption that the CMB fluctuations are isotropic, we have $\mu = 0$. We have the following expression for the covariance matrix

$$\mathbf{C} \equiv \left\langle \mathbf{x}\mathbf{x}^t \right\rangle = \mathbf{N} + \sum_l \mathbf{P}^l \mathbf{C}_l, \tag{3.15}$$

where $\mathbf{N}$ denotes the noise covariance matrix and the matrices $\mathbf{P}^l$ are defined as

$$\mathbf{P}^l_{ij} \equiv \frac{2l+1}{4\pi} P_l(\hat{\mathbf{r}}_i \cdot \hat{\mathbf{r}}_j). \tag{3.16}$$

Here the P_l denote Legendre polynomials and $\hat{\mathbf{r}}_i$ is a unit vector pointing in the direction of pixel i. Thus $\frac{\partial \mathbf{C}}{\partial C_l} = \mathbf{P}^l$, and equation 3.14 yields

$$\mathbf{F}^C_{ll'} = \frac{1}{2}\mathrm{Tr}\left[\mathbf{C}^{-1}\frac{\partial \mathbf{C}}{\partial C_l}\mathbf{C}^{-1}\frac{\partial \mathbf{C}}{\partial C_{l'}}\right] \tag{3.17}$$

3.1.2 The quadratic estimator

In Tegmark (1997) the author proposes a lossless estimator that is a quadratic function of the pixels, taking the form

$$\hat{C}_l = \mathbf{x}^t \mathbf{E}^l \mathbf{x} - b_l. \tag{3.18}$$

Here $\mathbf{x}$ is the data set consisting, in the CMB case, of pixels temperatures in a sky map, while the symmetric matrix $\mathbf{E}^l$ and the constant b_l are the weights and the de-bias term to be found, respectively.
Given this generic quadratic combination of the pixels, the goal is to find the weights and the de-bias term that give the best quadratic estimator of the power spectrum, namely the one with the smallest error bars. The de-bias term is found by inserting Eq. 3.15 in 3.18 and requiring the estimator to be unbiased, $\left\langle \hat{C}_l \right\rangle = C_l$. This leads to the following expression for b_l:

$$b_l = \mathrm{Tr}\left(\mathbf{N}\mathbf{E}^l\right) \tag{3.19}$$

and we are left with:

$$\left\langle \hat{C}_l \right\rangle = \sum_{l'} \mathbf{W}_{ll'} \mathbf{C}_{l'} \tag{3.20}$$

where we have defined the Window function of the estimator as:

$$\mathbf{W}_{ll'} \equiv \mathrm{Tr}\left(\mathbf{P}^{l'}\mathbf{E}^l\right). \tag{3.21}$$

Now we find the estimate of C_l with minimal variance, subject to the normalization constraint that $\mathbf{W}_{ll} = 1$. Since we are assuming Gaussianity, the covariance matrix of equation 3.7 is given by

$$\mathbf{V}_{ll'} = \sum_{ijkl} [\mathbf{C}_{ik}\mathbf{C}_{jl} + \mathbf{C}_{il}\mathbf{C}_{jk}]\mathbf{E}^l_{ij}\mathbf{E}^{l'}_{kl}. \tag{3.22}$$

Since both $\mathbf{E}^l$ and $\mathbf{C}$ are symmetric, we can rewrite equation 3.22 as

$$\mathbf{V}_{ll'} = 2\mathrm{Tr}[\mathbf{C}\mathbf{E}^l\mathbf{C}\mathbf{E}^{l'}] \tag{3.23}$$

so we simply want to minimize $\mathrm{Tr}\left(\mathbf{C}\mathbf{E}^l\mathbf{C}\mathbf{E}^{l'}\right)$ subject to $\mathrm{Tr}\left(\mathbf{P}^l\mathbf{E}^l\right) = 1$. Introducing a Lagrange multiplier λ, we wish to minimize the function

$$L = \mathrm{Tr}[\mathbf{C}\mathbf{E}^l\mathbf{C}\mathbf{E}^l - 2\lambda(\mathbf{P}^l\mathbf{E}^l - 1)]. \tag{3.24}$$

Requiring the derivatives with respect to the components of $\mathbf{E}^l$ to vanish, we obtain

$$\mathbf{C}\mathbf{E}^l\mathbf{C} = \lambda\mathbf{P}^l, \tag{3.25}$$

so substituting the λ that gives $\mathrm{Tr}\left(\mathbf{P}^l\mathbf{E}^l\right) = 1$ leaves us with the solution

$$\mathbf{E}^l = \frac{1}{2\mathbf{F}_{ll}}\mathbf{C}^{-1}\mathbf{P}^l\mathbf{C}^{-1}, \tag{3.26}$$

where $\mathbf{F}$ is the Fisher information matrix given by Eq. 3.17, $\mathbf{F}_{ll} = \mathrm{Tr}[\mathbf{C}^{-1}\mathbf{P}^l\mathbf{C}^{-1}\mathbf{P}^l]/2$. We will now prove that this method is lossless, in the sense that no other (more nonlinear) method can do any better. We start by noting that the way we chose to normalize $\mathbf{E}^l$ does not affect the error bars with which we can determine cosmological parameters, since multiplying the estimated power spectrum coefficients $\hat{C}_l$ by some constants (or more generally by any invertible matrix) will not change their information content. To simplify the calculation below, we therefore define rescaled power spectrum coefficients

$$y_l \equiv \mathbf{x}^t\mathbf{E}^l\mathbf{x} \tag{3.27}$$

where

$$\mathbf{E}^l \equiv \frac{1}{2}\mathbf{C}^{-1}\mathbf{P}^l\mathbf{C}^{-1} \tag{3.28}$$

Substituting equation 3.28 into equation 3.23, we find that the covariance matrix for $\mathbf{y}$ reduces to

$$\left\langle \mathbf{y}\mathbf{y}^t \right\rangle - \left\langle \mathbf{y} \right\rangle \left\langle \mathbf{y} \right\rangle^t = \mathbf{F}, \tag{3.29}$$

the Fisher matrix. Arranging the true power spectrum coefficients C_l into a vector $\mathbf{c}$, equation 3.20 takes the form

$$\left\langle \mathbf{y} \right\rangle = \mathbf{F}\mathbf{c}, \tag{3.30}$$

expressing the fact that the window function matrix $\mathbf{W}$ is also equal to the Fisher matrix. This means that if we use the vector

$$\tilde{\mathbf{c}} \equiv \mathbf{F}^{-1}\mathbf{y} \tag{3.31}$$

to estimate the power spectrum $\mathbf{c}$, then this estimator will be unbiased:

$$\left\langle \tilde{\mathbf{c}} \right\rangle = \mathbf{c} \tag{3.32}$$

The Cramér-Rao inequality tells us that the best an unbiased estimator can do (in terms of giving small error bars) is for its covariance matrix to equal $\mathbf{F}^{-1}$, the inverse of the Fisher matrix. Using equation 3.29 and equation 3.31, we find that this covariance matrix is

$$\left\langle (\tilde{\mathbf{c}} - \mathbf{c})(\tilde{\mathbf{c}} - \mathbf{c})^t \right\rangle = \mathbf{F}^{-1}[\left\langle \mathbf{y}\mathbf{y}^t \right\rangle - \left\langle \mathbf{y} \right\rangle \left\langle \mathbf{y} \right\rangle^t]\mathbf{F}^{-1} = \mathbf{F}^{-1}, \tag{3.33}$$

so $\tilde{\mathbf{c}}$ is indeed optimal in this sense: it is the best unbiased estimator of the power spectrum, the one which gives the smallest error bars allowed by the Cramér-Rao inequality.

It is worth noting that given the vector of raw power spectrum estimates y_α, one can always take linear combination of them and trade off the correlation of the data points with the size of the error bars. Indeed, the author of Tegmark (1997) points out that the choice of computing $\mathbf{F}^{-1}$, despite giving uncorrelated parameter estimates, with all the window functions looking like Kronecker delta functions, would give a plot of the power spectrum with huge error bars, due to the incomplete sky coverage that makes the Fisher matrix nearly singular. Instead, the author proposes three particular choices for the linear combination of data to be taken, each producing characteristic features in the window functions. All of these choices are based on the factorisation of the Fisher matrix as

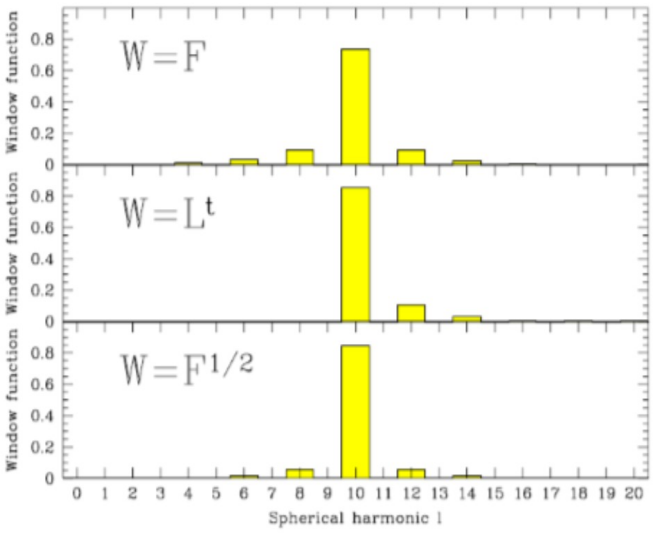

Figure 3.2: Window functions of the estimator at a fixed multipole $l^* = 10$, corresponding to three different linear combination of the raw data. This means three different choices for the matrix $\mathbf{M}$: using the original data vector $\mathbf{y}$, Choleski decomposing $\mathbf{F} = \mathbf{M}\mathbf{M}^t$ and taking $\mathbf{M}$ such that $\mathbf{M}^2 = \mathbf{F}$.

$$\mathbf{F} = \mathbf{M}\mathbf{M}^t \tag{3.34}$$

for some matrix $\mathbf{M}$, and then the linear combination considered is $\mathbf{X}^t\mathbf{y}$ with $\mathbf{X} = \mathbf{M}^{-1}$. The three particularly interesting choices for $\mathbf{M}$ are:

1. A lower triangular $\mathbf{M}$, such that $\mathbf{F} = \mathbf{M}\mathbf{M}^t$ corresponds to a Choleski decomposition. This case produces narrow and non-negative window functions (which is not guaranteed *a priori*) with side lobes only to the right;

2. Contrastingly, an upper triangular $\mathbf{M}$ produces side lobes only to the left;

3. Finally, the choice of $\mathbf{M}$ symmetric, such that $\mathbf{M^2} = \mathbf{F}$, produces non-negative and narrow window functions.

In Fig. 3.2 we can see the features of the window functions corresponding to these different choices. These linear combinations of the data produce some quantities that characterise the data in a highly compressed form, but are not estimates of the power spectrum in themselves, not being unbiased

estimators of the power spectrum. However, they are linear functions of $\mathbf{c}$, therefore the cosmological content is unchanged. We would also like to point out that, in a simulation with known power spectrum, one can always visually compare these quantities and the true power spectrum, by multiplying the latter on the left by $\mathbf{X}^t\mathbf{F}$.

3.2 The galaxies case

In 2004 the Sloan Digital Sky Survey collaboration released a paper [Tegmark et al. (2004)] where they provided a measurement of the matter power spectrum $P(k)$ on large scales by using data of over 200000 galaxies coming from the Survey. The matrix-based method followed in the paper differs substantially from others already present in literature and based on traditional Fourier methods [Percival et al. (2001); Feldman et al. (1993)] that have several drawbacks: since galaxies in a redshift survey probe the underlying density field only in a finite volume, the power spectrum estimated with Fourier methods only corresponds to a smeared out version of the true power spectrum, can underestimate power on the largest scales because of the integral constraint [Peacock and Nicholson (1991)] and has correlated errors. Contrastingly, if the galaxies were faithful tracers of mass, the proposed matrix-based method would produce unbiased minimum-variance power spectrum measurements with uncorrelated error bars, smaller than those from the Fourier methods.
The power spectrum estimation approach starts by expanding the galaxy density field in a set of functions known as pseudoKarhunen-Loève eigenmodes [Tegmark et al. (2002)]. This step compresses the data set into a much smaller size while retaining the large-scale cosmological information of interest. It also reduces the power spectrum estimation problem to a mathematical form equivalent to that encountered in CMB analysis, making the analysis similar to the case described in the previous section. Since the mathematical details of the quadratic estimator have already been described in the CMB section, here we will only briefly recall the key definitions and change the notation to make it more suitable for the case of the galaxies power spectrum; subsequently we will present the results, especially in terms of window functions of the estimator, deriving from the different choices of the linear combinations of data.

3.2.1 The method

The raw data consist of three-dimensional vectors $\mathbf{r}_\alpha$, giving the measured positions of each galaxy in redshift space. The observed three-dimensional density field is expanded in a basis of N_x noise-orthonormal functions $\psi_i, i = 1, ..., N_x$,

$$x_i \equiv \int \frac{n(\mathbf{r})}{\bar{n}(\mathbf{r})}\psi_i(\mathbf{r})\mathrm{d}^3r \tag{3.35}$$

and then we consider the N_x-dimensional data vector $\mathbf{x}$ of expansion coefficients instead of the $3 \times N_{gal}$ numbers $\mathbf{r}_\alpha$. Quadratic estimators $\hat{p}_i$ are quadratic functions of the data vector $\mathbf{x}$,

$$\hat{p}_i \equiv \mathbf{x^t Q_i x} - \mathrm{Tr}(\mathbf{N Q_i}) \tag{3.36}$$

where we already set the de-bias term equal to $\mathrm{Tr}\,(\mathbf{NQ}_i)$ to make the estimate unbiased. The basic idea behind quadratic estimators is that each matrix $\mathbf{Q_i}$ can be chosen to effectively Fourier transform the density field, square the Fourier modes in the i-th power spectrum band, and average the results together, thereby probing the power spectrum on that scale. Grouping the parameters p_i and the estimators $\hat{p}_i$ into vectors denoted $\mathbf{p}$ and $\hat{\mathbf{p}}$, the expectation value and covariance of the measurements is given by

$$\langle \hat{p} \rangle = \mathbf{W p} \tag{3.37}$$

$$cov(\hat{p}) \equiv \left\langle \hat{\mathbf{p}}\hat{\mathbf{p}}^\mathbf{t} \right\rangle - \langle \hat{\mathbf{p}} \rangle \left\langle \hat{\mathbf{p}}^\mathbf{t} \right\rangle = \mathbf{\Sigma} \tag{3.38}$$

where an explicit expression of $\mathbf{W}$ and $\mathbf{\Sigma}$ is provided below.
Following the CMB case, we choose the $\mathbf{Q}$ matrices to be of the form

$$\mathbf{Q}_i = \frac{1}{2}\sum_{j=1}^{m} \mathbf{M}_{ij}\mathbf{C}^{-1}\frac{\partial \mathbf{C}}{\partial p_i}\mathbf{C}^{-1} \tag{3.39}$$

where $\mathbf{F}$ is the Fisher matrix, given by

$$\mathbf{F}_{ij} = \frac{1}{2}\mathrm{Tr}\left[\mathbf{C}^{-1}\,\frac{\partial \mathbf{C}}{\partial p_i}\,\mathbf{C}^{-1}\,\frac{\partial \mathbf{C}}{\partial p_j}\right]. \tag{3.40}$$

This gives for the window matrix and the covariance matrix

$$\mathbf{W} = \mathbf{MF} \tag{3.41}$$

$$\mathbf{\Sigma} = \mathbf{MFM}^t \tag{3.42}$$

The choice of $\mathbf{M}$ is crucial. Ideally one would like to have both uncorrelated error bars (diagonal $\mathbf{\Sigma}$) and well-behaved (narrow, unimodal, and nonnegative) window functions $\mathbf{W}$. In fact, if the window functions have a nonzero width Δk, the estimate of the power on some scale k is really the weighted

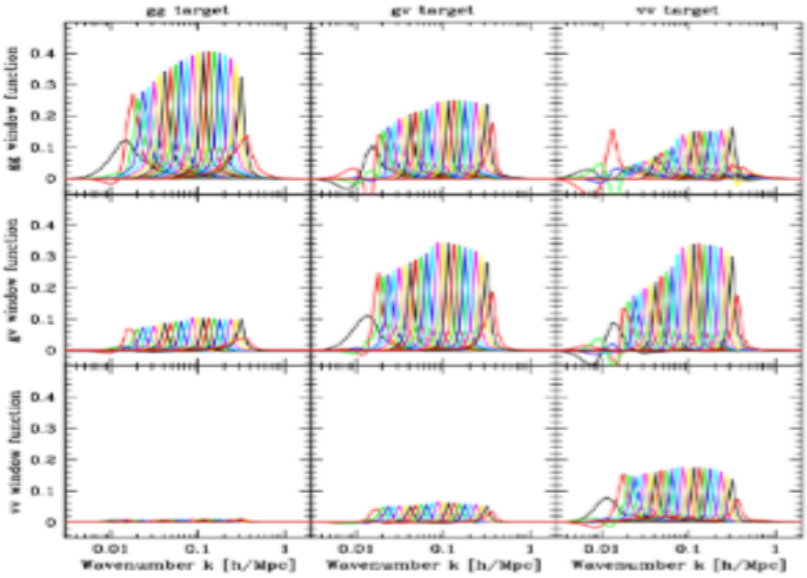

Figure 3.3: Window functions of the estimator in Tegmark et al. (2004), corresponding to the choice $\mathbf{M} = \mathbf{F}^{-1/2}$.

average of the power over a range of scales around k. For all choices of $\mathbf{M}$, we wish each window function (row of $\mathbf{W}$) to sum to unity so that we can interpret $\hat{p}_i$ as measuring a weighted average of the true power. Because of equation 3.41, the rows of $\mathbf{M}$ are therefore normalized to satisfy

$$\sum_j (\mathbf{MF})_{ij} = 1 \tag{3.43}$$

An interesting choice is $\mathbf{M} = \mathbf{F}^{-1}$, which gives $\mathbf{W} = \mathbf{I}$. In other words, all window functions are Kronecker delta functions, and $\hat{\mathbf{p}}_i$ gives completely unbiased estimates of the band powers, with $\langle \hat{p}_i \rangle = p_i$ regardless of what values the other band powers take. This gives an estimate $\hat{\mathbf{p}}$ similar to the maximum likelihood method, and the covariance matrix reduces to $\mathbf{F}^{-1}$. A serious drawback of this choice is that this covariance matrix tends to give large error bars ($\Delta p_i \equiv \mathbf{M}_{ii}^{1/2} = [(\mathbf{F}^{-1})_{ii}]^{1/2}$).
The choice $\mathbf{M} = \mathbf{F}^{-1/2}$ with the rows renormalized has the attractive property of making the errors uncorrelated, with the covariance matrix diagonal. The corresponding window functions $\mathbf{W}$ are plotted in Fig 3.3 and are seen to be quite well behaved: this choice turns out to be very effective, as it narrows the minimum-variance window functions at the cost of only a small noise increase, with uncorrelated noise as an extra bonus.

Chapter 4

The weak lensing case

We now move to the development of a quadratic estimator for the matter power spectrum $P(k)$ from weak lensing measurements, giving a detailed mathematical description of how the power spectrum is recovered from the measurements through the estimator. In the following we will concentrate on estimates of $P(k)$ from the convergence k, firstly introducing the mathematical basis of the estimator and then moving, in chapter 5, to the description of the unidimensional implementation of the method. In chapter 6 we finally move to the two- and three-dimensional case. Here we will present two different derivations of the method, valid in two different regimes: infinite and finite signal-to-noise (S/N) ratio.

4.1 Mathematical foundations

The quantity that has been used as a starting point, from which we extract information regarding the power spectrum, is the convergence κ, introduced in Chapter 1. The reason for this choice is that, being k a scalar field, it is easier to handle than a spin-2 field as the shear γ. The calculations for the shear are presented in the concluding chapter.

4.1.1 Tomography of the convergence field

We know from the theory of lensing (see chapter 1) that the convergence is related to the over density $\delta \equiv \frac{\rho-\bar{\rho}}{\bar{\rho}}$ by a line-of-sight integral

$$\kappa(z,\theta,\phi) = \int_0^z \mathrm{d}z' K(z,z')\delta(z',\theta,\phi) \tag{4.1}$$

where z is the redshift, θ and ϕ are the angular coordinates in a spherical coordinate system and $K(z,z')$ is a broad kernel function of lensing, given by Eq. 1.97:

$$\kappa_{eff} = \frac{3\Omega_m}{2}\left(\frac{H_0}{c}\right)^2 \int_0^w dw' \frac{f_K(w')f_K(w-w')}{f_K(w)} \frac{\delta[f_K(w')\vec{\theta}', w']}{a(w')}. \quad (4.2)$$

Using the notation of chapter 1, in the flat-Universe approximation $f(w) = w$ and therefore we can rewrite Eq. 4.1, specifying the kernel function, as

$$\kappa(\vec{r}) = \frac{3H_0^2\Omega_m}{2c^2} \int_0^r \mathrm{d}r' \frac{r'(r-r')}{r} \frac{\delta(\vec{r'})}{a(r')} \quad (4.3)$$

A basic issue we need to deal with is that the power spectrum evolves, so the first approximation that we make is to ignore it, by assuming that P does not evolve. We follow a tomographical approach, discretizing the problem into a series of shells labelled by Roman indices i:

$$\kappa_i = K_{ij}\delta_j + \epsilon_i \quad (4.4)$$

where the summation convention on the indices is implied. ϵ_i represents noise coming for example from shape/size dispersion and shot noise, or measurement errors. We will have $\langle\epsilon\rangle_i = 0$ and $\langle\epsilon_i\epsilon_j\rangle = N_{ij}$. We will consider $N_{ij} = \sigma_i^2\delta_{ij}^K$, where δ_{ij}^K is the Kronecker delta.

4.1.2 Assumptions

The mathematical derivation of the method is based on some underlying assumptions, which we now summarise here for clarity. We will then come back on them in chapter 7, commenting extensively on their validity and their possible developments in future work on the estimator.

1. $P(k, z) = P(k)$, i.e. we ignore the evolution of the matter power spectrum. This is a major simplification and may sound as a significant limitation for the validity of the method. Nevertheless, it is clear that even our simplified stationary treatment does not guarantee the success of the quadratic estimator in recovering the power spectrum. Therefore, dealing with a non-evolving $P(k)$ still represents a crucial initial step in the development of a complete estimator. Since it is not clear *a priori* that the method will work even in this simplified case, the fact that we prove in the next chapters that it does succeed constitutes a first necessary goal to be achieved in the development of a complete estimator. In other words if, for whatever reasons, the method did not prove to be successful even in this simplified case, there would be no hope in trying to extend it to a more complicated, redshift-dependent version.

2. $\sigma \neq \sigma(z)$, i.e., analogously to what we have done for the power spectrum, we consider a simplified noise, independent of the redshift z.

3. *Gaussian fields*: for both the overdensity and noise fields, we assume them to be Gaussian fields. This allows us to use Wick's theorem for them in our calculations (see Sect. 4.2.2).

4. *"Distant observer" approximation*: if the survey volume considered is far enough from the observer, then the lines of sight can be considered parallel and we can adopt a Fourier expansion (instead of a decomposition in spherical harmonics), including the use of FFT and IFFT algorithms when needed.

4.1.3 The starting point

Similarly to both the CMB and galaxies case, we start by seeking a quadratic estimator for the 3D power spectrum $P(k)$, at wavenumber k_α (labelled by the integer α), of the form:

$$\hat{P}_\alpha = \kappa_i E^\alpha_{ij} \kappa_j - B_\alpha \tag{4.5}$$

where the weights E^α and the de-bias term B_α are to be found. We can rewrite the previous expression in terms of the overdensities:

$$P^\alpha = K_{il} E_{ij} K_{jm} \delta_l \delta_m \tag{4.6}$$

or, in matrix notation

$$\mathbf{P} = \delta^T \mathbf{G} \delta, \tag{4.7}$$

where

$$\mathbf{G} = \mathbf{K}^T \mathbf{E} \mathbf{K} \tag{4.8}$$

The expectation value of P^α involves

$$\langle \delta_l \delta_m \rangle = \xi_{lm} = \int \frac{\mathrm{d}^3 k}{(2\pi)^3} P(k) \exp^{-\mathrm{i}\vec{k}\cdot(\vec{r}_l - \vec{r}_m)} \equiv A^\alpha_{lm} P_\alpha \tag{4.9}$$

The matrices (for fixed α) A are defined by the discretised version of this equation. We will come back on the exact definition of these matrices in Chapters 4 and 5, where we will give an explicit expression for them in the

1D, 2D and 3D case. ξ is the matrix that stores the correlation function, so that ξ_{lm} contains the information regarding the correlation between the data point labelled by index l and the data point labelled by index m. Again, we will provide a more detailed insight into this matrix in the chapters dedicated to the description of the method for the 1D, 2D and 3D case. For the moment, we emphasize that ξ_{lm} relates the data point l and m, therefore Eq. 4.9 is valid in any dimension, with the condition that the data set must be stored in a single one-dimensional array, over which the indices l and m can run.
That said, we have

$$\hat{\mathbf{P}} = \mathbf{WP} \tag{4.10}$$

where

$$W_{\alpha\beta} = \mathrm{Tr}(KA^{\beta T}K^T A^{\alpha}) \tag{4.11}$$

and we choose

$$B_\alpha = N_{ij}E^{\alpha}_{ij} = \sum_i \sigma_i^2 E^{\alpha}_{ii} \tag{4.12}$$

so as to make $\hat{P}$ unbiased.

4.2 Different noise regimes

4.2.1 The infinite S/N case

In the high (theoretically infinite) S/N limit the covariance of $\hat{P}$ is:

$$V_{\alpha\beta} = \left\langle (\hat{P}_\alpha - P_\alpha)(\hat{P}_\beta - P_\beta) \right\rangle = 2Tr(\xi \mathbf{K}^T \mathbf{E}^{\alpha} \mathbf{K} \xi \mathbf{K} \mathbf{E}^{\beta} \mathbf{K}^T) \tag{4.13}$$

which, following Tegmark's approach in Tegmark (1997), we minimise subject to the constraint $W_{\alpha\alpha} = 1$. Assuming high S/N, we obtain the weights (which will not be optimal in the finite S/N regime), still leading to unbiased $\hat{P}_\alpha$, provided we use the bias correction B_α with the weights $\mathbf{E}^{\alpha}$ we deduce. Since we can rewrite expression 4.13 as

$$V_{\alpha\beta} = 2\mathrm{Tr}(\xi \mathbf{G}_\alpha \xi \mathbf{G}^T_\beta) \tag{4.14}$$

we get an expression that is formally similar to the one in Tegmark's paper, the only big exception being that the $\mathbf{E}$ matrices in Tegmark's version are

now replaced by the **G** matrices, which in turn contain the **E** matrices. Therefore, following the same procedure as Tegmark's paper, we find that the solution (for **G**, in this case), is given by

$$\mathbf{G}_\alpha = \mathbf{K}^T \mathbf{E}^\alpha \mathbf{K} = \frac{\xi^{-1} \mathbf{A}_\alpha \xi^{-1}}{2F_{\alpha\alpha}} \tag{4.15}$$

where

$$F_{\alpha\beta} = \frac{1}{2} \mathrm{Tr}(\xi^{-1} \mathbf{A}_\alpha^T \xi^{-1} \mathbf{A}_\beta) \tag{4.16}$$

is the Fisher matrix in our case of interest. Now we can see the main difference between the weak lensing and both the CMB and galaxies cases: as we want to find an explicit expression for the weights **E**, we need to invert Eq. 4.15. It turns out that this can be done, as **K** is a triangular matrix with no diagonal elements equal to 0, which makes it invertible (see chapter 5 for a detailed description of the **K** matrix). Then we can simply recover **E** from **G** as

$$\mathbf{E}^\alpha = \frac{(\mathbf{K}^T)^{-1} \xi^{-1} \mathbf{A}_\alpha^T \xi^{-1} \mathbf{K}^{-1}}{2F_{\alpha\alpha}} \tag{4.17}$$

4.2.2 The finite S/N case

We would like to include the noise in the covariance. We calculate the covariance as

$$V_{\alpha\beta} = \langle \hat{P}_\alpha \hat{P}_\beta \rangle - \langle \hat{P}_\alpha \rangle \langle \hat{P}_\beta \rangle \tag{4.18}$$

where

$$\hat{P}_\alpha = \kappa_i E^\alpha_{ij} \kappa_j - B_\alpha. \tag{4.19}$$

We have

$$\hat{P}_\alpha - P_\alpha = K_{il} E^\alpha_{ij} K_{jm} \delta_l \delta_m + 2\epsilon_i \delta_m E^\alpha_{ij} K_{jm} + \epsilon_i \epsilon_j E^\alpha_{ij} - N_{ij} E^\alpha_{ij} K_{il} E^\alpha_{ij} K_{jm} \xi_{lm} \tag{4.20}$$

then

$$V_{\alpha\beta} = \langle \big(K_{il} E^\alpha_{ij} K_{jm} \delta_l \delta_m + 2\epsilon_i \delta_m E^\alpha_{ij} K_{jm} + \epsilon_i \epsilon_j E^\alpha_{ij} - N_{ij} E^\alpha_{ij} K_{il} E^\alpha_{ij} K_{jm} \xi_{lm} \big) \tag{4.21}$$

$$\Big(K_{i'l'} E^\beta_{i'j'} K_{j'm'} \delta'_l \delta'_m + 2\epsilon'_i \delta'_m E^\beta_{i'j'} K_{j'm'} + \epsilon'_i \epsilon'_j E^\beta_{i'j'} - N_{i'j'} E^\beta_{i'j'} K_{i'l'} E^\beta_{i'j'} K_{j'm'} \xi_{l'm'} \Big) \rangle. \tag{4.22}$$

We assume both δ and ϵ are Gaussian fields, so we can use Wick's theorem for them:

$$\langle \delta_i \delta_j \delta_k \delta_l \rangle = \langle \delta_i \delta_j \rangle \langle \delta_k \delta_l \rangle + \langle \delta_i \delta_k \rangle \langle \delta_j \delta_l \rangle + \langle \delta_i \delta_l \rangle \langle \delta_k \delta_j \rangle \tag{4.23}$$

The two-point functions are ξ_{ij} and N_{ij}, therefore V reduces to:

$$V_{\alpha\beta} = K_{il} E^{\alpha}_{ij} K_{jm} K_{i'l'} E^{\beta}_{i'j'} K_{j'm'} (\xi_{ll'} \xi_{mm'} + \xi_{lm'} \xi_{ml'}) \tag{4.24}$$

$$+4 N_{ip} \xi_{mq} E^{\alpha}_{ij} K_{jm} E^{\beta}_{ps} K_{sq} + E^{\alpha}_{ij} E^{\beta}_{pq} (N_{ip} N_{jq} + N_{iq} N_{jp}). \tag{4.25}$$

Minimising $V_{\alpha\alpha}$ with respect to E_{uv} subject to $W_{\alpha\alpha} = 1$ gives

$$K_{ul} K_{vm} K_{i'l'} E^{\alpha}_{i'j'} K_{j'm'} (\xi_{ll'} \xi_{mm'} + \xi_{lm'} \xi_{ml'}) + K_{il} K_{jm} E^{\alpha}_{ij} K_{ul'} K_{vm'} (\xi_{ll'} \xi_{mm'} + \xi_{lm'} \xi_{ml'}) \tag{4.26}$$

$$+ 4 N_{up} \xi_{mq} K_{vm} E^{\alpha}_{ps} K_{sq} + 4 N_{iv} \xi_{mq} E^{\alpha}_{ij} K_{jm} K_{vq} + E^{\alpha}_{pq} (N_{up} N_{vq} + N_{uq} N_{vp}) \tag{4.27}$$

$$+ E^{\alpha}_{ij} (N_{iu} N_{jv} + N_{iv} N_{ju}) - \lambda K_{ul} K_{vm} A^{\alpha}_{lm} = 0 \tag{4.28}$$

where λ is a Lagrange multiplier. Rearranging and letting $\mu = \lambda/4$, we have

$$\mu \operatorname{Tr}\left[\mathbf{K}^T \mathbf{A}^{\alpha} \mathbf{K}\right] = \operatorname{Tr}\left[\mathbf{K} \xi \mathbf{K}^T \mathbf{E}^{\alpha} \mathbf{K} \xi \mathbf{K}^T + 2 \mathbf{N} \mathbf{E}^{\alpha} \mathbf{K} \xi \mathbf{K}^T + \mathbf{N} \xi^{\alpha} \mathbf{N}\right] \tag{4.29}$$

which we can rewrite as

$$\mu \operatorname{Tr}\left[\mathbf{K}^T \mathbf{A}^{\alpha} \mathbf{K}\right] = \operatorname{Tr}\left[\mathbf{M} \mathbf{E}^{\alpha} \mathbf{M} + 2 \mathbf{N} \mathbf{E}^{\alpha} \mathbf{M} + \mathbf{N} \mathbf{E}^{\alpha} \mathbf{N}\right] \tag{4.30}$$

where $\mathbf{M} = \mathbf{K} \xi \mathbf{K}^T$.
Thus we solve with

$$E_{\alpha} = \mu (\mathbf{M} + \mathbf{N})^{-1} \mathbf{K} \mathbf{A}^{\alpha} \mathbf{K}^T (\mathbf{M} + \mathbf{N})^{-1}. \tag{4.31}$$

The condition $W_{\alpha\alpha} = 1$ implies $\mathbf{K}^T \mathbf{E}^{\alpha} \mathbf{K} \mathbf{A}^{\alpha} = 1$, so

$$\mathbf{E}^{\alpha} = \frac{(\mathbf{M} + \mathbf{N})^{-1} \mathbf{K} \mathbf{A}^{\alpha} \mathbf{K}^T (\mathbf{M} + \mathbf{N})^{-1}}{\operatorname{Tr}[\mathbf{K}^T (\mathbf{M} + \mathbf{N})^{-1} \mathbf{K} \mathbf{A}^{\alpha} \mathbf{K}^T (\mathbf{M} + \mathbf{N})^{-1} \mathbf{K} \mathbf{A}^{\alpha}]} \tag{4.32}$$

and we can see that we recover the infinite S/N result if $\mathbf{N} = 0$.

Chapter 5

Testing the estimator in one dimension

In this chapter we start describing the analysis carried out on the estimator to prove the goodness of the method previously derived. To this purpose, we test the estimator by creating a density field from a given power spectrum $P(k)$, whose analytic form is known exactly. We then pass from the density field $\delta(\vec{x})$ to the convergence field $\kappa(\vec{x})$ and we let the estimator act on that, so as to recover the original power spectrum. The estimate of the power spectrum obtained from the matrix-based method described in the previous chapter is then compared with the original, analytic power spectrum through a chi-square analysis. Simultaneously we study the window functions of the estimator and experiment different linear combinations of the data: following what described in Sect. 3.2.1, we trade off the covariance of the data with the size of the errorbars.

This testing of the estimator is performed through different levels of complexity. In particular, this involves starting from a 1D configuration, moving to a 2D approach and finally reaching a 3D analysis of the estimator. In doing so, not only we experiment different linear combinations of the raw data which give small error bars and/or uncorrelated values of the power spectrum at the different scales, but we also pass from a simplified treatment, with infinite signal-to-noise ratio, to a more realistic approach in the finite signal-to-noise regime.

In this chapter we present a detailed implementation of the model in the 1D case, providing a step-by-step description of the procedure followed to test the estimator. We then present the results obtained and comment on them. In chapter 6 we move to the description of the two- and three-dimensional case, putting emphasis on the differences between those cases and the one-dimensional case. In fact, while some of the steps followed in the procedure are similar for all dimensions, some of them differ in a significant way. As we will describe in detail later on, this particularly applies to the creation of

the initial density field and to the storage of the data, based on a mapping from multidimensional to one-dimensional arrays.
Furthermore, in the 1D case we will work under the assumption of infinite S/N ratio: the optimised weights including the effect of noise will be implemented in the 2D and 3D case.
Let us start now by describing the procedure followed to simulate a weak lensing dataset, which our estimator will use to recover the input power spectrum.

5.1 The mock dataset

Our purpose is to create a convergence field $\kappa(\vec{x})$ on a grid, whose elements are labelled by index i. In the one-dimensional case this would represent a line of sight, extending from the observer to the observed region in the sky, as shown in Fig. 5.1. The one-dimensional case corresponds to concentrating only on one particular line of sight, ignoring the others: with this approach, we effectively reduce our analysis to a fully one-dimensional treatment.

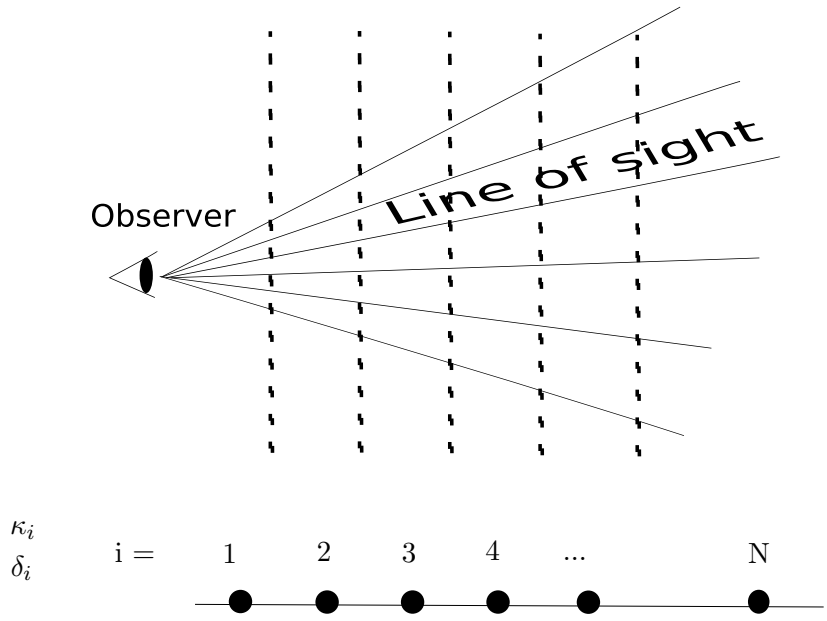

Figure 5.1: Sketch of the tomographic approach followed to model our mock dataset. In the 1D case we concentrate on just one line-of-sight and ignore the others. The result is the graphic shown in the lower part of the figure. We thus have one value of the fields $\kappa(\vec{x})$ and $\delta(\vec{x})$, both labelled by the index i, for each pixel of the grid. Index i ranges from 1 to N, where N indicates the number of pixels.

5.1.1 Choice of the input power spectrum

The first step consists in choosing an analytic form for our input power spectrum $P(k)$, which the estimator aims at recovering. The power spectrum we choose for the generation of the field is a Gaussian,

$$P(k) = P_0\, e^{-\frac{k^2\sigma^2}{2}} \tag{5.1}$$

P_0 being a constant, its value always set to 50 in the following. This is a simple analytic form that produces a likewise simple correlation function (another Gaussian, see sect.5.2.1). Furthermore, in order to make sure that the $\delta(\vec{x})$ field has mean 0, we need to impose $P(k) = 0$. We also need to take into account the grid step, which enters directly the expression provided for the power spectrum. If we call L and N the length and number of pixels of the grid respectively, we can write

$$k = \tilde{k}\frac{2\pi}{L}, \quad \sigma = \tilde{\sigma}\frac{L}{N}, \tag{5.2}$$

defining the physical wavenumbers k and the width σ of the power spectrum in units of the grid step. Eq. 5.1 for the power spectrum then becomes

$$P(k) = P_0\, e^{-\frac{(\tilde{k}\frac{2\pi}{L}\tilde{\sigma}\frac{L}{N})^2}{2}} = P_0\, e^{-\frac{(\frac{2\pi}{N}\tilde{k}\tilde{\sigma})^2}{2}}. \tag{5.3}$$

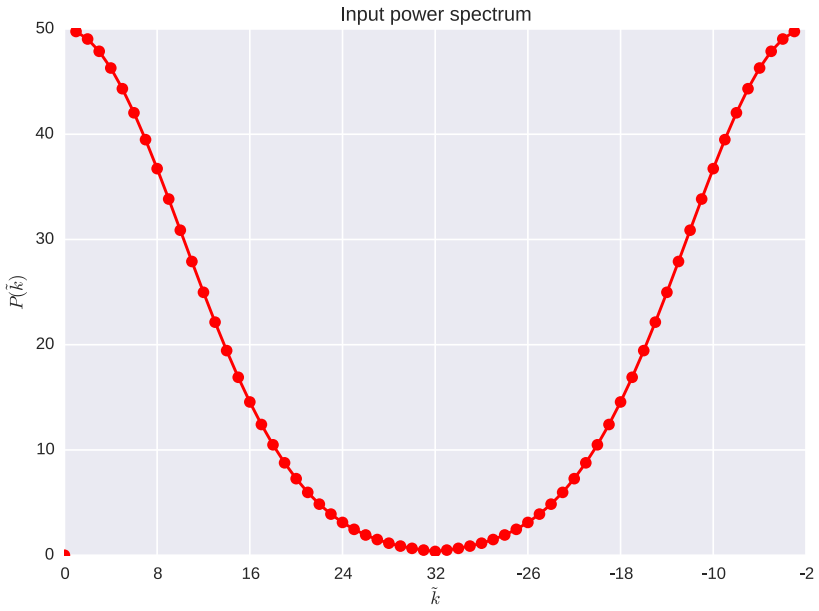

Figure 5.2: Gaussian power spectrum chosen for the generation of the density field. In this case $\tilde{\sigma} = 1.0$ and $L = N = 64$. The symmetry of the power spectrum with respect to the Nyquist frequency is due to the presence of the negative frequencies on the right-hand side of the $\tilde{k}$ axis.

In Fig. 5.2 we report an example of this power spectrum, for values of $\tilde{\sigma} = 1.0$ and $L = N = 64$. We can appreciate the symmetry of the power spectrum with respect to the Nyquist frequency $k_{nyq} = N/2$, due to the fact that the Gaussian is symmetric for positive and negative values of k.

5.1.2 Generating a density field from given power spectrum

Despite the fact that the results presented in this subsection are relative to the one-dimensional case, the procedure to generate a density field from a given power spectrum $P(k)$ is conceptually the same for every dimension. Therefore in the following we will indicate with n the generic dimension, using then the 1D case to give a concrete example of the algorithm described.

The procedure to generate a density field from a given $P(k)$ is easier to carry out in Fourier space, if we consider our density field $\delta(\vec{x})$ to be a statistically homogeneous and isotropic Gaussian random field. With this assumption, the Fourier coefficients,

$$\delta(\vec{k}) = \int \mathrm{d}^n x \, e^{\mathrm{i}\vec{k}\cdot\vec{x}} \, \delta(\vec{x}) \tag{5.4}$$

are only correlated as pairs

$$\left\langle \delta(\vec{k})\delta(-\vec{k'}) \right\rangle = \delta(\vec{k} - \vec{k'})P(k). \tag{5.5}$$

All higher-order moments can be traced back to second-order correlations. In addition, the Fourier coefficients, real and imaginary part separately, are Gaussian random variables because they are linear combinations of the field variables $\delta(\vec{x})$, as we can see from Eq. 5.4. This simplicity makes the realisation of a Gaussian random field easier if done for the coefficients $\delta(\vec{k})$. We only have to take care of the fact that the real and imaginary parts of just two Fourier coefficients are statistically correlated to each other. It follows for $\vec{k} \neq 0$ from Eq. 5.5 that $\left\langle \delta(\vec{k})\delta(\vec{k}) \right\rangle = 0$, or, if we split the equation into real and imaginary part,

$$\left\langle [\mathrm{Re}\,\delta(\vec{k})]^2 \right\rangle = \left\langle [\mathrm{Im}\,\delta(\vec{k})]^2 \right\rangle \tag{5.6}$$

$$\left\langle \mathrm{Re}\,\delta(\vec{k})\mathrm{Im}\,\delta(\vec{k}) \right\rangle = 0 \tag{5.7}$$

This means that in a homogeneous random field, real and imaginary part of $\delta(\vec{k})$ are not correlated and both, individually, must have the same variance. Furthermore, we can deduce that for $\vec{k} \neq 0$:

$$\left\langle \delta(\vec{k})\delta(-\vec{k}) \right\rangle = P(k) \tag{5.8}$$

from which it follows that

$$\left\langle \mathrm{Re}\,\delta(\vec{k})\mathrm{Re}\,\delta(-\vec{k})\right\rangle = -\left\langle \mathrm{Im}\,\delta(\vec{k})\mathrm{Im}\,\delta(-\vec{k})\right\rangle = \frac{\mathrm{Re}\,P(k)}{2} \tag{5.9}$$

$$\left\langle \mathrm{Re}\,\delta(\vec{k})\mathrm{Im}\,\delta(-\vec{k})\right\rangle = +\left\langle \mathrm{Im}\,\delta(\vec{k})\mathrm{Re}\,\delta(-\vec{k})\right\rangle = \frac{\mathrm{Im}\,P(k)}{2}. \tag{5.10}$$

This confines the correlations between all combinations of real and imaginary parts of the coefficient pair $\delta(\vec{k})$ and $\delta(-\vec{k})$. As we consider only cases in which the power spectrum is purely real, $\mathrm{Re}\,P(k) = P(k)$ and $\mathrm{Im}\,P(k) = 0$, the imaginary and real parts of $\delta(\vec{k})$ and $\delta(-\vec{k})$ in Eq. 5.10 are not correlated. We consider a more specialised case by restricting ourselves to real Gaussian fields with $\delta^*(\vec{x}) = \delta(\vec{x})$. This introduces an additional condition that follows from the definition 5.4 of the $\delta(\vec{k})$:

$$\delta(\vec{k}) = \delta^*(-\vec{k}) \iff \begin{cases} \mathrm{Re}\,\delta(\vec{k}) & = +\mathrm{Re}\,\delta(-\vec{k}) \\ \mathrm{Im}\,\delta(\vec{k}) & = -\mathrm{Im}\,\delta(-\vec{k}) \end{cases} \tag{5.11}$$

This further simplifies the task of making a field realisation. We only need a random number generator that makes a realisation of one single number based on a Gaussian PDF. The conditions 5.11 are easily accounted for if, for example, only the $\delta(\vec{k})$ for half of the spatial frequencies $\vec{k}$ are worked out and the frequencies are set accordingly. Furthermore, the real and imaginary parts of $\delta(\vec{k})$ are uncorrelated, and both follow the same Gaussian PDF. This PDF has zero mean and a variance

$$\sigma_k^2 = \frac{P(k)}{2} \tag{5.12}$$

according to Eq. 5.9.
The procedure for making one Gaussian field realisation thus requires two steps:

1. drawing numbers for the real and imaginary parts for every independent $\delta(\vec{k})$ with a Gaussian random number generator,

2. transforming this Fourier space representation to real space in order to obtain the field realisation. For this second step we used an IFFT algorithm.

In Fig. 5.4 we show an example of the passage from step 1 to step 2, namely from the k-space coefficients $\delta(\vec{k})$, generated from our Gaussian power spectrum, to the density field $\delta(\vec{x})$. Having paid attention to respect the conditions given by Eq. 5.11, we find an imaginary part of the field in configuration space which is basically 0 to within numerical precision, therefore we will ignore it in the following. Since the amplitudes of the

density and, consequently, of the convergence field (which depends on the density, see Sect. 5.1.3), are not particularly interesting for our study, we do not attempt to normalise them to realistic values.

Figure 5.3: Real and imaginary part of the field in k-space

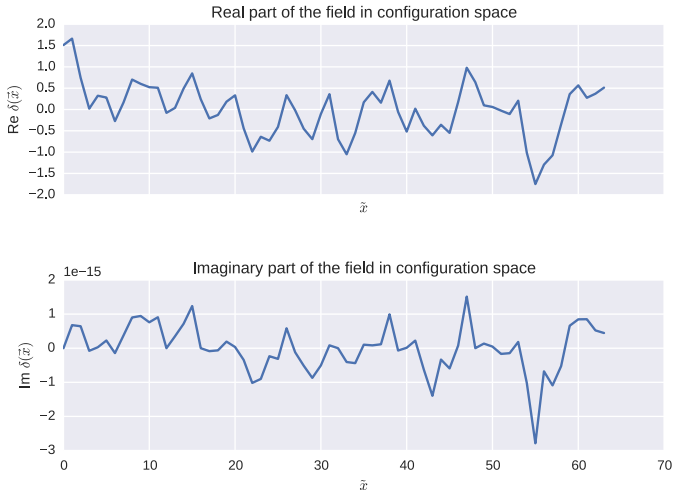

Figure 5.4: Real and imaginary part of the field in configuration space. Since, by construction, the imaginary part is negligible, we will ignore it from now on.

5.1.3 From the density field to the convergence field

Once we have generated the density field $\delta(\vec{x})$ we need to relate it to the convergence field $\kappa(\vec{x})$, as it constitutes the actual mock dataset upon which our estimator acts to recover the power spectrum. To pass from the density to the convergence field we exploit Eq. 3.43,

$$\kappa(z,\theta,\phi) = \int_0^z \mathrm{d}z' K(z,z')\delta(z',\theta,\phi) \tag{5.13}$$

In this formula K is the weak lensing kernel function. In the flat-Universe approximation we can specify last expression, which becomes

$$\kappa(r) = \frac{3H_0^2\Omega_m}{2c^2}\int_0^r \mathrm{d}r' \frac{r'(r-r')}{r}\frac{\delta(\vec{r'})}{a(r')} \tag{5.14}$$

so that we can identify the kernel function K as a function of the distances r and r'

$$K(r,r') = \frac{3H_0^2\Omega_m}{2c^2}\frac{r'(r-r')}{r}. \tag{5.15}$$

Eq. 5.14 contains the scale factor, which we can rewrite as a function of the distance, assuming $z \ll 1$, as

$$\frac{1}{a(r)} = 1 + z(r) \approx 1 + \frac{H_0}{c}r \tag{5.16}$$

Now, following the tomographic approach described in sect. 4.1, we need to discretize this expression, namely we need to find the matrices K_{ij} such that

$$\kappa_i = K_{ij}\delta_j \tag{5.17}$$

This is easily done assigning the index i to the coordinate r and the index j to the coordinate r'. In the one-dimensional case that we are considering here, this simply means that given our 1D array of κ_i, we assign a distance i to the i-th element and j to the j-th element. As we will see in the next chapter, in the 2D and 3D case this approach is still valid only if we store the multidimensional convergence field in a 1D array and pay attention to establish a suitable mapping between the two arrays. An assumption that we make is that, given a position i in the grid, the convergence κ in i depends on the matter distribution *until* the i-th pixel, but is independent of the density

field *beyond* i. This makes the $\mathbf{K}$ matrix triangular, as the summation over j in Eq.5.17 goes from 0 to i.
The prefactor in Eq. 5.15, containing constants, can be set to 1, as in the rest of the following treatment this numerical coefficient would get simplified in any case. This allows us to avoid extremely small numbers, numerically difficult to handle.
Nevertheless, a difficulty that we might encounter in building the $\mathbf{K}$ matrix arises from the singularity of the matrix itself. This is a problem, as in the algorithm for the recovery of the power spectrum we need to invert the $\mathbf{K}$ matrix to find the optimised weights $\mathbf{E}$. The shifting of indices that we operate, in order to solve this problem, is the following:

$$i' = i + 2 \tag{5.18}$$
$$j' = j + 1 \tag{5.19}$$

After this relabelling, we now have a $\mathbf{K}$ matrix which is lower triangular and invertible. We plot in Fig. 5.5 an example of such matrix.

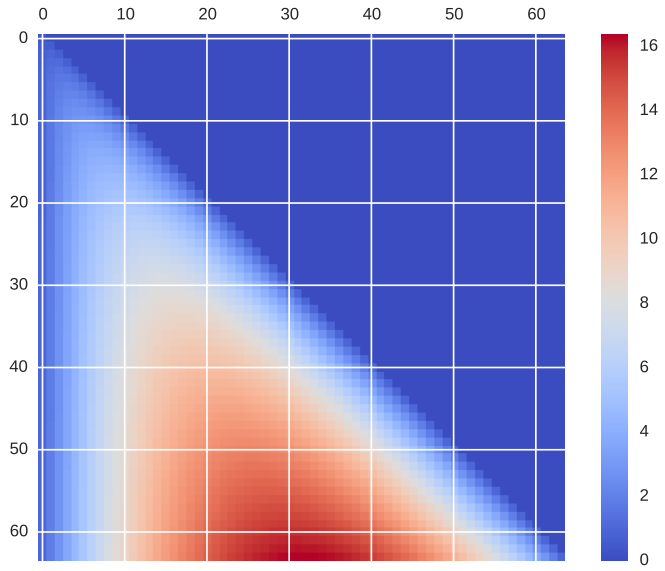

Figure 5.5: K matrix for a grid of 64 pixels.

Once the $\mathbf{K}$ matrix has been set up, it is straightforward to pass from the density field to the convergence field, simply acting with the $\mathbf{K}$ matrix on the $\delta(\vec{x})$ field. In Fig. 5.6 we show a typical κ field obtained with this approach. For the moment, we have deliberately not included any noise in

the data, as we are working in the approximation of infinite S/N ratio. We will come back to this point in the next chapter, when we implement the weights described in sect. 4.3, for the finite S/N regime, in the 2D and 3D case.

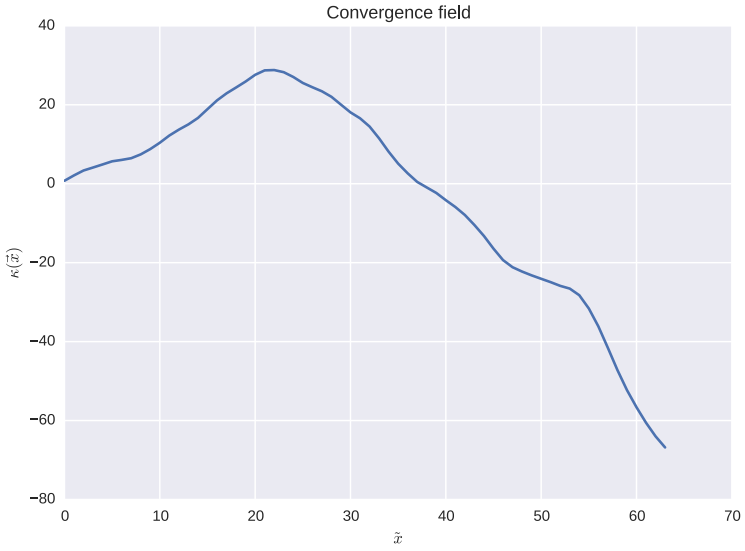

Figure 5.6: κ field for a grid of 64 pixels, obtained from a Gaussian power spectrum like the one of Eq.5.3, with $\tilde{\sigma} = 1.0$.

5.2 The correlation function

5.2.1 How to calculate it from the power spectrum

We now come to a crucial point in the algorithm for the recovery of the power spectrum. We need to create the matrix ξ, defined in sect. 4.1 by

$$\xi_{lm} = \int \frac{\mathrm{d}^n k}{(2\pi)^n} e^{-\mathrm{i}\vec{k}\cdot(\vec{x}_l - \vec{x}_m)} P(k) \tag{5.20}$$

In the 1D case this expression is simpler as there is a direct correspondence between the indices l and m of the matrix and those of the array of elements of the field. Instead, as we will see in the next chapter, this is no longer true in the 2D and 3D case and we will need to apply the same procedure used for the 1D case to a one-dimensional array containing all the points of the multidimensional grid. The previous relation becomes, in 1D:

$$\xi_{lm} = \int \frac{\mathrm{d}k}{2\pi} e^{-\mathrm{i}\, k \Delta x_{lm}} P(k) \tag{5.21}$$

where we indicated with Δx_{lm} the separation between two pixels labelled by indices l and m, $\Delta x_{lm} = x_l - x_m$. The first step is to calculate the correlation function, for our given Gaussian power spectrum, as a function of the separation Δ between elements of the field. We indicate it with η,

$$\eta(\Delta) = \frac{P_0}{2\pi\sigma} e^{-\frac{\Delta^2}{2\sigma^2}}. \tag{5.22}$$

Once we have this analytic expression as a function of the separation, we need to use it to fill the entries of the matrix ξ. However, before doing that, we need to keep into account that we are working with a discretised version of the correlation function.

5.2.2 The correlation function: discretisation

The discretisation urges us to pay attention when we calculate analytically the inverse Fourier transform of the power spectrum, as we need to multiply it for a prefactor that accounts for the discretisation done. To explicate this concept, let us first work out the relation between the correlation function, calculated directly from the definition as average of products of the field, and the Inverse Fast Fourier Transform (IFFT) of the power spectrum.
If we indicate with C the constant used by the routine that we employ to calculate the IFFT (for example, using Python's routine `np.fft.ifft`, $C = \frac{1}{N}$, where N is the dimension of the input array), we have that δ_j, the δ field in correspondence of the index j, can be written as

$$\delta_j = C \sum_{\tilde{k}} \delta_{\tilde{k}} e^{\mathrm{i} k_{\tilde{k}} x_j} = IFFT(\delta(k)) \tag{5.23}$$

namely as the IFFT of the field in k-space. Thus, if we now calculate the correlation function as a function of the separation, exploiting its definition and inserting Eq.5.23, we get

$$\eta(\Delta) \equiv \langle \delta_j \delta_{j+\Delta} \rangle = C^2 \frac{\sum_j}{N} \sum_{\tilde{k}} \sum_{\tilde{k}'} \delta^*_{\tilde{k}} \delta_{\tilde{k}'} e^{-\mathrm{i} k_{\tilde{k}} x_j} e^{\mathrm{i} k_{\tilde{k}} (x_j + \Delta)} \tag{5.24}$$

$$= \frac{C}{N} \left[C \sum_{\tilde{k}} P(\tilde{k}) e^{i k_{\tilde{k}} \Delta} \right] N \tag{5.25}$$

$$= C \times IFFT(P(\tilde{k})) \tag{5.26}$$

where we indicated with $IFFT(P(\tilde{k}))$ the IFFT of the power spectrum $P(\tilde{k})$. We exploited the definition of $P(\tilde{k})$ and the fact that when $k = k'$ we get a factor

$$\sum_j e^{\mathrm{i}(k_{\tilde{k}'}-k_{\tilde{k}})x_j} = \sum_j 1 = N. \tag{5.27}$$

Now we would like to shift from the discrete to the continuous approximation, transforming the summation into an integral. Therefore we start from Eq. 5.25 and we change from the summation to the integral, rewriting η as

$$\begin{aligned}
\eta(\Delta) &= \langle \delta_j \delta_{j+\Delta} \rangle & (5.28)\\
&= \frac{C}{N}\left[C\sum_{\tilde{k}} P(\tilde{k}) e^{ik_{\tilde{k}}\Delta}\right] N \to C^2 \frac{\int P(\tilde{k}) e^{ik_{\tilde{k}}\Delta} \mathrm{d}\tilde{k}}{\Delta\tilde{k}} & (5.29)\\
&= \frac{L}{2\pi} C^2 P_0 \int e^{-\frac{k^2\sigma^2}{2}} e^{\mathrm{i}k(\Delta\frac{L}{N})} \mathrm{d}k & (5.30)\\
&= \frac{L}{2\pi} C^2 \frac{\sqrt{2\pi}}{\sigma} P_0 e^{-\frac{(\Delta x)^2}{2\sigma^2}} & (5.31)\\
&= \frac{L}{\sqrt{2\pi}\sigma} C^2 P_0 e^{-\frac{(\Delta x)^2}{2\sigma^2}} & (5.32)
\end{aligned}$$

where we changed variable from $\tilde{k}$ to k, we set $\Delta\tilde{k} = 1$ and we defined $\Delta x = \Delta\, L/N$. Now we make explicit the dependence on the grid step:

$$\eta(\Delta) = \eta(\Delta\tilde{x}) = \frac{L}{\sqrt{2\pi}\tilde{\sigma}\frac{L}{N}} C^2 P_0 e^{-\frac{1}{2}(\frac{\Delta\tilde{x}\frac{L}{N}}{\tilde{\sigma}\frac{L}{N}})^2} = \frac{N}{\sqrt{2\pi}\tilde{\sigma}} C^2 P_0 e^{-\frac{1}{2}(\frac{\Delta\tilde{x}}{\tilde{\sigma}})^2} \tag{5.33}$$

To fill the matrix ξ we exploit the homogeneity and isotropy of the density field, which makes the correlation function depend only on the modulus of the separation between two elements of the field,

$$\xi_{lm} = \xi_{|l-m|} = \eta(\Delta\tilde{x}_{|l-m|}) = \eta(|\tilde{x}_l - \tilde{x}_m|). \tag{5.34}$$

The result is a matrix, ξ, that is symmetric and filled by bands, as shown in Fig. 5.7.

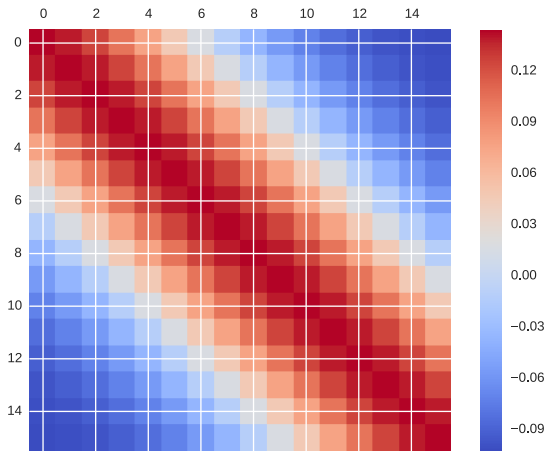

Figure 5.7: ξ matrix, plotted for a grid of $N = 16$ pixels and a power spectrum $P(k)$ like the one of Eq. 5.3, with $\tilde{\sigma} = 5.0$. This value of $\tilde{\sigma}$ has been chosen so that in this plot it is possible to better appreciate the Gaussian decrease of the values from the diagonal to the edges.

In Fig. 5.8 it is shown a comparison between the analytic expression of the correlation as a function of the separation, and the actual correlation function, obtained through a direct calculation from the elements of the field. From the plots shown we can appreciate how the analytic version of the correlation as a function of the separation faithfully represents the actual correlation of the elements of the field.

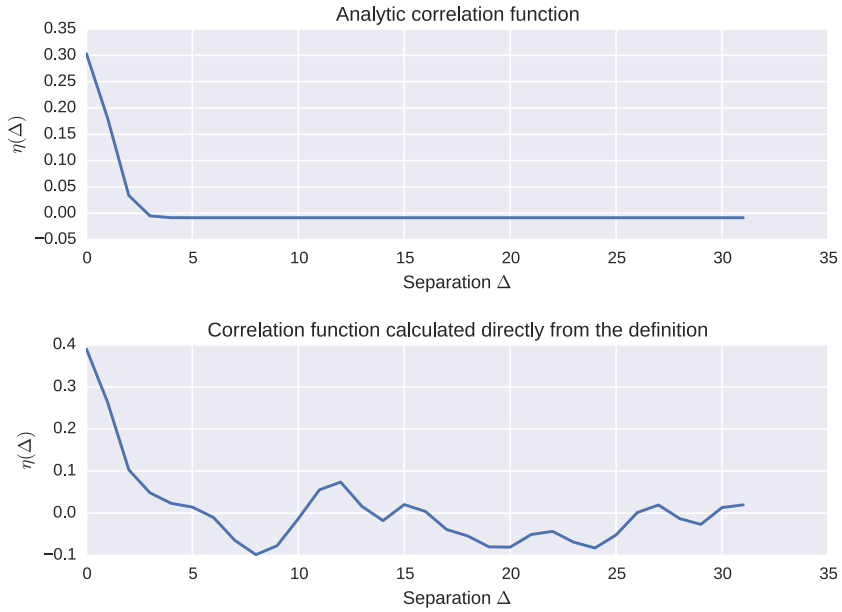

Figure 5.8: Comparison between the correlation function calculated analytically from the power spectrum (top) and directly from the realisation of the field, exploiting the definition given by Eq. 5.24 (bottom). Here we can see a lack of ergodicity due to the small N considered ($N = 64$). As $N \to \infty$, the two tend to agree more and more.

5.2.3 Approximation of the correlation function

We now need to work out the matrices A^α, that correspond, in the notation of sect. 4.1, to the expansion coefficients in the expression

$$\xi_{lm} = \int \frac{\mathrm{d}k}{2\pi} P(k) e^{-\mathrm{i}\, k \Delta x_{lm}} \equiv A^\alpha_{lm} P_\alpha \tag{5.35}$$

which represents a discretisation of the integral definition of the correlation function, as inverse Fourier transform of the power spectrum. The index α labels the wavenumber at which the power spectrum is evaluated. To find the A^α matrices, then, we explicitly evaluate the Fourier transform of the power spectrum in the 1D case and we discretise this relation, remembering to make explicit the dependence on the grid step:

$$\int \frac{\mathrm{d}k}{2\pi} P(k) e^{-\mathrm{i}\, k\Delta x_{lm}} \sim \sum_k P(k) e^{-\mathrm{i}k\Delta x_{lm}} \tag{5.36}$$

$$= \sum_{k>0} P(k) \left(e^{\mathrm{i}k\Delta x_{lm}} + e^{-\mathrm{i}k\Delta x_{lm}} \right) \tag{5.37}$$

$$= 2 \sum_{k>0} \cos\left(k\Delta x_{lm}\right) P(k) \tag{5.38}$$

$$= 2 \sum_{k>0} \cos\left(\tilde{k} \frac{2\pi}{L} \Delta\tilde{x}_{lm} \frac{L}{N} \right) P(\tilde{k}) \tag{5.39}$$

$$= 2 \sum_{k>0} \cos\left(\frac{2\pi}{N} \tilde{k} \Delta\tilde{x}_{lm} \right) P(\tilde{k}) \tag{5.40}$$

from which we derive that the expression for the A^α matrices, in the 1D case, is

$$A^\alpha_{lm} = 2\cos\left(\frac{2\pi}{N} \alpha \Delta\tilde{x}_{lm} \right) = 2\cos\left(\frac{2\pi}{N} \alpha (\tilde{x}_l - \tilde{x}_m) \right) \tag{5.41}$$

Here the index α is equivalent to the integer $\tilde{k}$.
In Fig. 5.9 we show the approximated version, obtained summing over α ($\xi = A^\alpha P_\alpha$), of the same ξ matrix in Fig. 5.7. From the plot we can appreciate how the approximated version assumes periodic boundary conditions, while the ξ matrix plotted in Fig.5.7, obtained through an analytic calculation, does not.

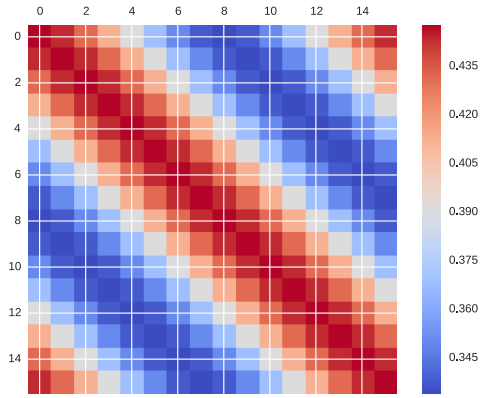

Figure 5.9: Approximation of the ξ matrix, obtained through the use of the A^{α} matrices. Note the periodic boundary conditions assumed, evident from the edges of the matrix, as opposed to the Gaussian non-periodic decay of Fig. 5.7.

5.3 Results and analysis

We are now at a point such that we have all the elements necessary to recover the power spectrum from our mock dataset of convergence field κ_i. Before proceeding and showing the results of this procedure, we would like to briefly summarise the algorithm we followed. The whole procedure aims at testing the estimator in a sort of "exercise" for the estimator, where the theoretical value of the power spectrum is known in advance and the estimator should recover it reasonably well. If this should not be true, then this would signal some serious problem in the theory of the estimator, gravely compromising its applicability to real experiments of weak lensing.

5.3.1 Summary of the algorithm for the recovery of the power spectrum

In short, the procedure can be summarised in the following steps (we refer the reader to sect. 4.1 for the notation used):

1. Choice of the initial power spectrum
2. Generation of the density field δ_i from the power spectrum
3. Creation of the kernel $\mathbf{K}$ matrix
4. Passage from the density field δ_i to the convergence field κ_i by means of the matrix $\mathbf{K}$

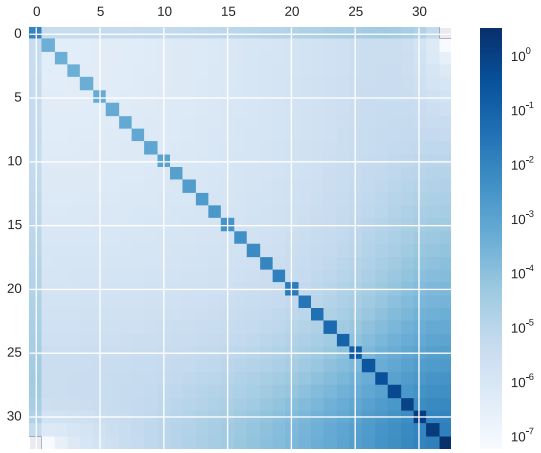

Figure 5.10: Fisher matrix for the Gaussian power spectrum with $\tilde{\sigma} = 1.0$

5. Creation of the ξ matrix from the correlation function, calculated analytically from the known power spectrum via inverse Fourier transform

6. Creation of the matrices A^{α}, coefficients of the expansion of the matrix ξ as a discrete summation of the power spectrum at different wavenumbers, labelled by α

7. Creation of the Fisher matrix $\mathbf{F}$, which is calculated simply through Eq. 4.16,

$$F_{\alpha\beta} = \frac{1}{2}\mathrm{Tr}(\xi^{-1}A_{\alpha}^{T}\xi^{-1}A_{\beta}) \tag{5.42}$$

   We show in Fig.5.10 an example of Fisher matrix.

   For every value of the integer α, labelling the wavenumber at which we want to recover the power spectrum, we then need to repeat the following operations:

8. In the notation of Sect. 4.1, create the matrix $\mathbf{G}^{\alpha}$

9. From $\mathbf{G}^{\alpha}$ get $\mathbf{E}^{\alpha}$, by inversion of the $\mathbf{K}$ matrix

10. From $\mathbf{E}^{\alpha}$ find the quadratic combination y^{α} and multiply the array $\mathbf{y}$ obtained by the inverse of the Fisher matrix, $\mathbf{F}^{-1}$, on the left, so as to get an unbiased estimate of the power spectrum.

Once we get an estimate of $P(k)$, we can then study the goodness of the recovered data by analysing different characteristics of the estimator and the data, such as the window functions W, or performing a χ^2 analysis on the recovered spectrum, obtaining a best fit of the data. We will describe these operations in the following sections, as well as presenting some examples of recovered power spectra.

5.3.2 χ^2 analysis of the recovered power spectrum

In order to quantify the goodness of the recovered power spectrum ,we need to perform a χ^2 analysis, comparing the recovered power spectrum and the input one, and ultimately producing a best fit of the data. However, we cannot proceed with the ordinary χ^2 theory that is normally used to find the best fit of a set of data. This is due to the fact that, contrarily to what usually happens, we are dealing with measurements that are correlated, therefore the covariance matrix is not diagonal and this modifies the formulas for the χ^2.
Let us be more explicit by revising the usual situation, considering a series x_i of n measurements, labelled by the index i, completely uncorrelated between each other and with $\sigma_i, i = 1...n$ errors on them. The covariance matrix for this set of measurements looks like:

$$\mathbf{C}_{ij} = \begin{pmatrix} \sigma_1^2 & 0 & 0 & \dots \\ 0 & \sigma_2^2 & 0 & \dots \\ 0 & 0 & \ddots & \ddots \\ \dots & \dots & \dots & \sigma_n^2 \end{pmatrix} \tag{5.43}$$

Let us now consider $p(\vec{\lambda}|\vec{x})$, the probability that a set of parameters, collectively grouped in the vector $\vec{\lambda}$, represent our theory, given the set of measurements x_i, in turn grouped in the vector $\vec{x}$. This probability is given by

$$p(\vec{\lambda}|\vec{x}) = \frac{p(\vec{x}|\vec{\lambda})p(\vec{\lambda})}{p(\vec{x})} \tag{5.44}$$

$$\propto p(\vec{x}|\vec{\lambda}) = \mathcal{L}. \tag{5.45}$$

Thus, if we take $p(\vec{\lambda})$, the probability of the parameters, to be a constant ("uniform prior"), we find that $p(\vec{\lambda}|\vec{x})$ is proportional to the Likelihood $\mathcal{L}$. If we assume the σ_i^2 to be Gaussian errors on $\vec{x}$ and uncorrelated, then the probability of one x_i, given the parameters, is

$$p(x_i|\vec{\lambda}) = \frac{1}{\sqrt{2\pi}\sigma_i} \exp\left[-\frac{1}{2}\frac{(x_i - t_i(\vec{\lambda}))^2}{\sigma_i^2}\right] \tag{5.46}$$

where we indicated with $t_i(\vec{\lambda})$ the theoretical value correspondent to x_i. If the x_i measurements are independent, then,

$$p(\vec{x}|\vec{\lambda}) \propto \frac{1}{\prod_i \sigma_i} \exp\left[-\frac{1}{2}\sum_i \frac{(x_i - t_i(\vec{\lambda}))^2}{\sigma_i^2}\right] \tag{5.47}$$

where $\sum_i \frac{(x_i - t_i(\vec{\lambda}))^2}{\sigma_i^2}$ is the χ^2 of the measurements. We notice that we can rewrite it as

$$\chi^2 = \sum_i \frac{(x_i - t_i(\vec{\lambda}))^2}{\sigma_i^2} = (x_i - t_i(\vec{\lambda}))C_{ij}^{-1}(x_j - t_j(\vec{\lambda})) \tag{5.48}$$

exploiting the diagonal form of the covariance matrix $\mathbf{C}$ given by Eq.5.43. In our case, the errors σ_i on the recovered values of the power spectrum are correlated, so Eq. 5.47 is no longer valid at face value. We need to consider a generalisation of the expressions provided, namely a generalised χ^2 where the covariance matrix is not necessarily diagonal:

$$p(\vec{x}|\vec{\lambda}) \propto \frac{1}{\det\mathbf{C}} \exp\left[-\frac{1}{2}\sum_{ij}(x_i - t_i(\vec{\lambda}))C_{ij}^{-1}(x_j - t_j(\vec{\lambda}))\right] \tag{5.49}$$

with the new χ^2 given by

$$\chi^2 = \sum_{ij}(x_i - t_i(\vec{\lambda}))C_{ij}^{-1}(x_j - t_j(\vec{\lambda})) \tag{5.50}$$

In the case when we produce an unbiased estimate of the power spectrum we have $\mathbf{C} = \mathbf{F}^{-1}$, therefore Eq.5.50 becomes

$$\chi^2 = \sum_{ij}(x_i - t_i(\vec{\lambda}))F_{ij}(x_j - t_j(\vec{\lambda})) \tag{5.51}$$

Given this generalised version of the χ^2, the procedure to quantify the goodness of the recovered power spectrum is based on the calculation of Eq. 5.51 for a grid of different parameters (those that describe our curve: for example, the amplitude and width of the Gaussian) with the purpose of finding where the minimum value happens to be. The set of parameters that minimise the χ^2 is the set that best describe our experimental data: we have thus provided a best fit for the data. To quantify the goodness of it, we need to evaluate the difference $\Delta\chi^2 = \chi^2 - \chi^2_{min}$ and see if it falls between predetermined intervals known from the literature (Press (2007)). We report here three reference values of $\Delta\chi^2$, corresponding to three different Confidence Levels p:

$\Delta\chi^2$	p
2.30	68.27%
4.61	90%
6.18	95.45%

5.3.3 Recovered power spectra and window functions

In Fig. 5.11, 5.12 and 5.13 we present plots of the recovered power spectrum, obtained following the procedure described before, starting from an input power spectrum with $\tilde{\sigma} = 1.0$, superimposed for a graphical comparison. We can see that the shape of the power spectrum is well recovered. The errorbars are given by the square roots of the diagonal elements of the covariance matrix, which in this case corresponds also to the inverse of the Fisher matrix. Later on we will present other combinations of the data, essentially given by a multiplication of the raw data vector $\mathbf{y}$ for another invertible matrix: in those cases we will have different errorbars.
We also plot the best fits of the data, obtained through the χ^2 analysis described in subsection 5.3.2: in this regard, we also present the grid of values for which we calculate the chi square and we find the minimum. We choose to parametrize our power spectrum with a canonical amplitude A and a width $\hat{\sigma}$, so that

$$P(k) = A\, e^{-\frac{k^2}{2\hat{\sigma}^2}} \tag{5.52}$$

In the χ^2 plots we can appreciate the contour plots of $\Delta\chi^2 = \chi^2 - \chi^2_{min}$ for the reference values of Tab. 5.3.2 and the value corresponding to the actual data. In the same plots we also show the window functions (rows of $\mathbf{W}$), for certain values of $\tilde{k}$: what we find is a $\mathbf{W}$ matrix essentially resembling a Kronecker delta, therefore the window functions manage to isolate a certain scale. Furthermore, considering the correlation matrix $\mathbf{C}_{\alpha\beta}$, defined by

$$\mathbf{C}_{\alpha\beta} = \frac{\mathbf{V}_{\alpha\beta}}{\sqrt{\mathbf{V}_{\alpha\alpha}\mathbf{V}_{\beta\beta}}} \tag{5.53}$$

where the covariance $\mathbf{V}_{\alpha\beta}$ of the estimator is defined by Eq. 4.13,

$$\mathbf{V}_{\alpha\beta} = \left\langle \left(P_\alpha - \hat{P}_\alpha\right)\left(P_\beta - \hat{P}_\beta\right)\right\rangle = 2\mathrm{Tr}\left(\xi\mathbf{K}^T\mathbf{E}^\alpha\mathbf{K}\xi\mathbf{K}\mathbf{E}^\beta\mathbf{K}^T\right) \tag{5.54}$$

we note that the off-diagonal elements of the $\mathbf{C}$ matrix are very small, indicating that the estimates of the power spectrum are close to be uncorrelated (although formally they are not). We speculate that this could be a consequence of the fact that we are dealing with small arrays, therefore we have a limited number of k-modes over the range where the power spectrum

changes from 1 to 0. These modes are well separated, making the estimates almost uncorrelated: however, if we had considered larger arrays then we would have had closer modes and the situation might have changed, leading to more correlated estimates of the power spectrum.

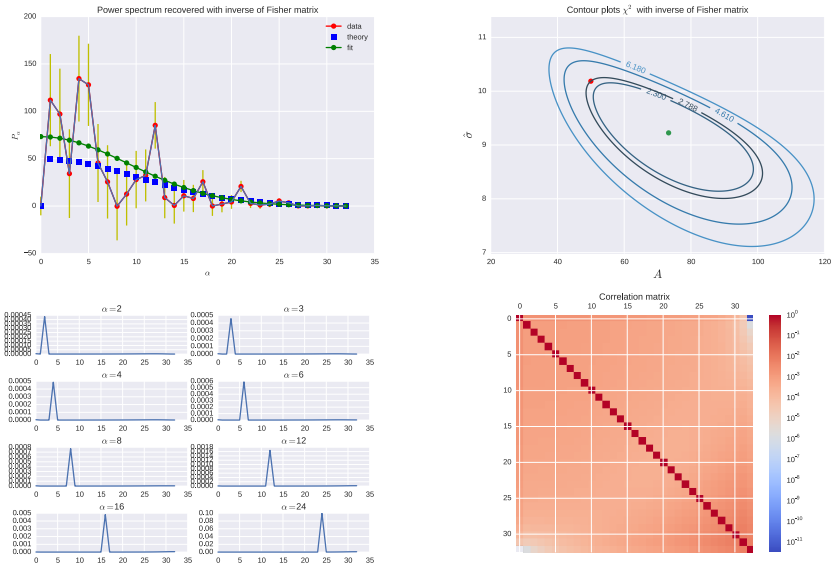

Figure 5.11: (Top row) Recovered power spectrum (left), superimposed to the theoretical one, and the best fit coming from the χ^2 analysis, whose contour plots are also shown (right). (Second row) Window functions and correlation matrix for the recovered power spectrum. All these plots are relative to a one-dimensional grid with 64 pixels (the possible values for k therefore range from 0 to 32) and a Gaussian power spectrum with $\tilde{\sigma} = 1.0$.

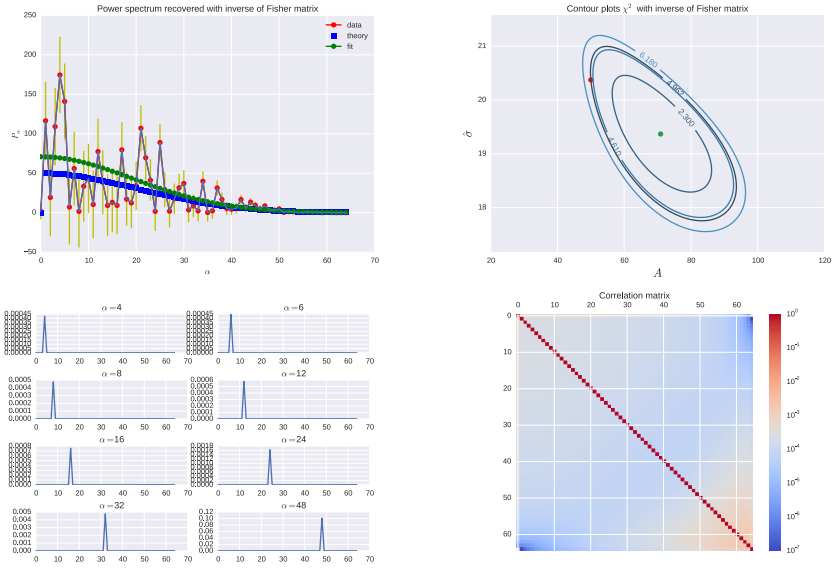

Figure 5.12: Same as 5.11, but for a grid of 128 pixels.

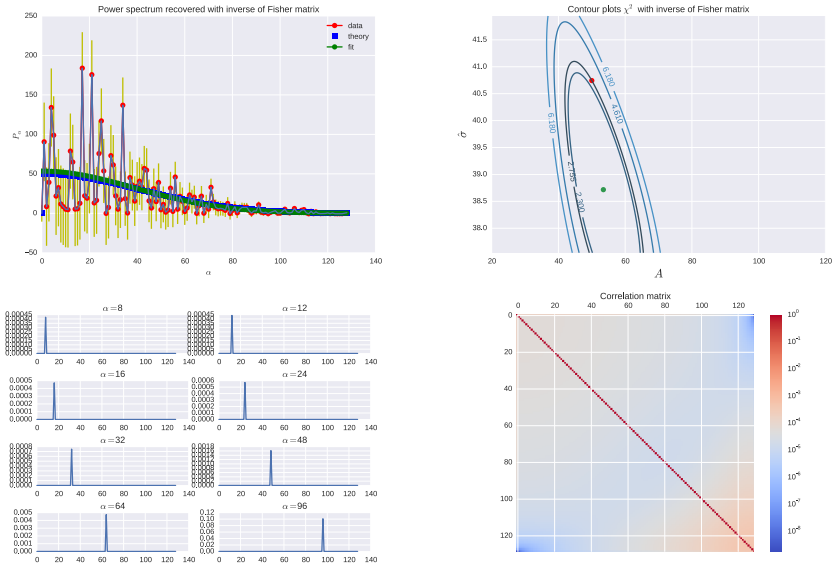

Figure 5.13: Same as 5.11, but for a grid of 256 pixels.

5.3.4 Varying the width of the power spectrum

As regards the window functions, we would like to point out an interesting feature that we discovered in our testing of the estimator. In order to show this point, we present in Fig. 5.14 a series of plots of window functions, plotted as the value $\tilde{\sigma}$ of the input power spectrum varies.
We notice the appearance of an unexpected feature at the Nyquist frequency, which grows as the value of $\tilde{\sigma}$ grows. We do not know how to exactly interpret this feature, although we suspect that it might be of numerical origin. In any case, as we will see in the next chapter, the implementation of the weights optimised for a finite S/N ratio allows the estimator to recover well the form of the power spectrum despite this strange feature that persists in the window functions. For this reason, although it remains an unresolved issue which needs further investigation, it was not treated as high priority.

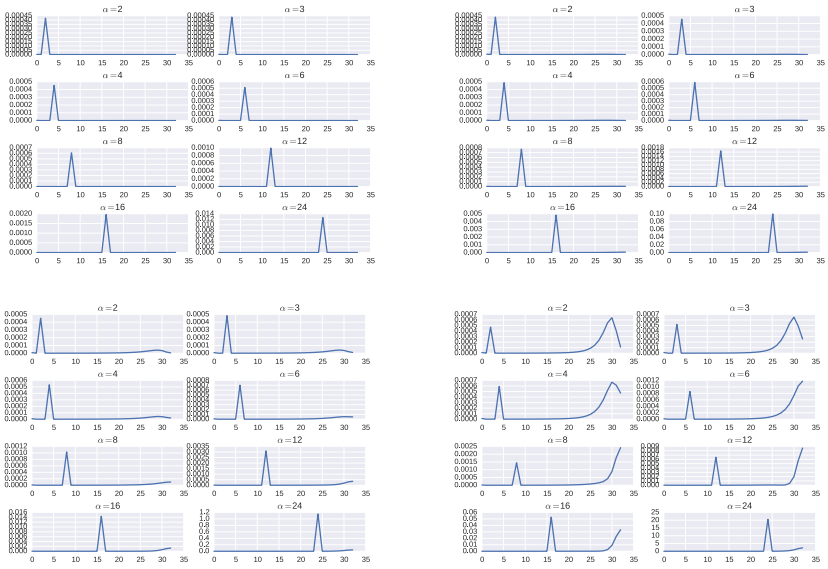

Figure 5.14: Window functions for the recovered power spectrum, for different values of $\tilde{\sigma}$: from left to right, from top to bottom, $\tilde{\sigma} = 0.8, 1.0, 1.2, 1.4$, respectively. The number of pixels of the grid is always 64.

5.3.5 Implementing different linear combinations of the data

As anticipated before, we now come to point when we would like to test different linear combinations of the raw data, so as to trade off the covariance of the data with the size of the errorbars. We follow the description provided in section 3.1.2 to identify the different linear combinations. In particular, we implement the Choleski decomposition

$$\mathbf{F} = \mathbf{L}\mathbf{L}^T \tag{5.55}$$

with $\mathbf{L}$ lower triangular. The combination considered is $\mathbf{X}\mathbf{y}$ with $\mathbf{X} = \mathbf{L}^{-1}$. This procedure clearly does not give an unbiased estimate of the power spectrum, therefore in order to compare the recovered and the input power spectrum we need to multiply the input $P(k)$ by $\mathbf{X}\mathbf{F} = \mathbf{L}^T$. We also implement the combination $\left(\mathbf{L}^{-1}\mathbf{y}\right)^t$, which has the interesting property to have a lower triangular window matrix as shown later on in this Section. In this case we need to plot $\mathbf{c}^t\mathbf{L}$ in order to compare the biased estimate of the power spectrum with a rescaled version of the original one. We thus obtain estimates of the power spectrum like those shown in Fig.5.15.
in fact $\left\langle \left(\mathbf{L}^{-1}\mathbf{y}\right)^t \right\rangle = \mathbf{c}^t\mathbf{L}$, where $\mathbf{c}$ represents the vector of the true power spectrum.

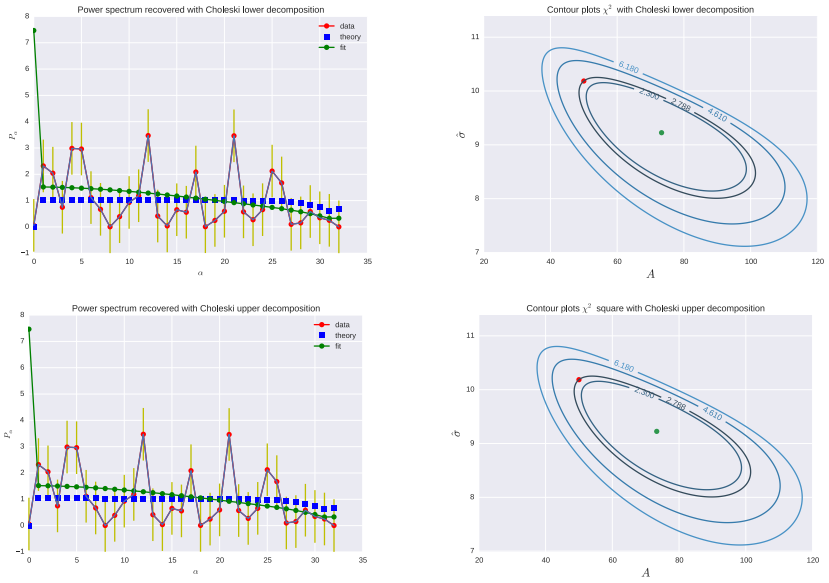

Figure 5.15: Linear combinations of the power spectra and χ^2 contour plots for the linear combinations described in the text, namely $\mathbf{X}\mathbf{y}$ with $\mathbf{X} = \mathbf{L}^{-1}$ (top) and $\left(\mathbf{L}^{-1}\mathbf{y}\right)^t$ (bottom). $P(k)$ is originally the usual Gaussian with $\tilde{\sigma} = 1.0$, but needs to be rescaled to be compared with the biased estimates provided.

Alongside the power spectrum we plotted the χ^2 contour plots: as expected, they did not change, as we only considered linear combinations of the data. However, if we consider the new errorbars given by the square roots of the diagonal elements of the new covariance matrix, they are different from the

case when we multiplied by the inverse Fisher matrix. Let us now give an explicit expression of the new covariance matrix. If we call $\mathbf{q}$ the new combination of data, in the first case we have $\mathbf{q} = \mathbf{X}\mathbf{y}$ and if we calculate the covariance $\mathbf{C}$ from its definition (assuming for simplicity and without loss of generality that $\langle \mathbf{q} \rangle = 0$), we find

$$\mathbf{C} \equiv \left\langle \mathbf{q}\mathbf{q}^t \right\rangle = \left\langle (\mathbf{X}\,\mathbf{y})\ (\mathbf{X}\mathbf{y})^T \right\rangle \tag{5.56}$$

$$= \mathbf{X} \left\langle \mathbf{y}\mathbf{y}^t \right\rangle \mathbf{X}^t \tag{5.57}$$

$$= \mathbf{X}\,\mathbf{F}\,\mathbf{X}^T \tag{5.58}$$

$$= \mathbb{1}. \tag{5.59}$$

where we exploited Eq. 3.29, $\left\langle \mathbf{y}\mathbf{y}^t \right\rangle = \mathbf{F}$. Following similar calculations we can show that the same relation holds for the case $\left(\mathbf{L}^{-1}\mathbf{y}\right)^t$.
Let us now give an explicit expression for the new window functions, which we denote by S_{ij}. For $\mathbf{q} = \mathbf{X}\mathbf{y}$ we consider

$$\langle \mathbf{q} \rangle = \langle \mathbf{X}\mathbf{y} \rangle = \left\langle (\mathbf{L}^{-1})\mathbf{y} \right\rangle = \left[(\mathbf{L}^{-1})\mathbf{F} \right] \mathbf{P} = \mathbf{L}^t \mathbf{c} \tag{5.60}$$

where $\mathbf{c}$ denotes the true power spectrum, we can then identify the window functions as

$$S_{ij} = L^t_{ij} \tag{5.61}$$

or, in matrix notation, $\mathbf{S} = \mathbf{L}^T$, i.e. they are upper triangular. For $\left(\mathbf{L}^{-1}\mathbf{y}\right)^t$ we have

$$\left\langle \left(\mathbf{L}^{-1}\mathbf{y}\right)^t \right\rangle = \left\langle \mathbf{y}^t \left(\mathbf{L}^{-1}\right)^t \right\rangle = \mathbf{c}^t\,\mathbf{L} \tag{5.62}$$

i.e. we have a lower triangular window matrix. We plotted some of the window functions (rows of the window matrices) in Fig. 5.16.

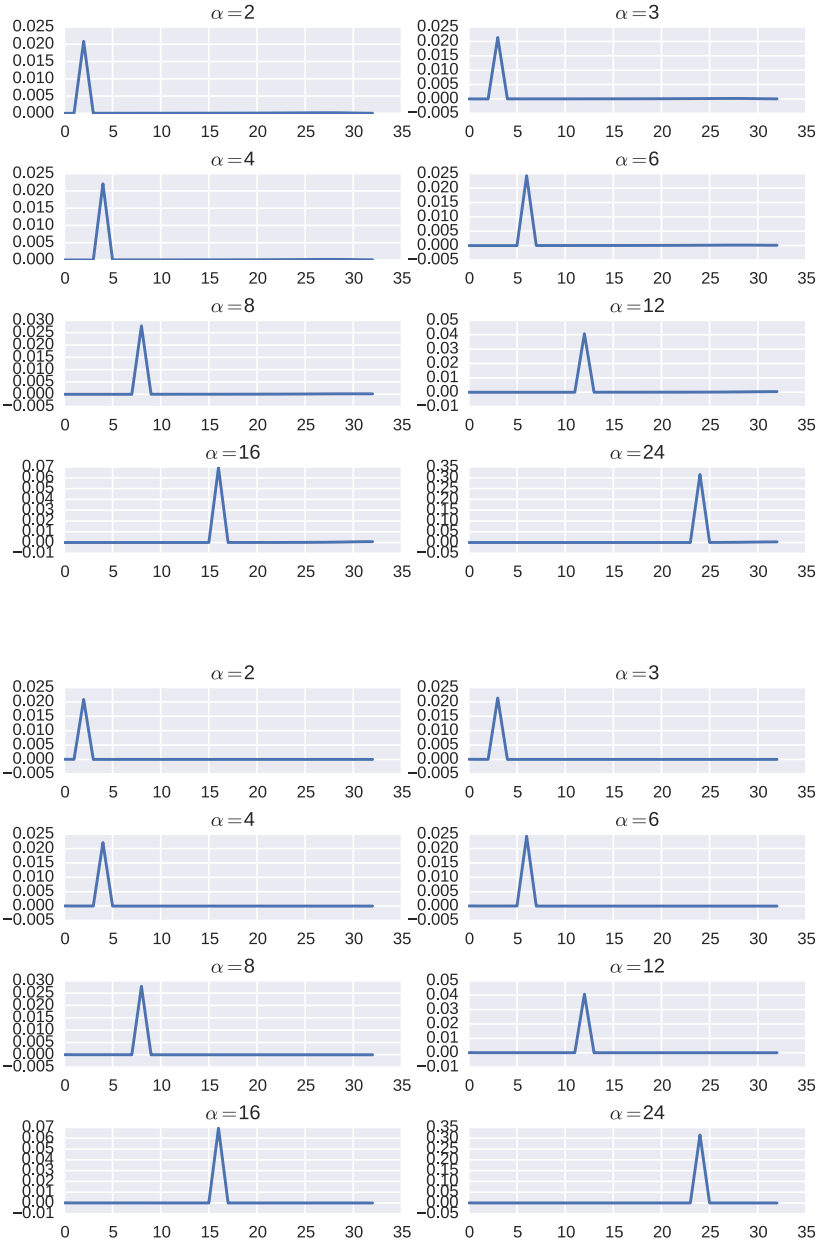

Figure 5.16: Window functions for the different linear combinations described in the text, namely $\mathbf{L}^{-1}\mathbf{y}$ (top) and $\left(\mathbf{L}^{-1}\mathbf{y}\right)^{t}$ (bottom). The original power spectrum is always a Gaussian with $\tilde{\sigma} = 1.0$. In this particular case the window functions are not only upper triangular (top) or lower triangular (bottom), but also extremely peaked around the wavenumber k, labelled by the integer α, of the corresponding row of the window matrix.

Chapter 6

Testing the estimator in two and three dimensions

We will now present the extension of the novel quadratic estimator for $P(k)$ to a 2D and 3D analysis, providing an insight into the simulations carried out on the estimator in two and three dimensions. The essential testing mechanism of the estimator is unchanged, conceptually following the same steps described in the unidimensional case (see Sect. 5.3.1): in summary, we choose an input power spectrum, create a mock dataset from it and we see how well the estimator recovers the original $P(k)$. However, some technical implementations differ significantly in the 2D and 3D case. This applies in particular to the creation of the mock dataset, which is now generated on a two- and three- dimensional grid. Namely, we generate a convergence field on a square and a cube: this not only implies a different technical approach to the creation of the field, but also calls for a shrewd storage of the data into a unidimensional vector, from the original 2D or 3D field. We will extensively investigate this feature in Sect. 6.1.4, but we anticipate here that, being the recovery of the power spectrum essentially a unidimensional procedure (as $P(k)$ depends only on the modulus of the wavenumber), we need a mapping between the two- or three- dimensional field and a unidimensional data vector that contains all the elements of the field. Let us now start from the description of the 2D testing of the estimator, subsequently moving to the 3D analysis. In both cases we will focus on the main differences with the 1D case, referring the reader to the previous chapter for those parts of the algorithm that are unchanged from the unidimensional analysis.

6.1 The 2D case

6.1.1 Tomographic approach

The tomographic approach followed in the 2D case is based on a planar configuration, that we can visualize starting from the 1D line of sight in Fig. 5.1 and considering multiple lines of sight, placed next to each other and extending *along* the direction of observation. In other words, we do not consider a planar image of the sky, extending orthogonally to the line of sight between the observer and the distribution of matter: contrastingly, we consider a planar grid along the direction of observation. The motivation behind this choice is that, as we will see in detail later on in the chapter, this allows us to take advantage of some of the techniques already employed in the 1D case, appropriately reinterpreted. We can appreciate the new geometrical configuration in Fig. 6.1, where we reproduce a view of the survey from above and the modelisation given in terms of a square grid. We choose a square grid for our survey: in particular, not only we set the dimensions L_x and L_y of the two axes to be the same, $L_x = L_y$, but we also consider the same number of pixels in each direction, $N_x = N_y$. We will come back to this important aspect, common to the 3D analysis, in the concluding chapter, where we will outline some of the possibilities that could result from changing this feature. For the moment, let us consider $L_x = L_y$ and $N_x = N_y$, and let us describe the generation of the 2D density field from a given power spectrum.

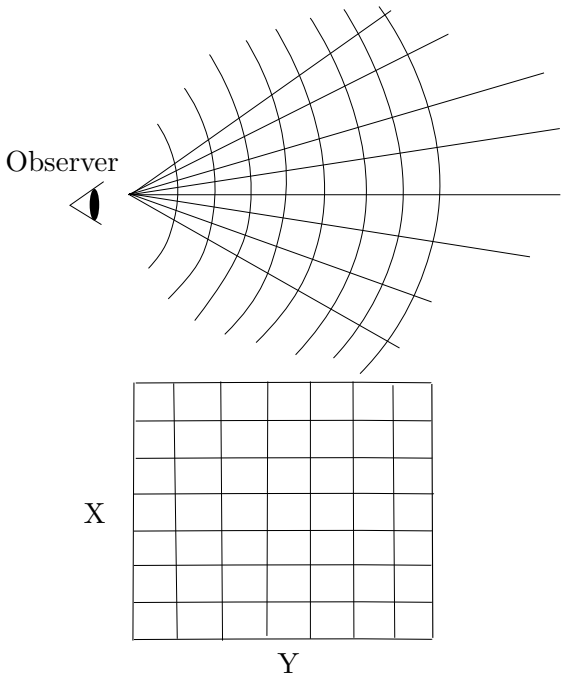

Figure 6.1: Seen *from above*: tomographic approach in 2D and modelisation given in terms of a square grid. The planar configuration lies *along* the direction of observation.

6.1.2 Choice of the input power spectrum

Regarding the options for our input power spectrum, we stick to the choice of the Gaussian already made for the 1D case. We decide to use the form

$$P_0\, e^{-\frac{\left(k_x^2\sigma_x^2+k_y^2\sigma_y^2\right)}{2}}, \tag{6.1}$$

P_0 being a constant, in the following always set equal to 50. This is a general, potentially anisotropic form for the power spectrum: for our purposes we will choose an isotropic power spectrum $P(k) = P(\sqrt{k_x^2 + k_y^2})$, by requiring $\sigma_x = \sigma_y$. Said L_x and L_y the physical lengths of the axes of our grid and N_x and N_y the number of pixels in each direction, such that

$$k_x = \tilde{k}_x \frac{2\pi}{L_x}, \quad k_y = \tilde{k}_y \frac{2\pi}{L_y}, \tag{6.2}$$

$$\sigma_x = \tilde{\sigma}_x \frac{L_x}{N_x}, \quad \sigma_y = \tilde{\sigma}_y \frac{L_y}{N_y}, \tag{6.3}$$

we can express Eq. 6.1 in terms of the grid steps as

$$P(k) = P_0\, e^{-\frac{1}{2}\left(\left(\tilde{k}_x \frac{2\pi}{L_x}\right)^2 \left(\tilde{\sigma}_x \frac{L_x}{N_x}\right)^2 + \left(\tilde{k}_y \frac{2\pi}{L_y}\right)^2 \left(\tilde{\sigma}_y \frac{L_y}{N_y}\right)^2\right)} \tag{6.4}$$

$$= P_0\, e^{-\frac{1}{2}\left(\frac{2\pi}{N}\right)^2 \left(\tilde{k}_x^2 \tilde{\sigma}_x^2 + \tilde{k}_y^2 \tilde{\sigma}_y^2\right)} \tag{6.5}$$

$$= P_0\, e^{-\frac{1}{2}\left(\frac{2\pi}{N}\right)^2 \tilde{\sigma}^2 \left(\tilde{k}_x^2 + \tilde{k}_y^2\right)}. \tag{6.6}$$

The simplest choice to satisfy $\sigma_x = \sigma_y$ is to put $L_x = L_y \equiv L$ and $N_x = N_y \equiv N$, from which it follows $\tilde{\sigma}_x = \tilde{\sigma}_y \equiv \tilde{\sigma}$. As we will see in the concluding chapter, there are very good reasons to desire to have far fewer pixels in the radial direction than in the angular direction, but for the moment we stick to the choice $N_x = N_y$, referring the reader to the concluding chapter for a discussion of different possibilities. We show in Fig.6.2 an example of such power spectrum, for $N = L = 32$ and $\tilde{\sigma} = 1.0$. Since we expect the power spectrum to be isotropic, we also impose that $P(k) = 0$ for $k > k_{Nyq}$, the Nyquist frequency. This follows from the fact that, with wavenumbers that are directed along an axis, we cannot have any power beyond the Nyquist frequency. Then it is appropriate to truncate the power spectrum for modes that are at some angle with respect to an axis: if this did not happen, then we could have anisotropic power, for example along the diagonal of the square grid (up to $\sqrt{2} \times k_{Nyq}$, see Fig. 6.9 later on), while we would not have power going along the axes. In other words, within the constraints given by the discreteness of our grid, we want to make the power spectrum as much isotropic as we can: by truncating the power spectrum when the modulus of k reaches the Nyquist frequency, regardless of the direction, we aim at treating all the directions as equally as we can.

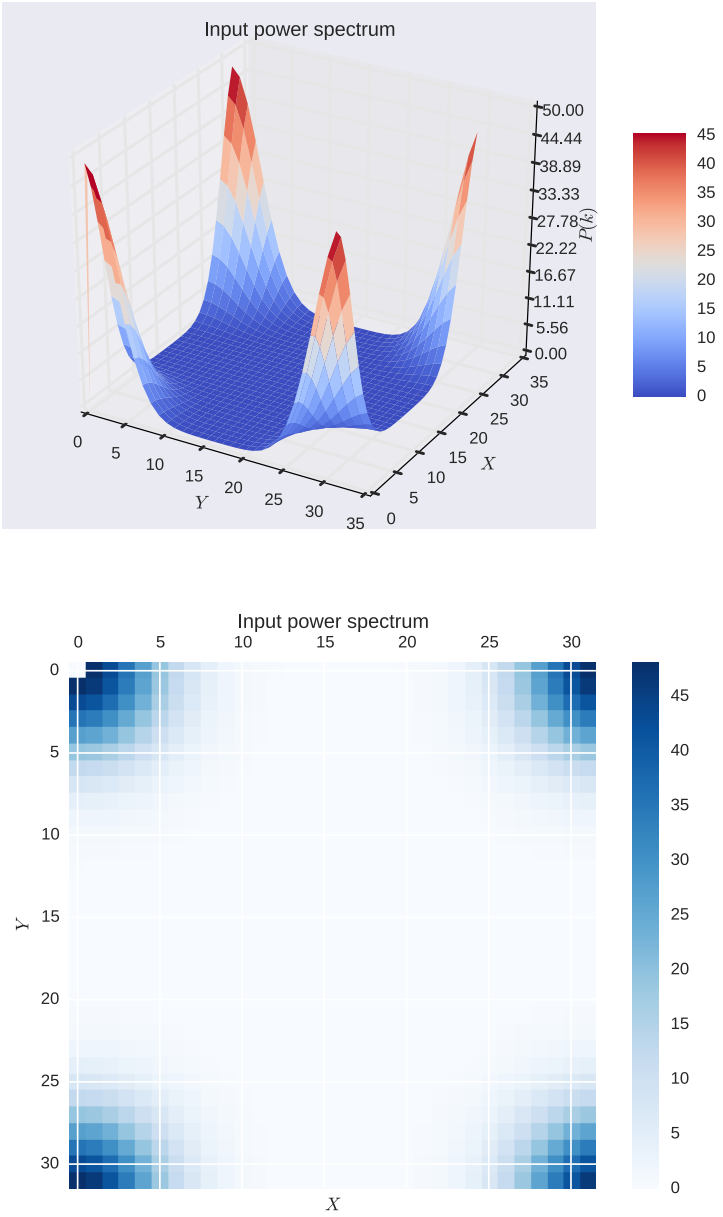

Figure 6.2: Input 2D Gaussian power spectrum, presented in a 3D plot and on the grid. The analytic form is given by Eq. 6.6, with $\tilde{\sigma} = 1.0$. As in the 1D case, the "wrapping" effect around the Nyquist frequency is due to the presence of positive and negative frequencies plotted on both the axes.

6.1.3 The generation of the density field

We now want to specify the treatment of Sect. 5.1.2, valid for all dimensions, to the two-dimensional grid discussed insofar. The generation of the density field $\delta(\vec{x}) = \delta(x, y)$ is still carried out passing through the coefficients $\delta(\vec{k}) = \delta(k_x, k_y)$ in Fourier space. Therefore we still have to respect the symmetry $\delta(\vec{k}) = \delta^*(-\vec{k})$, due to the reality of the field in configuration space. In two dimensions this relation becomes

$$\delta(k_x, k_y) = \delta^*(-k_x, -k_y). \tag{6.7}$$

We plot in Fig. 6.3 a typical two-dimensional grid and the way it has been divided to account for Eq. 6.7. We see how we need to generate a complex $\delta(\vec{k})$, made up of independently generated $\mathrm{Re}\,\delta(\vec{k})$ and $\mathrm{Im}\,\delta(\vec{k})$, for only half of the plane, the other half being filled according to Eq. 6.7. A special treatment is reserved to the elements of the grid whose index k_x and/or k_y is equal to the Nyquist frequency $N_x/2$ or $N_y/2$. These elements are indicated by the bands in Fig. 6.3: they are set real and such that $\mathrm{Re}\,\delta(\vec{k}) = \mathrm{Re}\,\delta(-\vec{k})$. This happens because at the Nyquist frequency we have a turning point between positive and negative frequencies, but the Nyquist frequency itself plays both roles of positive and negative frequency at the same time.
Once we have set up the field following the indications described, we transform it via a two-dimensional IFFT and we obtain a field in configuration space, which we can consider as purely real to within numerical precision, the imaginary part being negligible as shown in Fig. 6.4 and 6.5. The reality of the field in configuration space represents a good test to verify that the Fourier coefficients have been set up correctly.

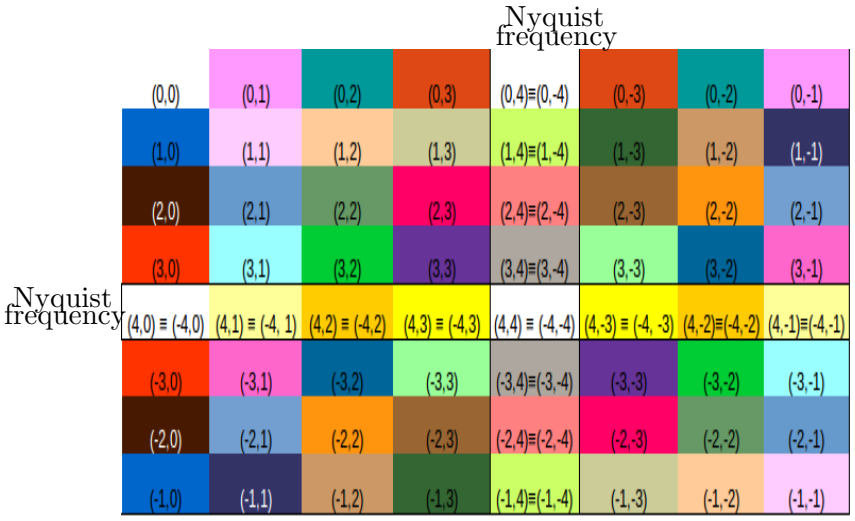

Figure 6.3: An example of 2D grid for the generation of the density field. In this case $N_x = N_y = 8$. The numbers written between parentheses are the couples (k_x, k_y) in Fourier space. We used the same colours to match couples that are complex conjugates, respecting Eq. 6.7 as required by the reality of the field in configuration space. The modes at the Nyquist frequency (included between bands in the figure) receive a special treatment, as explained in the text.

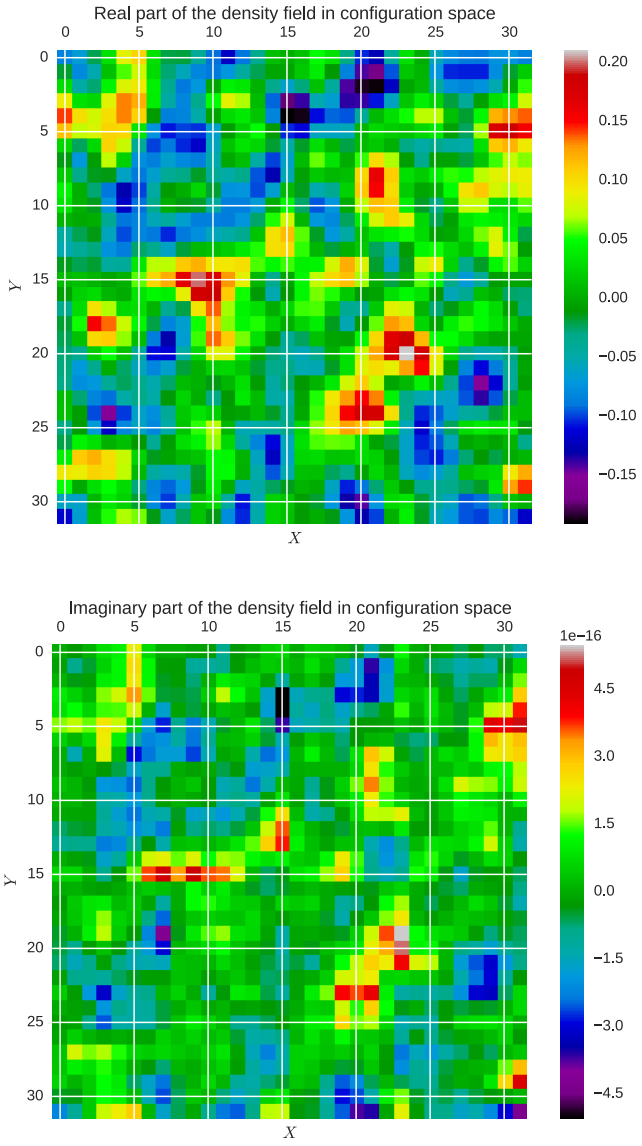

Figure 6.4: Plot on the grid of the real and imaginary part of the density field generated from a Gaussian power spectrum with $\tilde{\sigma}_x = \tilde{\sigma}_x = 1.0$. As expected, the imaginary part is negligible and we will ignore it in the following.

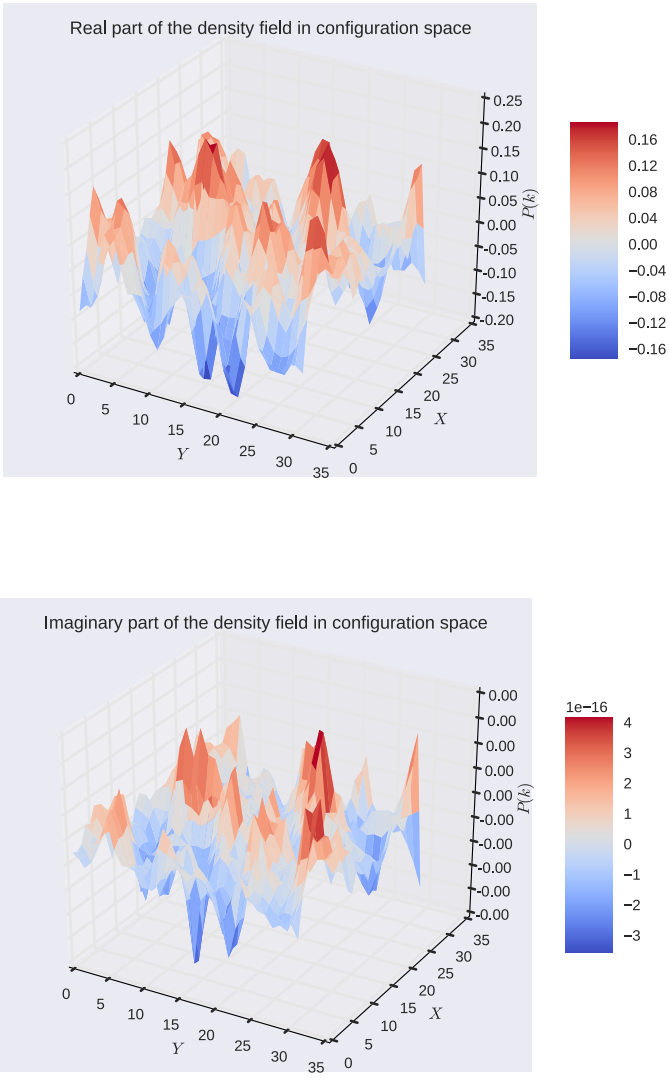

Figure 6.5: Same as Fig.6.4, this time in a 3D plot.

6.1.4 From the density to the convergence field

In order to pass from the density to the convergence field we still need a K matrix, representing a two-dimensional discretised version of the lensing kernel function, Eq. 5.15. In building this matrix our tomographic approach, based on a planar configuration parallel to the line of sight, reveals all its utility. In fact, as described before, we can consider the square grid as composed of multiple repeated lines of sight, placed next to each other, and proceed in filling the K matrix by applying to each of these lines the same reasoning applied to the single line of sight of the 1D case. This implies that, for every line of sight, we consider the convergence in the position labelled by index i to depend on the density field along the line sight from the observer *until* the position i, but not beyond it. We apply this hypothesis to every line of sight and we consider the various lines of sight to be independent of each other, in the sense that the convergence on one line of sight does not depend on the density field on another line. Furthermore, we adopt the "distant observer" approximation, considering the different lines of sight all parallel to each other. Within the "distant observer" approximation we could be concerned about density fluctuations coming from outside the "box" (with this term we refer to either a planar or volumetric configuration, as the same 2D reasoning applies to the 3D case). However, for the purposes of our exercise, we assume that this is not true and that the density fluctuations are therefore confined to the box. With these approximations, we find a K matrix which is lower triangular, simply resulting from the same 1D kernel matrix, repeated as many times as the number of lines that constitute our grid. We can see an example of such matrix in Fig. 6.6.

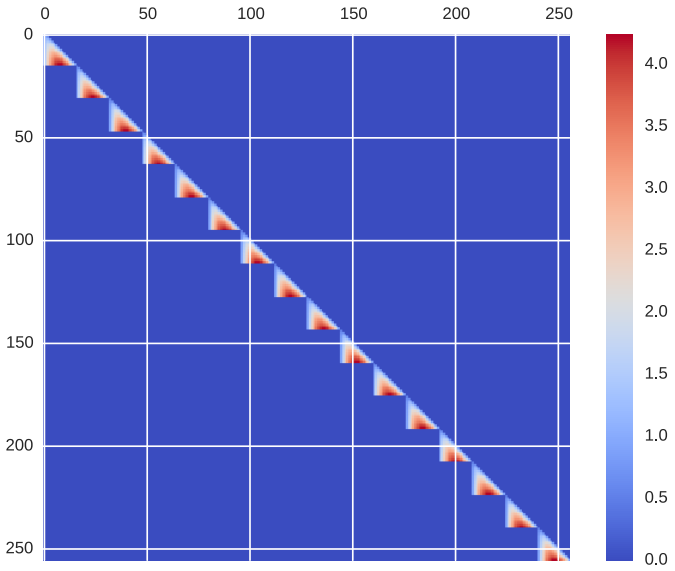

Figure 6.6: K matrix in the case of a grid of 16×16 pixels. We chose to plot this particular dimension to better illustrate how the 2D kernel matrix is essentially the repetition of the 1D K matrix along the diagonal.

We need to keep track of how we built the kernel matrix when we store our data. In fact, it is clear from the previous description that our K matrix will be a $(N_x \times N_y) \times (N_x \times N_y) = N^4$ matrix, being essentially N times the repetition along the diagonal of the same 1D, $N \times N$, kernel matrix. Thus this K matrix needs to act on a N^2, unidimensional data vector, storing the density field in an appropriate way. Therefore, the particular form of the kernel matrix requires the 1D data vector to be filled according to the approximations that were used to build K. Concretely speaking, this means that when we take our 2D grid of values we need to "append" one row to another, starting from the first row corresponding to the first 1D kernel matrix in the big 2D K matrix, and then proceeding until we include all the field elements. There is no other way of filling the 1D data vector: its structure is imposed by the assumptions made to build the K matrix. If we carefully follow this procedure and then apply the K matrix to the density field previously generated, we get a convergence field like the one in Fig. 6.7.

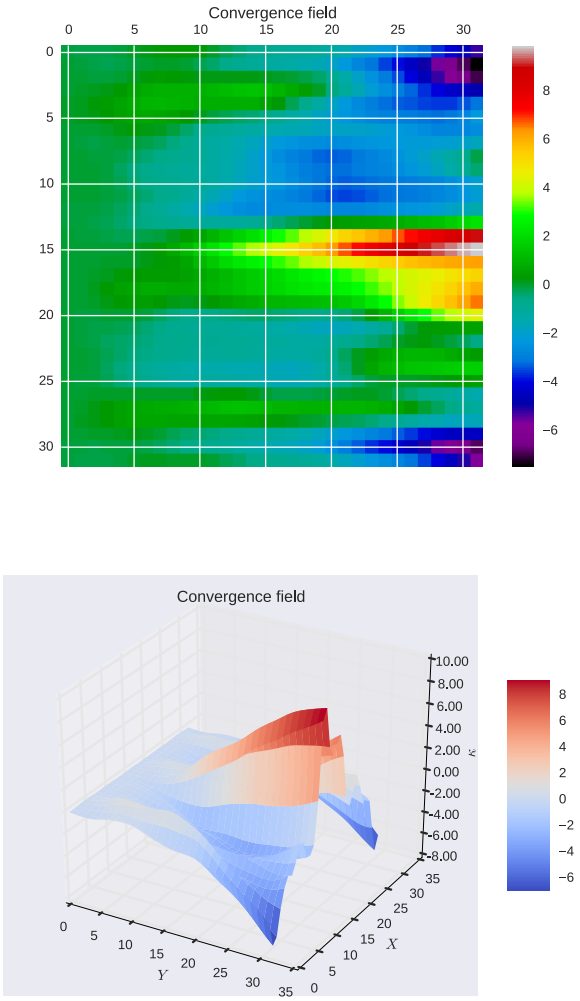

Figure 6.7: 2D convergence field, plotted on the grid and in a 3D plot, deriving from a Gaussian power spectrum with $\tilde{\sigma}_x = \tilde{\sigma}_y = 1.0$.

6.1.5 The correlation function and its approximation

We now come to another crucial difference between the 1D and 2D case. The general definition (Eq. 5.20) of the ξ matrix becomes, in two dimensions,

$$\xi_{lm} = \int \frac{\mathrm{d}^2 k}{(2\pi)^2} e^{-\mathrm{i}k_x(x_l - x_m)} e^{-\mathrm{i}k_y(y_l - y_m)} P(k), \tag{6.8}$$

and the discretised version of this relation, $\xi_{lm} = A^\alpha P_\alpha$, still defines the matrices A^α,where α is an integer labelling the wavenumber. We want to provide an explicit form for these expressions in the 2D case.

As regards ξ, its definition is relatively easy to implement once we have set up our 1D data vector from the 2D density field. Indeed, the indices l and m in the definition of ξ refer to this compressed 1D data vector, therefore we need a mapping between the indices l, m of the 1D vector, and the indices of the 2D density field. This mapping can be realised either by using some pre-built routines (for example `np.unravel`) or explicitly working out a mathematical relation between the two set of indices. Other than that, the matrix ξ is filled in a very similar fashion to the 1D case: we first calculate the correlation function as a function η of the separation between the pixels, and then exploit the homogeneity and isotropy ($\xi_{lm} = \xi_{|l-m|} = \eta(|l-m|)$) to fill ξ starting from the correlation function. The explicit expression of the latter is

$$\eta(\Delta x, \Delta y) = \int \frac{\mathrm{d}^2 k}{(2\pi)^2} P_0 e^{-\frac{\left(k_x^2\sigma_x^2 + k_y^2\sigma_y^2\right)}{2}} e^{-\mathrm{i}k_x\Delta x} e^{-\mathrm{i}k_y\Delta y} \tag{6.9}$$

$$= P_0 \int \frac{\mathrm{d}k_x}{2\pi} e^{-\frac{k_x^2\sigma_x^2}{2}} e^{-\mathrm{i}k_x\Delta x} \int \frac{\mathrm{d}k_y}{2\pi} e^{-\frac{k_y^2\sigma_y^2}{2}} e^{-\mathrm{i}k_y\Delta y} \tag{6.10}$$

$$= P_0 \frac{e^{-\frac{(\Delta x)^2}{2\sigma_x^2}}}{2\pi\sigma_x} \frac{e^{-\frac{(\Delta y)^2}{2\sigma_y^2}}}{2\pi\sigma_y} \tag{6.11}$$

$$= P_0 \frac{e^{-\frac{\left((\Delta x)^2 + (\Delta y)^2\right)}{2\sigma^2}}}{(2\pi\sigma)^2}. \tag{6.12}$$

Arrived at this point, following Sect. 5.2.2, we discretise the relation found, obtaining

$$\eta(\Delta x, \Delta y) = \frac{P_0}{2\pi\sigma^2} \frac{L_x}{N_x^2} \frac{L_y}{N_y^2} e^{-\frac{\left((\Delta x)^2 + (\Delta y)^2\right)}{2\sigma^2}} \tag{6.13}$$

Given that $\xi_{lm} = \xi_{|l-m|} = \eta(|l-m|)$, finally we have a banded matrix, such as the one shown in Fig. 6.8.
Regarding the A matrices in the expression $\xi = A^\alpha P_\alpha$, we start by evaluating the integral

$$\int \frac{\mathrm{d}^2 k}{(2\pi)^2} P(k) e^{-\mathrm{i}\vec{k}\cdot\Delta\vec{r}} \tag{6.14}$$

where $\vec{k} = (k_x, k_y)$ and $\Delta\vec{r} = (\Delta x, \Delta y)$. We introduce polar coordinates, such that $\vec{k}\cdot\Delta\vec{r} = k|\Delta\vec{r}|\cos\theta = k\Delta\vec{r}\cos\theta$, and $\mathrm{d}^2 k = k\mathrm{d}k\mathrm{d}\theta$, so that Eq. 6.14 becomes

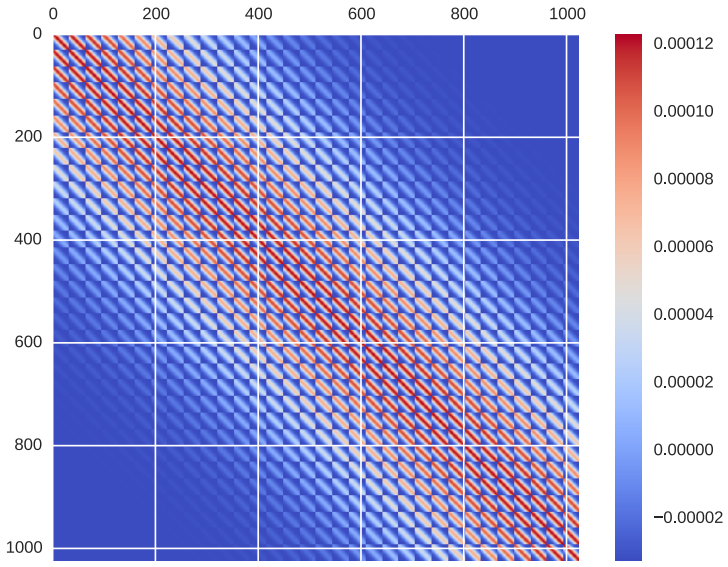

Figure 6.8: Example of 2D ξ matrix, for a Gaussian power spectrum with $\tilde{\sigma}_x = \tilde{\sigma}_y = 5.0$ and a grid of $N_x = N_y = 32$ pixels. The value of the width has been chosen to better appreciate the Gaussian decay of the correlation function from the diagonal to the edges of the matrix.

$$\int_0^\infty \int_0^{2\pi} \frac{k\,\mathrm{d}k\,\mathrm{d}\theta}{(2\pi)^2} P(k) e^{-\mathrm{i}k\Delta r\cos\theta} = \frac{1}{2\pi}\int_0^\infty P(k) J_0(k\Delta r) k\mathrm{d}k \tag{6.15}$$

where we recognised the definition of J_0, the Bessel function of the first kind of order 0,

$$J_0(k\Delta r) = \frac{1}{2\pi}\int_0^{2\pi} \mathrm{d}\theta\, e^{-\mathrm{i}k\Delta r\cos\theta}. \tag{6.16}$$

Arrived at this point, we discretise Eq. 6.15, which becomes

$$\sum_k P(k)\frac{J_0(k\Delta r)}{2\pi} k\Delta k \tag{6.17}$$

$$= \sum_{\tilde{k}} P(\tilde{k}) \frac{J_0\left(\tilde{k}\frac{2\pi}{L}\sqrt{(\Delta x)^2+(\Delta y)^2}\right)}{2\pi} \tilde{k}\frac{2\pi}{L}\Delta\tilde{k}\frac{2\pi}{L} \tag{6.18}$$

$$= \sum_{\tilde{k}} P(\tilde{k}) \frac{\tilde{k}}{2\pi}\left(\frac{2\pi}{L}\right)^2 J_0\left(\tilde{k}\frac{2\pi}{L}\sqrt{(\Delta x)^2+(\Delta y)^2}\right), \tag{6.19}$$

where we inserted the grid steps and exploited $\Delta\tilde{k} = 1$. From the last expression we read the definition of the A^α matrices (the integer α replaces $\tilde{k}$ in labelling the modulus of the wavenumber) as

$$A^\alpha = \frac{\alpha}{2\pi}\left(\frac{2\pi}{L}\right)^2 J_0\left(\tilde{\alpha}\left(\frac{2\pi}{L}\right)^2\sqrt{(\Delta\tilde{x})^2+(\Delta\tilde{y})^2}\right) \tag{6.20}$$

6.1.6 Implementation of the weights for finite S/N ratio and results

In the context of this 2D analysis we also implement the optimised weights for finite S/N ratio, developed in Sect. 4.2.2. In order to include noise in the mock dataset, when we pass from from the generated density field to the convergence field we add a Gaussian noise term ϵ to it, according to Eq. 4.4, by simply generating ϵ from a Gaussian distribution with mean 0 and constant variance σ_N. The value of σ_N is parametrized so as to be related to the variance σ_κ of the convergence data vector, through the S/N ratio:

$$\sigma_\kappa^2 = \left(\frac{S}{N}\right)^2 \sigma_N^2. \tag{6.21}$$

The inclusion of noise in the estimator has already been discussed in Sect. 4.2.2: its application to the algorithm is straightforward, as we only need to modify the weights $\mathbf{E}$ including the noise covariance matrix $\mathbf{N}$, following the expressions derived in Sect. 4.2.2. The matrix $\mathbf{N}$ is determined according to the hypothesis $N_{ij} = \sigma_i^2 \delta_{ij}^K$.
The rest of the algorithm for the recovery of the power spectrum is formally similar to the 1D case, therefore we refer the reader to Sect. 1.3 for a detailed description. The main difference is that, while in the 1D case we considered the values of the integer α, labelling the modulus of the wave number, to range from 0 to the Nyquist frequency $N/2$, we now have more possible values for α, namely from 0 to $\sqrt{2}N_x/2 = \sqrt{2}N_y/2$. This is straightforward to understand if one looks at the 2D grid in Fig. 6.9 and considers the possible values for k: the maximum value for the modulus of the wavenumber is determined by the length of the diagonal of the square grid.
Here we present a series of results obtained for the 2D case with a S/N ratio of 10. We first show some cases of recovered power spectra, with the relative window functions and χ^2 contour plots (Fig. 6.10). Then, we show similar plots for the choices of linear combinations of data previously described in Sect. 5.3.5 (Fig. 6.11 and 6.12).

6.2 The 3D case

When testing the estimator in 3D we can take advantage of the techniques employed in the 2D case and reinterpret them considering an extra dimension. However, it is indeed this extra dimension that noticeably increases the number of pixels, and consequently data, that we need to store. This may end up creating problems in terms of computer memory needed for the storage of the data. We will come back to this point in the concluding section, but it is already clear from what we showed in the 2D case that big matrices

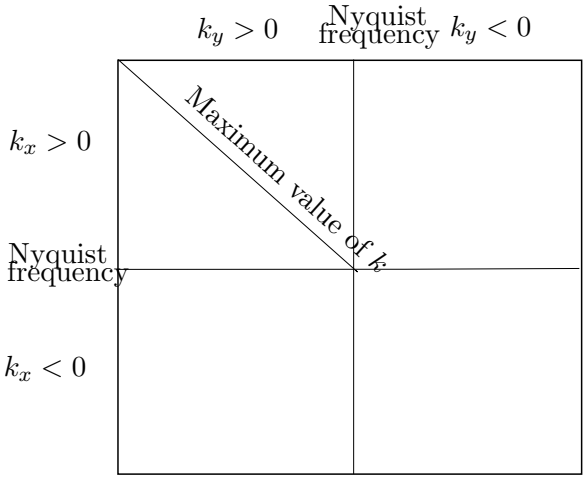

Figure 6.9: The grid of Fourier modes. The maximum possible value for k is the length of the diagonal of the square, $\sqrt{2}\times(\text{Nyquist frequency}) = \sqrt{2}\times\frac{N}{2}$.

such as the ξ matrix, whose dimension is now $(N_x \times N_y \times N_z) \times (N_x \times N_y \times N_z) = N^6$, may require a seriously challenging amount of computer memory.

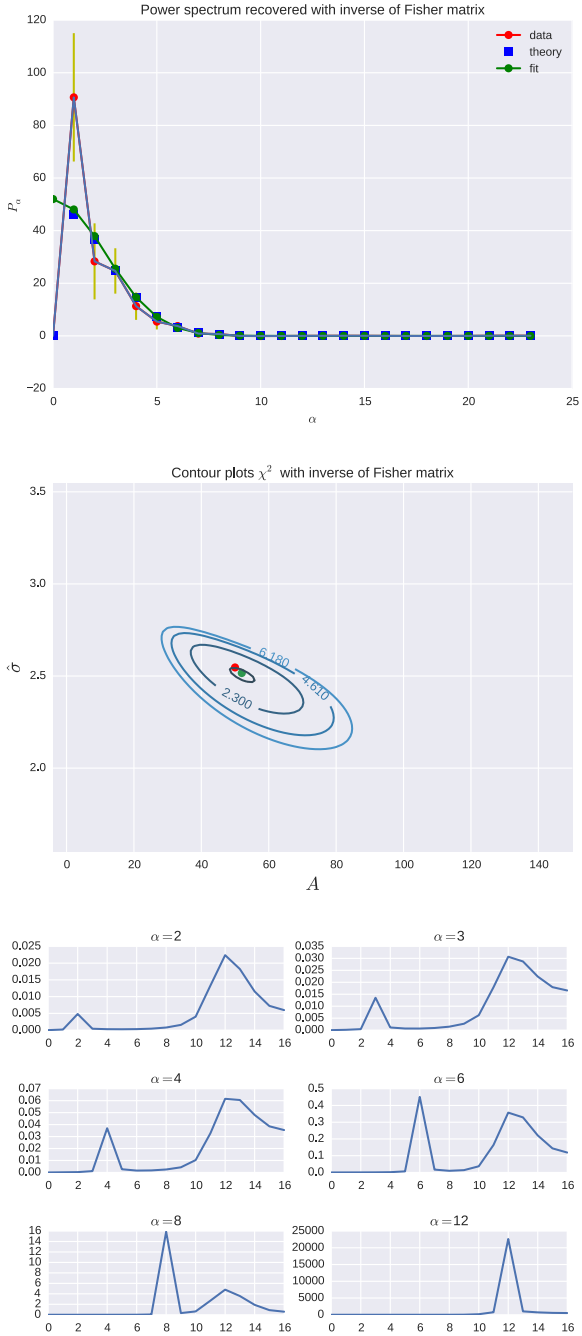

Figure 6.10: Recovered power spectrum, χ^2 contour plots and window functions of the estimator, obtained using the inverse of the noise-including Fisher matrix, which makes the estimate of $P(k)$ unbiased. The input power spectrum is a Gaussian with $\tilde{\sigma}_x = \tilde{\sigma}_y = 2.0$.

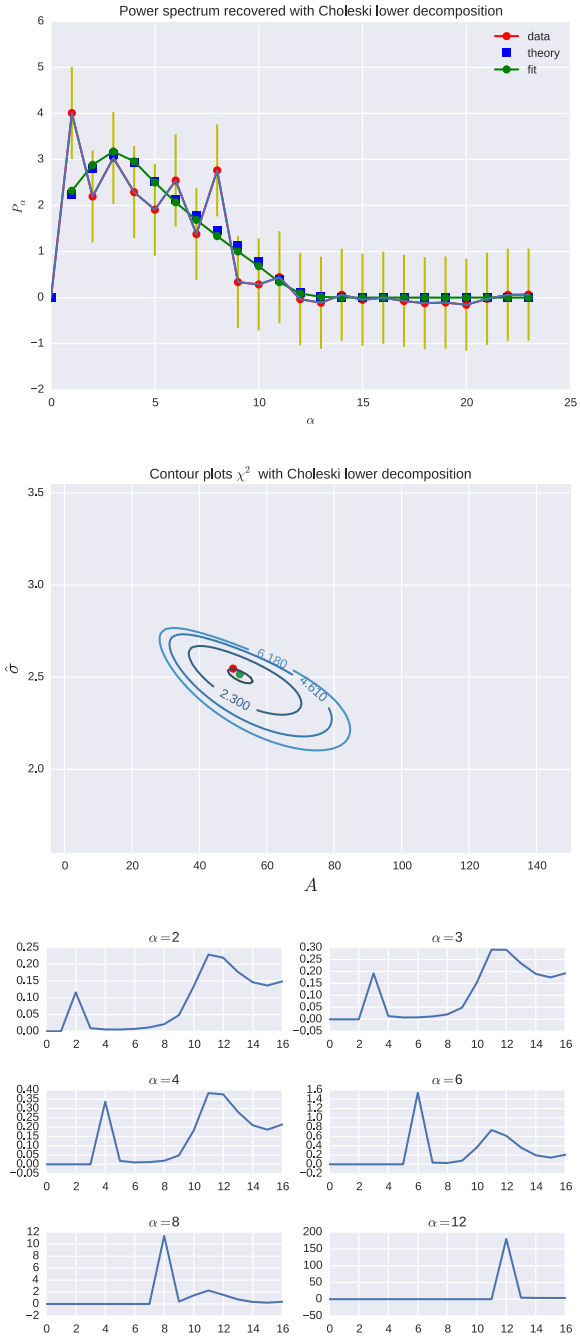

Figure 6.11: Recovered power spectrum, χ^2 contour plots and window functions of the estimator, obtained using the linear combination of data described in Sect. 3.1.2, based on the Choleski lower triangular decomposition of the Fisher matrix. The input power spectrum is a Gaussian with $\tilde{\sigma}_x = \tilde{\sigma}_y = 1.0$.

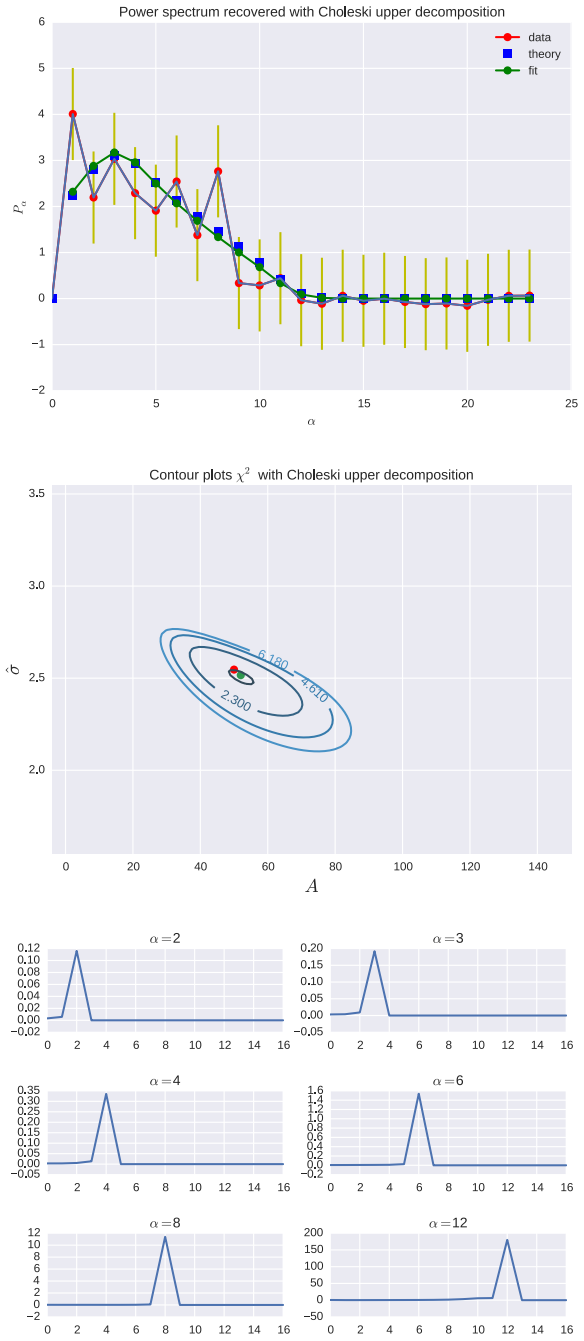

Figure 6.12: Same as Fig.6.11, this time using the linear combination $\left(\mathbf{L}^{-1}\mathbf{y}\right)^t$.

6.2.1 Tomographic approach

Our data grid is now a cube, which we create keeping the same axis length $L_x = L_y = L_z$ for each dimension. Furthermore, we adopt the same pixelization in every direction, $N_x = N_y = N_z$, referring the reader to the final chapter for a discussion of the possible features that may come up from different choices. The geometrical approach of our 3D survey is based on the extension of the 2D case to multiple planes. If in the 2D case we considered only one plane along the direction of observation, now we 'pile up' different planes, letting the "altitude" vary. This is modelled by considering, in the distant observer approximation, a cube. This geometrical configuration is shown in Fig. 6.2.1.

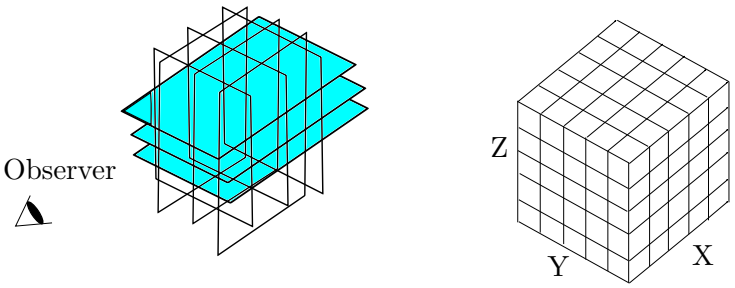

Figure 6.13: Tomographic approach in the 3D analysis and modelisation given in terms of a square grid.

6.2.2 Choice of the input power spectrum

The power spectrum is still a Gaussian,

$$P_0\, e^{-\frac{\left(k_x^2\sigma_x^2+k_y^2\sigma_y^2+k_z^2\sigma_z^2\right)}{2}} \tag{6.22}$$

where we need to have $\sigma_x = \sigma_y = \sigma_z$ to have an isotropic power spectrum. P_0 is a constant, in the following set equal to 50. We can rewrite Eq. 6.22, using the grid steps

$$k_x = \tilde{k}_x \frac{2\pi}{L_x},\ k_y = \tilde{k}_y \frac{2\pi}{L_y},\ k_z = \tilde{k}_z \frac{2\pi}{L_z} \tag{6.23}$$

$$\sigma_x = \tilde{\sigma}_x \frac{L_x}{N_x},\ \sigma_y = \tilde{\sigma}_y \frac{L_y}{N_y},\ \sigma_z = \tilde{\sigma}_z \frac{L_z}{N_z} \tag{6.24}$$

as

$$P(\tilde{k}_x, \tilde{k}_y, \tilde{k}_z) = P_0\, e^{-\frac{1}{2}\left(\left(\frac{2\pi}{L_x}\right)^2 \tilde{k}_x^2 \left(\frac{L_x}{N_x}\right)^2 \tilde{\sigma}_x^2 + \left(\frac{2\pi}{L_y}\right)^2 \tilde{k}_y^2 \left(\frac{L_y}{N_y}\right)^2 \tilde{\sigma}_y^2 + \left(\frac{2\pi}{L_z}\right)^2 \tilde{k}_z^2 \left(\frac{L_z}{N_z}\right)^2 \tilde{\sigma}_z^2\right)} \tag{6.25}$$

$$= P_0\, e^{-\frac{1}{2}\left(\left(\frac{2\pi}{N_x}\right)^2 \tilde{k}_x^2 \tilde{\sigma}_x^2 + \left(\frac{2\pi}{N_y}\right)^2 \tilde{k}_y^2 \tilde{\sigma}_y^2 + \left(\frac{2\pi}{N_z}\right)^2 \tilde{k}_z^2 \tilde{\sigma}_z^2\right)} \tag{6.26}$$

$$= P_0\, e^{-\left(\frac{2\pi}{N}\right)^2 \sigma^2 \left(\tilde{k}_x^2 + \tilde{k}_y^2 + \tilde{k}_z^2\right)}, \tag{6.27}$$

Analogously to the 2D case, we require $L_x = L_y = L_z \equiv L$, $N_x = N_y = N_z \equiv N$ and consequently $\tilde{\sigma}_x = \tilde{\sigma}_y = \tilde{\sigma}_z \equiv \sigma$ to satisfy $\sigma_x = \sigma_y = \sigma_z$. Motivated by the same intention to make our power spectrum as much isotropic as possible, we operate the same truncation applied in the 2D case, setting to 0 the values of $P(k)$ for $k > k_{Nyq}$. We show an example of this kind of power spectrum in Fig. 6.14.

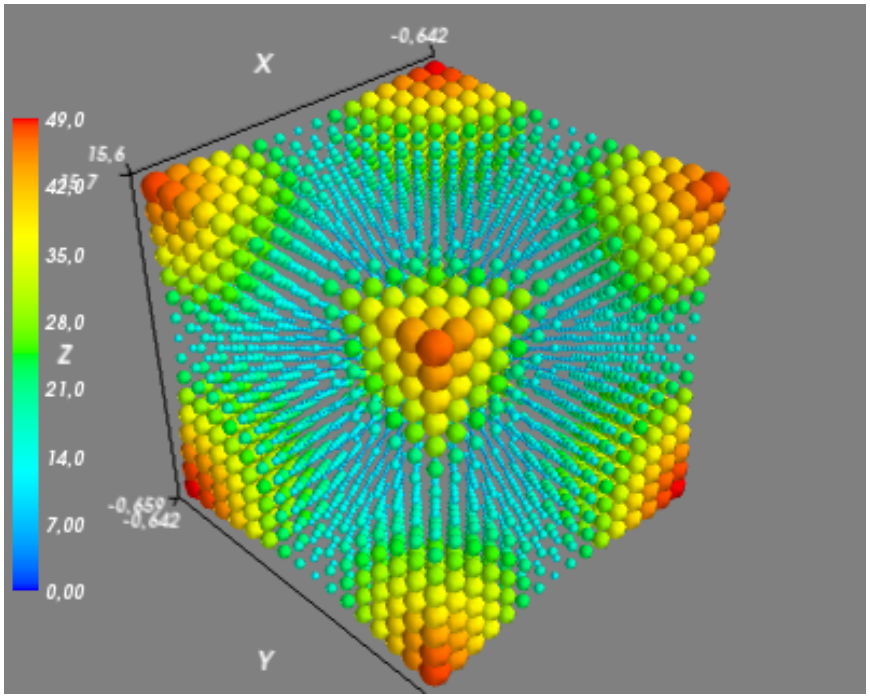

Figure 6.14: Example of Gaussian power spectrum with $\tilde{\sigma}_x = \tilde{\sigma}_y = \tilde{\sigma}_z = 0.3$.

6.2.3 The generation of the density field

To create the density field $\delta(\vec{x}) = \delta(x, y, z)$ from the chosen power spectrum we first generate the Fourier coefficients $\delta(\vec{k}) = \delta(k_x, k_y, k_z)$, paying attention to respect the Hermitian symmetry $\delta(\vec{k}) = \delta^*(-\vec{k})$, due to the reality of the field in configuration space. Written explicitly, this relation becomes

$$\delta(k_x, k_y, k_z) = \delta^*(-k_x, -k_y, -k_z). \tag{6.28}$$

To fill the 3D vector storing the field we only need to create half of the coefficients, as the others will be automatically determined by Eq. 6.28. To this purpose, it is useful to divide the cube in eight octants, corresponding to the eight possible combinations $k_x, k_y, k_z \lessgtr 0$. The octants are divided from each other by the intersections of the planes $x = N_x/2, y = N_y/2, z = N_z/2$. The elements of the grid belonging to these planes receive the same special treatment reserved, in the 2D case, to the $x = N_x/2$ and/or $y = N_y/2$ elements of the grid: they are set real and such that they satisfy $\mathrm{Re}\,\delta(\vec{k}) = \mathrm{Re}\,\delta(-\vec{k})$.

If we follow the procedure described, the result is a density field with negligible imaginary part, like the one shown in Fig. 6.15.

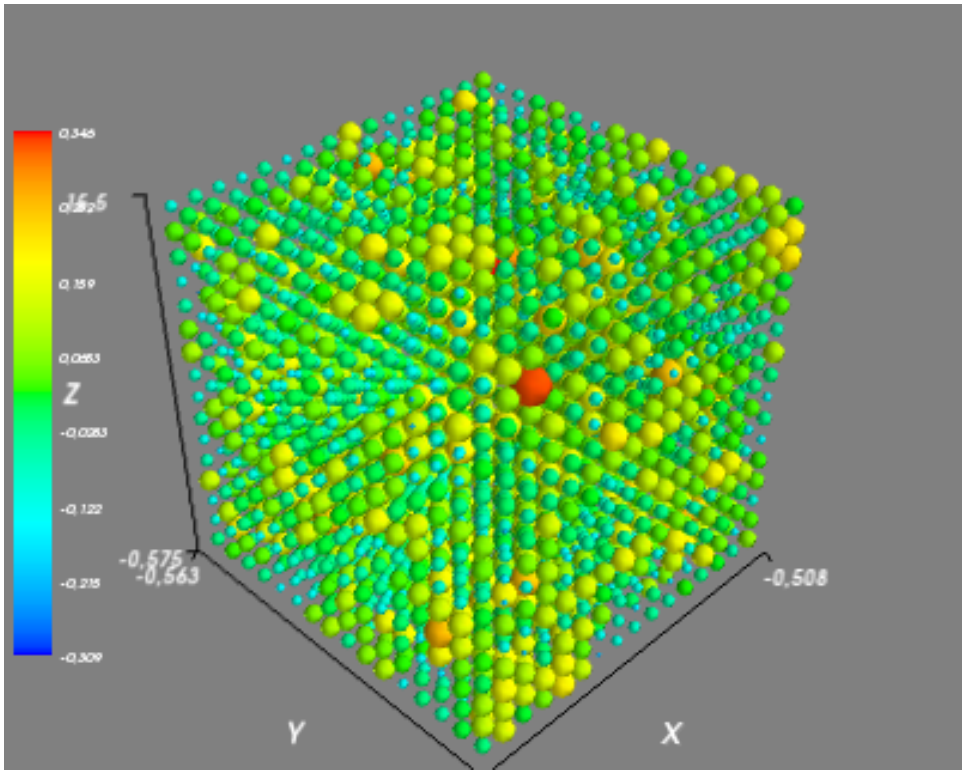

Figure 6.15: Density field generated from a Gaussian power spectrum with $\tilde{\sigma}_x = \tilde{\sigma}_y = \tilde{\sigma}_z = 0.3$. We plotted only the real part, as the imaginary one is negligible as a result of Eq. 6.28.

6.2.4 From the density to the convergence field

The procedure to build the kernel matrix directly follows from the geometry of our model. Having modelled our cubic grid as a collection of planes, we also set our K matrix as a collection of kernel matrices specifically designed for the various planes. Since we are in the distant observer approximation, every plane is equivalent to the others. If we also consider that they are independent of each other, in the sense that the convergence on one plane does not depend on the density on another (as well as the convergence on one line of sight does not depend on the density along another line of sight, as in the 2D case) we find a K matrix that is basically an extension of the 2D version, in turn obtained as an extension of the 1D kernel matrix. This is represented in Fig. 6.16, where we can appreciate the fact that K is lower triangular and largely sparse. This is crucial for the technical implementation of this matrix which, despite its big dimension, $(N_x \times N_y \times N_z) \times (N_x \times N_y \times N_z) = N^6$, can be easily stored in memory thanks to its particular configuration and sparsity.

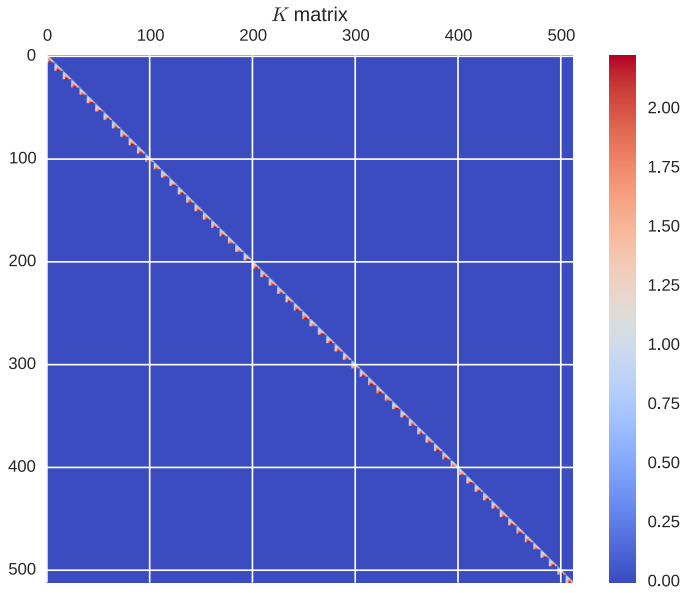

Figure 6.16: K matrix for a grid of $N_x = N_y = N_z = 8$ pixels.

As in the 2D case, this particular configuration of the kernel matrix requires us to follow the same pattern when we store the 3D density field into a single unidimensional vector, which we need to create so that we can get a convergence field acting on it with the K matrix. The creation of the

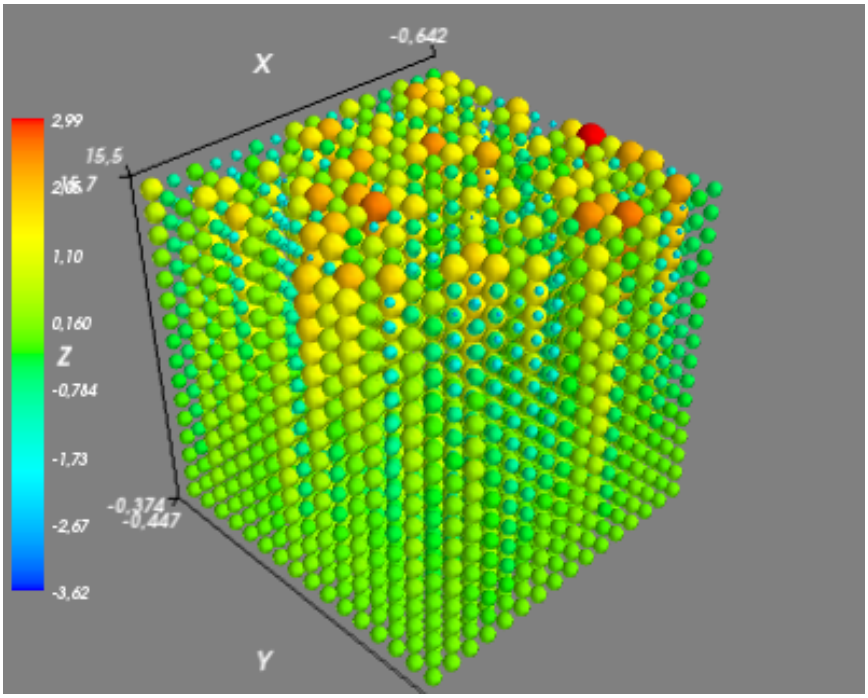

Figure 6.17: Convergence field obtained from a 3D Gaussian power spectrum with $\tilde{\sigma}_x = \tilde{\sigma}_y = \tilde{\sigma}_z = 0.3$.

unidimensional data vector can be easily achieved by simply appending the rows of the different planes of the cube one after the other, paying attention to respect the order

- a) between the planes and
- b) within a single plane.

The resulting convergence field, obtained after acting with the kernel matrix on the 1D density vector, is plotted in Fig. 6.17.

6.2.5 The correlation function and its approximation

Let us now briefly describe the creation of the ξ matrix, whose definition in the 3D case is:

$$\xi_{lm} = \int \frac{\mathrm{d}^3 k}{(2\pi)^3} e^{-\mathrm{i}k_x(x_l - x_m)} e^{-\mathrm{i}k_y(y_l - y_m)} e^{-\mathrm{i}k_z(z_l - z_m)} P(k), \tag{6.29}$$

We always start with the analytic calculation of the correlation function as a function of the separation :

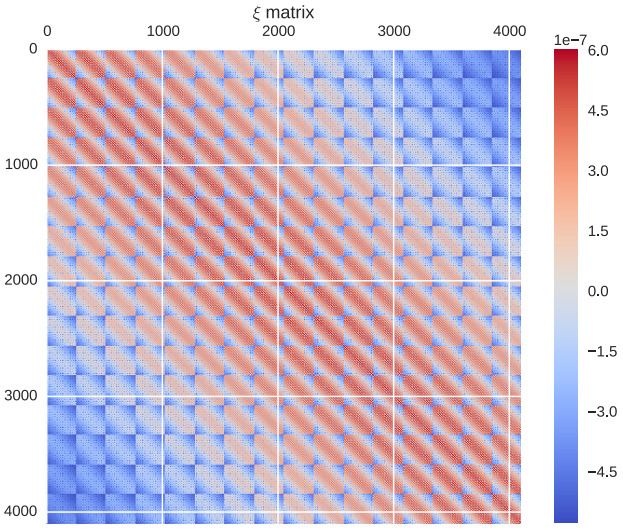

Figure 6.18: ξ matrix obtained from a 3D Gaussian power spectrum with $\tilde{\sigma}_x = \tilde{\sigma}_y = \tilde{\sigma}_z = 5.0$.

$$\eta(\Delta x, \Delta y, \Delta z) = \int \frac{\mathrm{d}^3 k}{(2\pi)^3} P_0 e^{-\frac{\left(k_x^2\sigma_x^2 + k_y^2\sigma_y^2 + k_z^2\sigma_z^2\right)}{2}} e^{-\mathrm{i}k_x\Delta x} e^{-\mathrm{i}k_y\Delta y} e^{-\mathrm{i}k_z\Delta z} \tag{6.30}$$

$$= P_0 \int \frac{\mathrm{d}k_x}{2\pi} e^{-\frac{k_x^2\sigma_x^2}{2}} e^{-\mathrm{i}k_x\Delta x} \int \frac{\mathrm{d}k_y}{2\pi} e^{-\frac{k_y^2\sigma_y^2}{2}} e^{-\mathrm{i}k_y\Delta y} \int \frac{\mathrm{d}k_z}{2\pi} e^{-\frac{k_z^2\sigma_z^2}{2}} e^{-\mathrm{i}k_z\Delta z} \tag{6.31}$$

$$= \frac{P_0}{(2\pi\sigma)^3} e^{-\frac{\left((\Delta x)^2 + (\Delta y)^2 + (\Delta z)^2\right)}{2\sigma^2}} \tag{6.32}$$

where $\sigma = \sigma_x = \sigma_y = \sigma_z$. Discretising this expression, according to Sect. 5.2.2, we get

$$\eta(\Delta x, \Delta y, \Delta z) = \frac{P_0}{\left(\sqrt{2\pi}\sigma\right)^3} \frac{L_x}{N_x^2} \frac{L_y}{N_y^2} \frac{L_z}{N_z^2} e^{-\frac{\left((\Delta x)^2 + (\Delta y)^2 + (\Delta z)^2\right)}{2\sigma^2}}. \tag{6.33}$$

As in the 2D case, we then fill the ξ matrix exploiting its definition and the homogeneity and isotropy, which imply $\xi_{lm} = \xi_{|l-m|} = \eta(|l-m|)$. The result is a banded matrix like the one shown in Fig. 6.18.
We then need to calculate the A matrices, coefficients of the expansion of the ξ matrix as a discrete summation of the power spectrum at different

wavenumbers, labelled by α. We start by evaluating the integral definition of ξ

$$\int \frac{\mathrm{d}^3k}{(2\pi)^3} P(k) e^{-\mathrm{i}\vec{k}\cdot\vec{\Delta r}} \tag{6.34}$$

where this time $\vec{k} = (k_x, k_y, k_z)$ and $\Delta\vec{r} = (\Delta x, \Delta y, \Delta z)$. We introduce spherical polar coordinates, such that $\vec{k}\cdot\Delta\vec{r} = k|\Delta\vec{r}|\cos\theta$, and $\mathrm{d}^3k = k^2\sin\theta \mathrm{d}k\mathrm{d}\theta\mathrm{d}\phi$. The integral becomes

$$\frac{1}{(2\pi)^3}\int_0^\infty\int_0^\pi\int_0^{2\phi} P(k)e^{-\mathrm{i}k\Delta r\cos\theta}k^2\sin\theta\mathrm{d}k\mathrm{d}\theta\mathrm{d}\phi \tag{6.35}$$

$$=\frac{1}{(2\pi)^2}\int_0^\infty\int_0^\pi P(k)e^{-\mathrm{i}k\Delta r\cos\theta}k^2\sin\theta\mathrm{d}k\mathrm{d}\theta \tag{6.36}$$

$$=\frac{1}{(2\pi)^2}\int_0^\infty\int_{-1}^{+1} P(k)e^{-\mathrm{i}k\Delta rt}k^2\mathrm{d}k\mathrm{d}t \tag{6.37}$$

$$=\frac{2}{(2\pi)^2}\int_0^\infty P(k)\frac{\sin(k\Delta r)}{\Delta r}\,k\,\mathrm{d}k \tag{6.38}$$

where we first integrated in ϕ and then performed a change of variable, from θ to $t \equiv \cos\theta$. At this point we perform a discretisation, so that the previous expression becomes

$$\sum_k P(k)\frac{2}{(2\pi)^2}\frac{\sin(k\Delta r)}{\Delta r}k\Delta k \tag{6.39}$$

$$=\sum_{\tilde{k}} P(\tilde{k})\frac{2}{(2\pi)^2}\frac{\sin\left(\left(\tilde{k}\frac{2\pi}{L}\right)\frac{L}{N}\sqrt{(\Delta\tilde{x})^2+(\Delta\tilde{y})^2+(\Delta\tilde{z})^2}\right)}{\frac{L}{N}\sqrt{(\Delta\tilde{x})^2+(\Delta\tilde{y})^2+(\Delta\tilde{z})^2}}\tilde{k}\frac{2\pi}{L}\Delta\tilde{k}\frac{2\pi}{L} \tag{6.40}$$

where we inserted explicitly the grid steps and exploited the hypothesis $L_x = L_y = L_z = L$ and $N_x = N_y = N_z = N$. We finally obtain for the A matrices

$$A^\alpha = \frac{2N\alpha}{L^3}\frac{\sin\left(\alpha\frac{2\pi}{N}\sqrt{(\Delta\tilde{x})^2+(\Delta\tilde{y})^2+(\Delta\tilde{z})^2}\right)}{\sqrt{(\Delta\tilde{x})^2+(\Delta\tilde{y})^2+(\Delta\tilde{z})^2}} \tag{6.41}$$

We notice that this expression is not defined for $|\Delta\tilde{r}| = \sqrt{(\Delta\tilde{x})^2+(\Delta\tilde{y})^2+(\Delta\tilde{z})^2} = 0$, therefore we perform a Taylor expansion when $|\Delta\tilde{r}| \to 0$ and we use the result as a definition of A^α in the special case $|\Delta\tilde{r}| = 0$. We find

$$\lim_{|\Delta\tilde{r}|\to 0} A^\alpha = \frac{4\pi}{L^3}\alpha^2 \tag{6.42}$$

6.2.6 Results

Bearing in mind that the values for k can range from 0 to $\sqrt{3} \times N/2$, as a result of the cubic grid adopted, we can now present some of the results obtained for the 3D analysis. We first show in Fig. 6.19 the recovery of the power spectrum, with a S/N ratio of 10, using the inverse of the noise-including Fisher matrix to get an unbiased estimate of the power spectrum. As usual, we plot not only the recovered $P(k)$, but also the χ^2 contour plots and the window functions of the estimator. We then show in Fig. 6.20 and 6.21 the same graphs, but relative to the linear combinations of data described in Sect. 5.3.5.

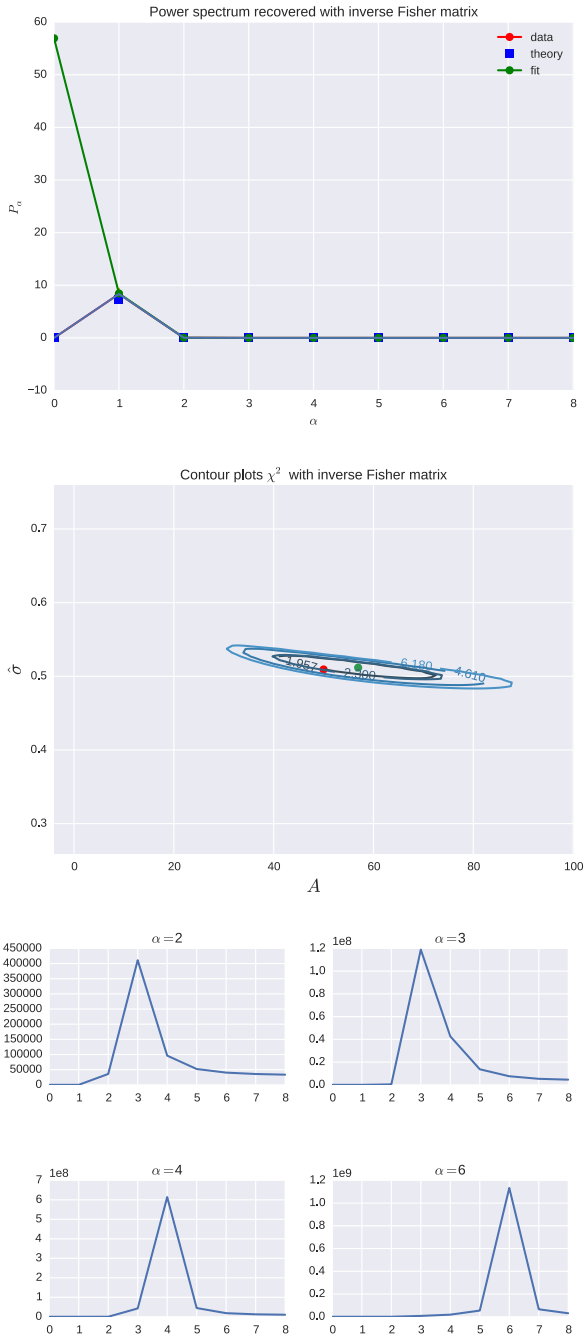

Figure 6.19: Recovered power spectrum, χ^2 contour plots and window functions of the estimator, obtained using the inverse of the noise-including Fisher matrix, which makes the estimate of $P(k)$ unbiased. The input power spectrum is a Gaussian with $\tilde{\sigma}_x = \tilde{\sigma}_y = \tilde{\sigma}_z = 5.0$.

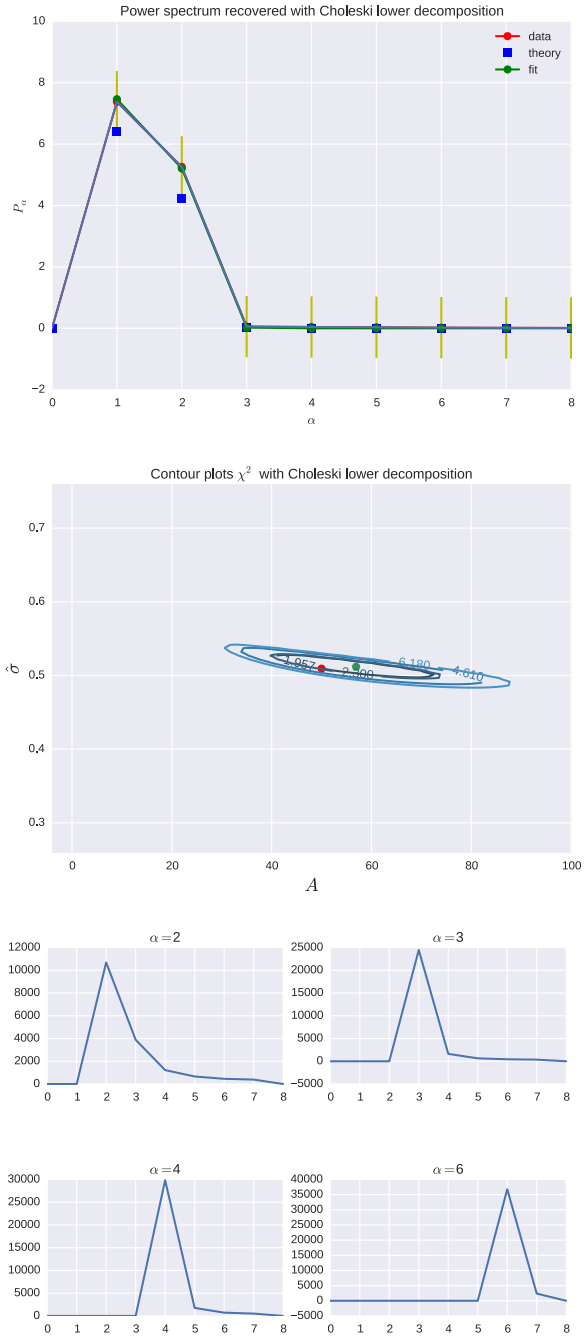

Figure 6.20: Recovered power spectrum, χ^2 contour plots and window functions of the estimator, obtained using the linear combination of data described in Sect. 3.1.2, based on the Cholesky lower triangular decomposition of the Fisher matrix. The input power spectrum is a Gaussian with $\tilde{\sigma}_x = \tilde{\sigma}_y = \tilde{\sigma}_z = 5.0$.

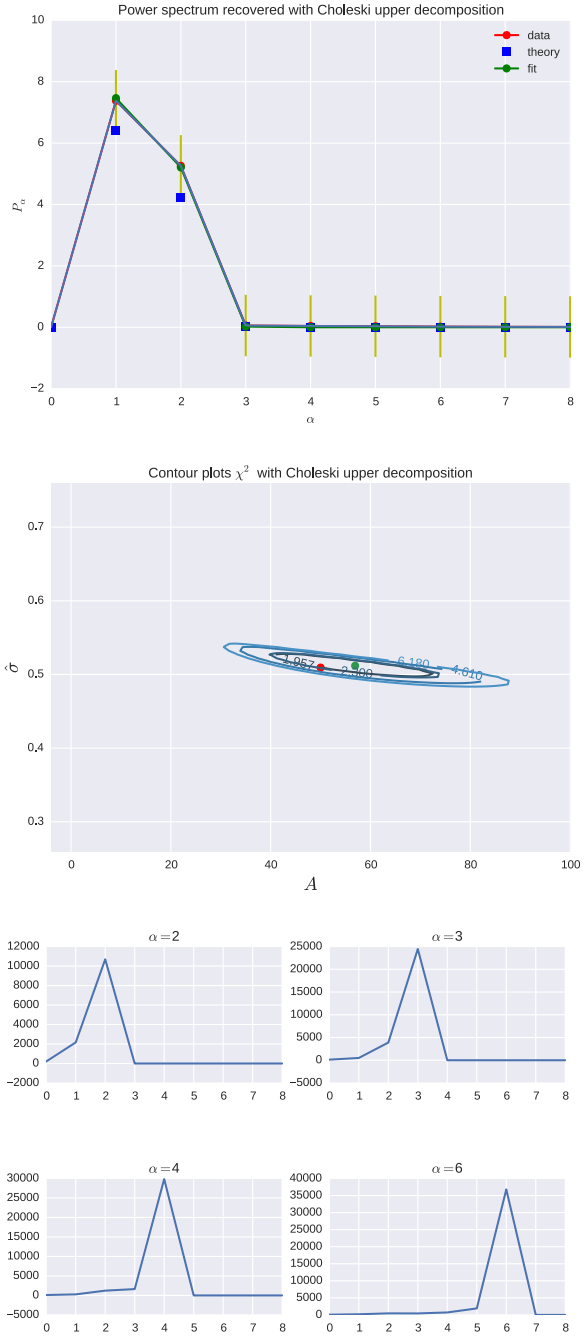

Figure 6.21: Same as Fig. 6.11, this time using the linear combination $\left(\mathbf{L}^{-1}\mathbf{y}\right)^t$.

Chapter 7

Conclusions

In this concluding chapter we summarise and comment the results obtained, we discuss the approximations made in devising our estimator and we propose some possible future developments of our work. In particular, we include the calculations for the shear γ.

7.1 Discussion of the results obtained and problems encountered

We have successfully demonstrated that the estimator works, well recovering the analytic form of the power spectrum as witnessed by the good χ^2 values reported. However, we notice that generally speaking the width of the input Gaussian is recovered worse than the amplitude. We also point out that the goodness of the global recovery highly depends on the analytic form of the input power spectrum, in particular on its width. This is true in every dimension (1D, 2D and 3D case), but we identify two main trends:

- the dependence on the width of the power spectrum is less important as we *increase* the dimension and is related to the appearance of the spurious feature in the window functions already described in Sect. 5.3.4;
- despite this fact, the χ^2 results improve as we *decrease* the dimension.

While we are unable to fully explain the appearance of the strange feature in the window functions, we think that the first aspect can be related to the development of optimal weights for different signal-to-noise regimes. In fact, we notice that while in the 1D case, when we worked only with weights optimised for infinite S/N ratio, the dependence on the width of the power spectrum was particularly strong, this is less true in the 2D and 3D case, where we implemented weights optimised for a finite S/N ratio. We suspect that the issue could be of numerical origin and perhaps connected with the

particular analytic form chosen for the input power spectrum. Therefore, we propose to study different input power spectra in future work, especially some that may allow for a decay from finite values to essentially 0 in a wider range of k, rather than the Gaussian used.
As regards the second point, we suspect that it might be the result of effects due to the discreteness of the grid considered. In fact, while in the 1D case we could push our analysis to fairly big numbers of pixels N, this was not possible for the 2D and 3D case, for computational reasons (see next Section for a discussion). We suspect that, extending the 2D and 3D algorithm to larger arrays (for example through the use of supercomputers) these issues might disappear as a result of the increased precision in our analysis, which is a discretised treatment of a continuous problem. We think that this particularly applies to the approximation given for the correlation function and its approximation. We defined both of them through Eq. 4.9

$$\xi_{lm} = \int \frac{\mathrm{d}^3 k}{(2\pi)^3} P(k) \exp^{-\mathrm{i}\vec{k}\cdot(\vec{r}_l - \vec{r}_m)} \equiv A^{\alpha}_{lm} P_{\alpha} \tag{7.1}$$

In a comparison with the actual correlation function, i.e. the one calculated directly from the realisation of the field through the definition $\xi_{lm} = \langle \delta_l \delta_m \rangle$, we notice that both the analytic and the approximated version represent a more and more faithful description of the original one as the number of pixels increase. We show this effect in Fig.7.1, where we propose the same plot shown in Fig. 5.8, this time with an array of 512 pixels. We can see that the ergodicity is much improved and the analytic correlation function represents a more accurate description of the actual correlation function. The approximation given by the summation $A^{\alpha}_{lm} P_{\alpha}$ relies on the fact that A_{ij} is constant along the interval Δk, which represents our discretisation of the infinitesimal interval $\mathrm{d}k$. Therefore, the approximation will be better and better as this interval becomes smaller and smaller as the number of pixels increase.

We would like to particularly emphasise the results obtained for the window functions of the estimator. We successfully managed to implement window functions that are well peaked around the k value of interest, although at times they get seriously compromised by the spurious feature present around the Nyquist frequency. However, we also managed to implement window functions that are one-sided, as described in Tegmark's paper [Tegmark (1997)]. With the choice of the linear combination $\left(\mathbf{L}^{-1}\mathbf{y}\right)^t$ we even managed to get rid of this feature at it arises towards the Nyquist frequency which is cut off by the lower triangular window matrix. This is just an example of a particularly attractive feature of these window functions, which make them particularly interesting in future applications. Indeed, we might take advantage of the one-sided window functions to isolate different regimes for

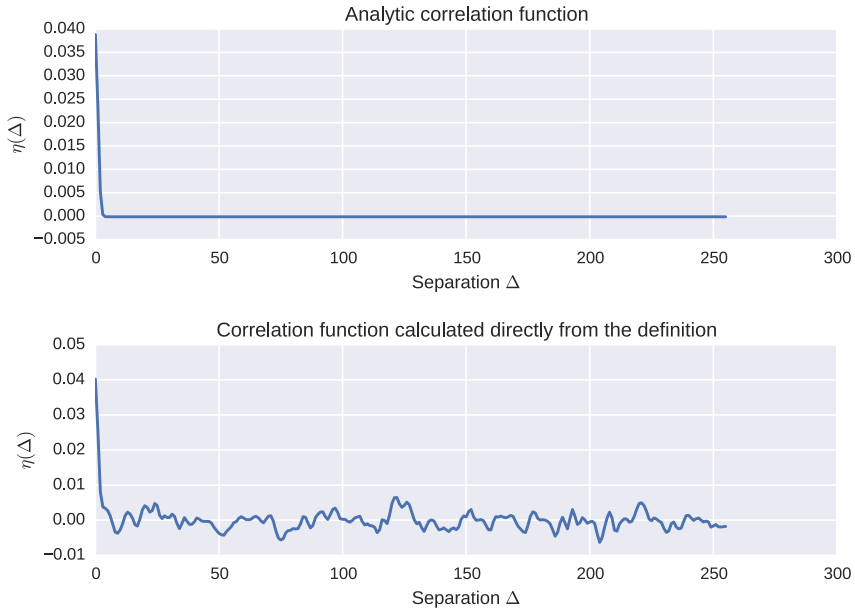

Figure 7.1: Comparison between the correlation function calculated analytically from the power spectrum (top) and directly from the realisation of the field, exploiting the definition $\xi_{lm} = \langle \delta_l \delta_m \rangle$ (bottom). Here the lack of ergodicity found in Fig. 5.8, due to the small N considered ($N = 64$) there, is much less important.

the k-values, namely, we might use the Choleski lower decomposition to isolate the low-k values, and the other decomposition for the high-k regime. This is crucial, as it would allow us to concentrate on the k-values that we are most interested in, without unwanted influences from the others. We could therefore become sensitive or insensitive at various parts of the matter power spectrum that are influenced by different physical processes, for example the region around $k \sim 1\ h\ \mathrm{Mpc}^{-1}$, governed by neutrino mass effects or the high-k regime ($k > 1\ h\ \mathrm{Mpc}^{-1}$), which is affected by uncertain baryon feedback processes.

7.1.1 Computational requirements

Now we would like to briefly comment the computational requirements for the algorithm for the recovery of the power spectrum as it has been presented in this thesis. We start by showing in Fig. 7.2 some plots concerning the scaling of the computational time with the total number of pixels N, for all the three cases considered. In the 1D case N represents the number of

Dimension	Index p
1	4.72
2	3.68
3	2.96

Table 7.1: Fitted index p of power-law scaling with the number of pixels N, in the various cases considered.

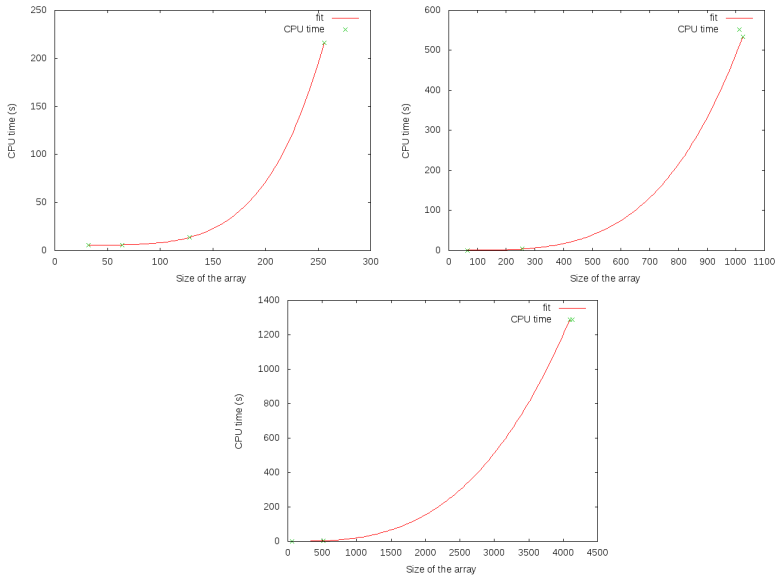

Figure 7.2: Computational time required for the three dimensions considered, as a function of the total number of pixels

pixels on the one and only axis of the grid, in the 2D and 3D case it is the square or the cube of the number of pixels on one axis (the grid is always considered square). We find that the computational time scales like N^p with p roughly between 3 and 5.

The computational time shown refers only to the pure algorithm for the recovery of the power spectrum, without any other features such as the calculation of the window functions or the χ^2 analysis. It is clear how the current situation is not ideal for a realistic implementation. However, we claim that some improvements can be achieved by some future optimisation performed on the algorithm. Improvements may also come from the implementation of the code in programming languages other than `Python`, which was used for this thesis since we were mainly interested in studying the application of the principle rather than in an optimised version of the

algorithm. In addition to that, we might always consider the possibility of using supercomputers for realistic analyses, especially if we consider the problems linked with the storage of the data, discussed in the following.

Indeed, one of the problems encountered in the computational implementation of the estimator was the amount of computer memory needed for the storage of the data. As already pointed out in the text, this particularly applies to the 3D case, where the presence of very large non-sparse matrices (of order N^6, where N is the number of pixels on one axis) constitutes a serious issue and in our case effectively prevented the application of the algorithm to arrays larger than $16 \times 16 \times 16$. In this case too, a future reconsideration of the algorithm, to the purpose of optimising the storage of the data, seems appropriate. Nevertheless, it might happen that, in order to deal with realistic configurations, we would simply need to apply the algorithm on supercomputers.

7.1.2 Approximations

Let us now come to the discussion of the approximations made in the development of our estimator.

We start from the hypothesis of redshift-independent matter power spectrum, which was assumed from the beginning of the treatment. The reason behind this assumption is that even in this simplified case the success of the method is not guaranteed *a priori*, therefore our "exercise" constitutes at the same time a necessary first step and a "bottleneck" for the development of a complete estimator: if this simplified version had failed, there would have been no hope to proceed in a more complicated, redshift-dependent analysis. Since we proved that the estimator successfully passed this "preliminary test", this opens up the possibility of a development of a redshift-dependent estimator in future work. For example, a straightforward approach might consider linear growth, where $P(k, z)$ factorizes, but a full, general non-linear $P(k, z)$ would need more development.

We also assumed both the density and noise fields to be Gaussian, which allowed us to exploit the Wick's theorem in the derivation of the optimal weights (see Sect.4.2.2). For the density field, this hypothesis seems justified by most of the inflationary models [Liddle (1999)] and recent Planck results [Planck Collaboration], while for the noise it is common procedure to model it with a Gaussian distribution (see Refregier (2003)). Furthermore, the hypothesis of Gaussian fields would be valid for large "voxels" (volumetric pixels) as a result of the Central Limit Theorem.

Regarding the distant observer approximation, this seems to be a reasonable hypothesis, especially considering the growing depth of surveys, such as Euclid, planned to extend until redshift $z \sim 2$ [Amendola et al.].

7.2 Future developments

We have already mentioned some of the future prospects for this estimator. We summarise them here:

- To confirm the validity of the method, we think that further simulations need to be carried out, using the same testing mechanism, but changing the input power spectrum. For example one might use more realistic power spectra coming from codes like CAMB [Lewis et al. (2000)]. One might also be interested in carrying out further analyses on the one-sided window functions, for example by still choosing simple analytic forms, but with more features towards higher scales.

- Thinking about a real implementation of the method, one has to consider how too calculate the various elements of the algorithm without knowing the original power spectrum *a priori*. In fact, in our "exercise" we knew the analytic form of the input power spectrum, but this is not true in the real case. Therefore one might think about a "prior", i.e. a fiducial power spectrum from which the estimator can start, and then proceed in an iterative approach, each time reinserting the estimated power spectrum as the input one. This could be repeated as many times as needed to satisfy some convergence criteria. A similar approach can be found in Bond et al. (1998) and may initially be investigated in the simple form described in this thesis, where the "prior" power spectrum is the true one.

- A very important and attractive feature is the possibility of varying the number of pixels in the different directions, so that we do no longer have a square grid. This approach can certainly be tested in our simplified model, with a Gaussian power spectrum. It is hard to speculate what features may arise from this procedure, but certainly it is very appealing as it might be the actual case for future weak lensing surveys (for example Euclid). The motivation behind that is that weak lensing estimates strongly depend on the estimation of redshifts of the sources. Since the number of galaxies that future surveys will utilize as lensing sources is too large for spectroscopic measurements, one needs to rely on the photometric redshifts whose accuracy may not be sufficient for future surveys which are expected to have very small statistical errors.

  Since the positions of sources have errors of typically 10% (see for example Refregier et al. (2010)), there is no point in having bins that are very close together. For this reason one might well want to have a coarser grid in the radial direction, for example 5 - 10 bins for $z = 0 \div 2$, and a finer grid in the angular direction, of the order of a few arcminutes square for each pixel.

- The method can be extended to the treatment of shear (see next section).

7.3 Shear

The derivation for shear proceeds in a similar way to the case of convergence. Let the data vector be a set of shear components $\vec{x} = (\{\gamma_1\}, \{\gamma_2\})$, in n_{vox} voxels, $n_{vox} = n_{pix} \times n_{shells}$, for images with n_{pix} across the sky, and in n_{shells} tomographic bins. Thus $\vec{x}$ is a $2n_{vox}$ - dimensional vector. It has covariance matrix

$$C_{ij} = \left\langle x_i x_j^T \right\rangle = \sum_X \sum_l C^X_{l,\alpha\beta} \frac{\partial C_{ij}}{\partial C^X_{l,\alpha\beta}} + N_{ij} \tag{7.2}$$

where $X = EE, BB, EB$, $l = l_{\min}, \ldots, l_{\max}$, N_{ij} is the shot noise, and α, β label the tomographic shells that points i, j reside in. $C^X_{l,\alpha\beta}$ are tomographic cross- and auto-power spectra associated with E and B modes. For now, let us ignore B modes, so $X = EE$ only and we will drop the superscript. The lensing potential in shell α at angular coordinate $\mathbf{\Omega}$ can be written (see Bartelmann and Schneider (2001), or Munshi et al. (2008))

$$\phi_\alpha(\mathbf{\Omega}) = \frac{2}{c^2} \int_0^\infty \mathrm{d}r \, g_\alpha(r) \, \Phi(\vec{r}) \tag{7.3}$$

where Φ is the gravitational potential, and

$$g_\alpha(r) = \int_{z(r)}^\infty \mathrm{d}z' p_\alpha(z') \left(\frac{1}{r} - \frac{1}{r'} \right) \tag{7.4}$$

(flat Universe), with $p_\alpha(z)$ being the redshift distribution of shell α. In the Limber approximation,

$$C^{\phi\phi}_{l,\alpha\beta} = \frac{4}{c^4} \int_0^\infty \mathrm{d}r \, g_\alpha(r) \, g_\beta(r) \, P_\Phi\left(\frac{l}{r}; t(r) \right) \tag{7.5}$$

where P_Φ is the potential power spectrum (evaluated at the lookback time corresponding to the distance r). From the relationship between shear and the potential, the shear power spectrum is

$$C_{l,\alpha\beta} \equiv C^{\gamma\gamma}_{l,\alpha\beta} = \frac{1}{4} \frac{(l+2)!}{(l-2)!} C^{\phi\phi}_{l,\alpha\beta}. \tag{7.6}$$

The correlation function of the complex number $\gamma = \gamma_1 + \mathrm{i}\gamma_2$ is

$$\langle \gamma_\alpha (\mathbf{\Omega}) \gamma_\beta (\mathbf{\Omega} + \theta) \rangle = \sum_l C_{l,\alpha\beta} P_l (\cos\theta) \tag{7.7}$$

where P_l is a Legendre polynomial, and θ is the angle between two pixels. This is divided equally between γ_1 and γ_2, and the cross term is zero.

Acknowledgements

I wish to express all my gratitude to Professor Sabino Matarrese and Professor Alan Heavens for their invaluable guidance and the opportunity that they gave me to work on an extremely interesting topic in a great environment, during a wonderful year as an Erasmus student.

Bibliography

Amendola, L. et al. Cosmology and fundamental physics with the euclid satellite. 2013. *Living Rev. Rel*, 16(6).

Bacon, D. J., Refregier, A. R., and Ellis, R. S. (2000). Detection of weak gravitational lensing by large-scale structure. *Monthly Notices of the Royal Astronomical Society*, 318(2):625–640.

Bartelmann, M. and Schneider, P. (2001). Weak gravitational lensing. *Physics Reports*, 340(4):291–472.

Bernardeau, F., Colombi, S., Gaztanaga, E., and Scoccimarro, R. (2002). Large-scale structure of the universe and cosmological perturbation theory. *Physics Reports*, 367(1):1–248.

Bond, J., Jaffe, A. H., and Knox, L. (1998). Estimating the power spectrum of the cosmic microwave background. *Physical Review D*, 57(4):2117.

Bond, J. R. (1995). Signal-to-noise eigenmode analysis of the two-year cobe maps. *Physical review letters*, 74(22):4369.

Cooray, A. and Sheth, R. (2002). Halo models of large scale structure. *Physics Reports*, 372(1):1–129.

Eddington, A. S., Dyson, F. W., and Davidson, C. (1920). A determination of the deflection of light by the sun's gravitational field, from observations made at the total eclipse of may 29, 1919. *Philosophical Transactions of the Royal Society of London A: Mathematical, Physical and Engineering Sciences*, 220(571-581):291–333.

Efstathiou, G. (2004). Myths and truths concerning estimation of power spectra: the case for a hybrid estimator. *Monthly Notices of the Royal Astronomical Society*, 349(2):603–626.

Einstein, A. (1911). Über den einfluß der schwerkraft auf die ausbreitung des lichtes. *Annalen der Physik*, 340(10):898–908.

Feldman, H. A., Kaiser, N., and Peacock, J. A. (1993). Power spectrum analysis of three-dimensional redshift surveys. *arXiv preprint astro-ph/9304022*.

Hu, W., Eisenstein, D. J., and Tegmark, M. (1997). Weighing neutrinos with galaxy surveys. *arXiv preprint astro-ph/9712057*.

Kaiser, N., Wilson, G., and Luppino, G. A. (2000). Large-scale cosmic shear measurements. *arXiv preprint astro-ph/0003338*.

Lesgourgues, J., Mangano, G., Miele, G., and Pastor, S. (2013). *Neutrino cosmology*. Cambridge University Press.

Lesgourgues, J. and Pastor, S. (2006). Massive neutrinos and cosmology. *Physics Reports*, 429(6):307–379.

Lesgourgues, J. and Tram, T. (2011). The cosmic linear anisotropy solving system (class) iv: efficient implementation of non-cold relics. *Journal of Cosmology and Astroparticle Physics*, 2011(09):032.

Lewis, A., Challinor, A., and Lasenby, A. (2000). Efficient computation of cosmic microwave background anisotropies in closed friedmann-robertson-walker models. *The Astrophysical Journal*, 538(2):473.

Liddle, A. R. (1999). An introduction to cosmological inflation. *arXiv preprint astro-ph/9901124*.

Liddle, A. R. and Lyth, D. H. (2000). *Cosmological inflation and large-scale structure*. Cambridge University Press.

Meneghetti, M. (2012). *Introduction to Gravitational Lensing - Lecture Scripts*.

Munshi, D., Valageas, P., Van Waerbeke, L., and Heavens, A. (2008). Cosmology with weak lensing surveys. *Physics Reports*, 462(3):67–121.

Peacock, J. and Nicholson, D. (1991). The large-scale clustering of radio galaxies. *Monthly Notices of the Royal Astronomical Society*, 253(2):307–319.

Peacock, J. A. (1999). *Cosmological physics*. Cambridge university press.

Percival, W. J., Baugh, C. M., Bland-Hawthorn, J., Bridges, T., Cannon, R., Cole, S., Colless, M., Collins, C., Couch, W., Dalton, G., et al. (2001). The 2df galaxy redshift survey: the power spectrum and the matter content of the universe. *Monthly Notices of the Royal Astronomical Society*, 327(4):1297–1306.

Planck Collaboration, X. Planck 2015 results. xvii. constraints on primordial non-gaussianity. 2015.

Press, W. H. (2007). *Numerical recipes 3rd edition: The art of scientific computing*. Cambridge university press.

Refregier, A. (2003). Weak gravitational lensing by large-scale structure. *arXiv preprint astro-ph/0307212*.

Refregier, A., Amara, A., Kitching, T., Rassat, A., Scaramella, R., Weller, J., et al. (2010). Euclid imaging consortium science book. *arXiv preprint arXiv:1001.0061*.

Schneider, P. (1992). *Gravitational lensing statistics*. Springer.

Schneider, P. (2006). Weak gravitational lensing. In *Gravitational Lensing: Strong, Weak and Micro*, pages 269–451. Springer.

Seitz, S., Schneider, P., and Ehlers, J. (1994). Light propagation in arbitrary spacetimes and the gravitational lens approximation. *Classical and Quantum Gravity*, 11(9):2345.

Tegmark, M. (1997). How to measure cmb power spectra without losing information. *Physical Review D*, 55(10):5895.

Tegmark, M., Blanton, M. R., Strauss, M. A., Hoyle, F., Schlegel, D., Scoccimarro, R., Vogeley, M. S., Weinberg, D. H., Zehavi, I., Berlind, A., et al. (2004). The three-dimensional power spectrum of galaxies from the sloan digital sky survey. *The Astrophysical Journal*, 606(2):702.

Tegmark, M., Hamilton, A. J., and Xu, Y. (2002). The power spectrum of galaxies in the 2df 100k redshift survey. *Monthly Notices of the Royal Astronomical Society*, 335(4):887–908.

Tegmark, M., Taylor, A. N., and Heavens, A. F. (1997). Karhunen-loeve eigenvalue problems in cosmology: how should we tackle large data sets? *The Astrophysical Journal*, 480(1):22.

Treu, T. (2010). Strong lensing by galaxies. *arXiv preprint arXiv:1003.5567*.

Van Waerbeke, L., Mellier, Y., Erben, T., Cuillandre, J., Bernardeau, F., Maoli, R., Bertin, E., Mc Cracken, H., Fevre, O. L., Fort, B., et al. (2000). Detection of correlated galaxy ellipticities on cfht data: first evidence for gravitational lensing by large-scale structures. *Arxiv preprint astro-ph/0002500*.

Wambsganss, J. (1998). Gravitational lensing in astronomy. *Living Rev. Relativity*, 1:12.

Wittman, D. M., Tyson, J. A., Kirkman, D., Dell'Antonio, I., and Bernstein, G. (2000). Detection of weak gravitational lensing distortions of distant galaxies by cosmic dark matter at large scales. *Nature*, 405(6783):143–148.